MOLECULAR SIMULATION OF GAS PERMEATION AND SEPARATION IN POLYMER MEMBRANES

FANG WEIJIE

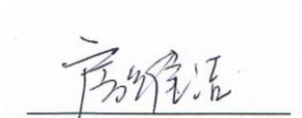NATIONAL UNIVERSITY OF SINGAPORE

2012

DECLARATION

I hereby declare that this thesis is my original work and it has been written by me in its entirety. I have duly acknowledged all the sources of information which have been used in the thesis.

This thesis has also not been submitted for any degree in any university previously.

Fang Weijie
12-Dec-2012

MOLECULAR SIMULATION OF GAS PERMEATION AND SEPARATION IN POLYMER MEMBRANES

FANG WEIJIE

(*B. Eng.*, Hebei University of Technology
M. Eng., Tianjin University)

A THESIS SUBMITTED

FOR THE DEGREE OF DOCTOR OF PHILOSOPHY

DEPARTMENT OF CHEMICAL AND BIOMOLECULAR ENGINEERING

NATIONAL UNIVERSITY OF SINGAPORE
2012

ACKNOWLEDGEMENTS

First and foremost, I would like to extend my deepest and sincerest appreciation to my supervisor Professor Jiang Jianwen. His invaluable guidance, unwavering support and encouragement have helped me develop in-depth understanding of my research subject and overcome considerable difficulties during my Ph.D. program. Prof. Jiang's passion and meticulous attitude in scientific research have deeply inspired me and set a wonderful example to me. I sincerely treasure this precious experience, which will be extremely valuable for my future professional career.

I would like to convey my gratitude to Professor Neal Chung Tai-Shung for his kind support for my Ph.D. study in the last four years. I would also like to express my sincere thanks to National Research Foundation for financial support and also to National University of Singapore for the opportunity to pursue my Ph.D. degree.

I would also like to extend my thanks to all my group members: Dr. Zhang Liling, Dr. Luo Zhonglin, Dr. Hu Zhongqiao, Dr. Ravichandar Babarao, Dr. Anjaiah Nalaparaju, Dr. Chen Yifei, Mr. Krishna Mohan Gupta, Mr. Huang Zongjun, Ms. Zhang Kang, and Mr. Naresh Thota.

Finally, I am deeply indebted to my parents and friends for their love, support, and encouragement during my Ph.D. program.

TABLE OF CONTENTS

SUMMARY

Polymer membranes have been widely used in industry for gas separation and are anticipated to play an increasingly important role in the development of new energy and environmental technologies. To understand the relationship between polymer structure and performance, deep insights into membrane properties such as chain mobility, free volume distribution, gas diffusion and sorption are crucial. With ever-growing computational power and advances in mathematical algorithms, molecular simulation has become an indispensable tool for materials characterization, screening and design. Through molecular simulation, this thesis aims to elucidate gas permeation and separation in two classes of newly synthesized polymer membranes, namely polymers of intrinsic microporosity (PIMs) and polymerized ionic liquids (PILs). These polymer membranes have recently attracted considerable interest because of their unique structures and properties; however, molecular-level studies on their performance in gas permeation and separation are scarce. The major content of the thesis consists of four parts.

1. Gas sorption, diffusion and permeation in two PIMs (PIM-1 and PIM-7) are simulated to compare their performance. The voids in both PIMs have diameter up to 9 Å and are largely interconnected. The solubility and diffusion coefficients are correlated well with the critical temperatures and effective diameters of gases, respectively. These molecular-based correlations can be used for the prediction of other gases. For CO_2/H_2, CO_2/O_2, and CO_2/CH_4 gas pairs, the simulated sorption, diffusion, and permeation selectivities match fairly well with experimental data. The quantitative microscopic understanding of gas permeation and separation in the two PIMs is useful for the new development of polymer membranes with high permeability and selectivity.

2. Permeation and separation of CO_2 and N_2 are examined in PIM-1 with various functional groups (cyano, trifluoromethyl, phenylsulfone, and carboxyl). A robust equilibration protocol is proposed to construct model membranes with predicted densities very close to experimental data. Hydrogen bonds are observed to form among carboxyl groups and contribute to the lowest fractional free volume in CX-PIM. *Ab initio* calculations reveal that the interaction energies between CO_2 and functional groups decrease as carboxyl > phenylsulfone > cyano > trifluoromethyl. To evaluate the gas separation performance the diffusion selectivity, sorption selectivity and permselectivity of CO_2 and N_2 were calculated. While the diffusion selectivity of CO_2/N_2 remains nearly constant, the sorption selectivity increases as PIM-1 < TFMPS-PIM < CX-PIM; consequently, the permselectivity follows the same hierarchy as the sorption selectivity. This study provides microscopic insight into the role of functional groups in gas permeation and suggests strong CO_2-philic groups should be chosen to functionalize PIM-1 membrane for high-efficiency CO_2/N_2 separation.

3. The effects of residual solvent in PIM-1 on membrane structure and H_2 permeation are studied since it remains elusive how residual solvent specifically interacts with PIM-1 membrane and affects membrane microstructure and performance. The effects of residual solvents on the diffusion and sorption of various gases are similar. Therefore, as a simple gas, H_2 is considered in this work. The interaction energies of three solvents ($CHCl_3$, CH_3OH and H_2O) with PIM-1 are -16.3, -9.6 and -7.0 kcal/mol, respectively, in good agreement with experimental data. The cyano and dioxane groups in PIM-1 interact preferentially with CH_3OH and H_2O; however, carbon atoms interact more strongly with $CHCl_3$. The mobility of residual solvent decreases in the order of $H_2O > CH_3OH > CHCl_3$. The solubility and diffusion coefficients of H_2 were predicted to investigate the effects of residual

solvents on gas permeation. The predicted solubility and diffusion coefficients of H_2 decrease in the same order, and they are in fairly good agreement with experimental coefficients. This study provides quantitative understanding for microscopic properties of residual solvent in a polymer membrane and reveals that residual solvent plays a crucial role in tailoring membrane structure and gas permeation.

4. CO_2 capture is examined by simulation in four polymeric ionic liquids (PILs) based on 1-vinyl-3-butylimidazolium ($[VBIM]^+$) and four anions bis(trifluoromethylsulfonyl)imide ($[TF_2N]^-$), thiocyanate ($[SCN]^-$), hexafluorophosphate ($[PF_6]^-$) and chlorine ($[Cl]^-$). In addition, two ILs [BMIM][TF$_2$N] and [BMIM][SCN] based on 1-butyl-3-methylimidazolium ($[BMIM]^+$) are also considered. The predicted densities, solubility parameters and vaporization enthalpies of the PILs and/or ILs match well with experimental data. In remarkable contrast to ILs, gas in PILs interacts with polycation more strongly than with anion and thus the effect of anions on gas solubility is marginal. Therefore, the gas solubilities predicted in poly([VBIM][TF$_2$N]), poly([VBIM][PF$_6$]), poly([VBIM][SCN]) and poly([VBIM][Cl]) are close, which also agree well with available measured data. Consistent with the increasing percentage of large voids, gas diffusivities in the four PILs increase as poly([VBIM][Cl]) < poly([VBIM][PF$_6$]) < poly([VBIM][SCN]) < poly([VBIM][TF$_2$N]). For CO_2/N_2 separation, the sorption, diffusion and permeation selectivities from simulation and experiment are consistent. The diffusion selectivities are approximately equal to one, implying the separation is governed by sorption. This study provides atomistic insight into the mechanisms of gas sorption, diffusion and permeation in $[VBIM]^+$-based PILs and suggests that polycation plays a dominant role in gas-membrane interaction and governs separation performance.

LIST OF TABLES

LIST OF FIGURES

TFMPS-PIM and CX-PIM.

NOMENCLATURE

α	Selectivity
β	Reciprocal temperature, $1/k_B T$
γ	Activity coefficient
δ	Solubility parameter
ε	Well depth of Lennard-Jones potential
ε_0	Permittivity of vacuum
θ	Scattering angle or bond angle
λ	Wavelength
μ	Chemical potential
μ^{ex}	Excess chemical potential
ρ	Density
φ	Dihedral angle
χ	Out-of-plane angle
$\vec{a}$	Acceleration
b	Langmuir affinity parameter or bond length
c	Concentration
d	d-spacing
d_c	Collision diameter
d_k	Kinetic diameter
d_{eff}	Effective diameter
k_B	Boltzmann constant, 1.38066×10^{-23} J/K
k	Elastic constant
k_D	Henry's constant

l	Membrane thickness
m	Mass
p	Pressure
Δp	Pressure difference
q	Atomic charge
r	Distance between atoms, bond length or radius
$\vec{r}$	Position of a particle
r^0	Equilibrium bond length
$\Delta \vec{\mathbf{r}}_i$	Displacement of a particle i
t	Time
Δt	Timestep
v	Molar volume
$\vec{v}$	Velocity
C	Penetrant concentration
$C_H^{'}$	Langmuir sorption capacity
D	Diffusion coefficient
E	Interaction energy
E_{coh}	Cohesive energy per mole
E_{vac}	Cohesive energy in vacuum
E_{bulk}	Cohesive energy in amorphous bulk state
$\vec{F}_i$	Force
ΔH^{vap}	Vaporization enthalpy
J	Flux
K_H	Henry's constant
L	Membrane intrinsic coefficient

N	Number of particles
P	Permeability
R	Universal gas constant
S	Solubility coefficient
$S_{selectivity}$	Selectivity
T	Temperature
T_c	Critical temperature
T_g	Glass transition temperature
U	Potential energy
U_b	Bond-stretching potential
U_θ	Bond-bending potential
U_φ	Torsional potential
U_{bonded}	Intramolecular potential
U_k	Kinetic energy
U_p	Potential energy
$U_{non\text{-}bonded}$	Intermolecular potential
U_{VDW}	van der Waals potential
U_Q	Coulombic potential
V	System volume
V_c	Critical volume
V_{vdw}	van der Waals volume
V_{sp}	Specific volume

ABBREVIATIONS

AMBER   Assisted Model Building with Energy Refinement

CHARMM   Chemistry at HARvard Macromolecular Mechanics

COMPASS   Condensed-phase Optimized Molecular Potentials for

Atomistic Simulation Studies

CED   Cohesive Energy Density

CFF   Consistent Force Field

CFF91   Consistent Force Field 91

COF   Covalent Organic Frameworks

CVFF   Consistent Valence Force Field

DFT   Density Function Theory

FFV   Fractional Free Volume

GCMC   Grand Canonical Monte Carlo

IL   Ionic Liquid

LJ   Lennard-Jones

MC   Monte Carlo

MD   Molecular Dynamics

MM   Molecular Mechanics

MMFF93   Merck Molecular Force Field93

MMMs   Mixed Matrix Membranes

MOFs   Metal-organic Frameworks

MP2   Second order Møller–Plesset

MSD   Mean Squared Displacement

PALS	Positron Annihilation Lifetime Spectroscopy
PC	Polycarbonate
PCFF	Polymer Consistent Force Field
PDMS	Polydimethylsiloxane
PEEK	Poly(ether-ether-ketone)
PEG	Polyethylene glycol
PEI	Polyetherimide
PET	Poly(ethylene terephthalate)
PI	Polyimide
PIM	Polymer intrinsic microporosity
PIL	Polymeric Ionic Liquid
PSf	Polysulfone
PTMSP	Poly[1-(trimethylsilyl)-1-propyne]
PVC	Poly(vinyl chloride)
RDFs	Radial Distribution Functions
SILM	Supported Ionic Liquid Membrane
TST	Transition State Theory
VSD	Void Size Distribution
VVA	Velocity Verlet Algorithm
WAXD	Wide Angle X-ray Diffraction
[BMIM]$^+$	1-butyl-3-methylimidazolium
[VBIM]$^+$	1-vinyl-3-butylimidazolium
Poly[BIM]$^+$	poly[2-(1-butylimidazolium-3-yl)ethyl methacrylate]$^+$
Poly[MABI]$^+$	poly[1-[2-(methacryloyloxy)ethyl]-3-butyl-imidazolium]$^+$
Poly[VBBI]$^+$	poly[1-(p-vinylbenzyl)-3-butyl-imidazolium]$^+$

Poly[VBI]$^+$ poly[1-(4-vinylbenzyl)-3-butylimidazolium]$^+$

Poly[VBTMA]$^+$ poly[(*p*-vinylbenzyl)trimethylammonium]$^+$

[TF$_2$N]$^-$ Bis(trifluoromethylsulfonyl)imide

[BF$_4$]$^-$ Tetrafluoroborate

[Cl]$^-$ Chlorine anion

[Sac]$^-$ o-benzoicsulphimide

[SCN]$^-$ Thiocyanate

[PF$_6$]$^-$ Hexafluorophosphate

CHAPTER 1 INTRODUCTION

1.1 Polymers for Gas Permeation and Separation

Early observation of gas permeation in polymers can be traced back to the 19th century. In 1830's, Mitchell first observed gas diffusion in a natural rubber [1]. After approximately 30 years, Graham reported the first quantitative measurement of gas permeation and proposed solution-diffusion model [2,3]. This model suggests that gas flux is governed by sorption and diffusion, and has been widely used to elucidate gas permeation process in polymer membranes. Later, Wroblewski quantitatively defined the concept of permeability and discussed the relationship between gas permeability and other factors such as flux, membrane thickness, and pressure gradient [4]. Furthermore, Wroblewski proved that permeability is equal to the product of solubility and diffusivity. These early studies are the solid foundation for subsequent studies of gas permeation and separation in polymer membranes.

Before 1950's, most polymers investigated for gas permeation were natural rubbers. The advent of synthetic polymers appeared in late 1950's to 1970's; thereafter, synthetic polymers were systematically studied by examining the effects of molecular mass, chemical structure, cross-linking, etc. It is worth to note that most polymers considered during this period were rubbery polymers with low glass transition temperatures (T_g). However, rubbery polymers have low modulus and are not easy to be fabricated into thin, self-supported, and pressure-resistant membranes. After 1970's, advanced polymer materials appeared, particularly glassy polymers with high T_g. In general, glassy polymers exhibit higher gas selectivity than rubbery polymers and attract more attention.

1

To choose a polymer membrane for gas separation, the following factors should be considered: (1) high flux and high separation efficiency (2) good thermal resistant (3) good mechanical strength (4) low cost and (5) engineering feasibility [5]. On this basis, the commonly investigated polymers include polyimides (PIs), polysulfones (PSfs), poly[1-(trimethylsilyl)-1-propyne] (PTMSP), polyphosphazenes, polycarbonates, etc. Among these polymers, PTMSP has ultra-high gas permeability, comparable to that of rubbery polymers, as attributed to the large free volume. However, gas selectivity in PTMSP is exceptionally low.

It has been well recognized that a polymer membrane with high permeability is coupled with low selectivity, and vice versa. In this context, Robeson proposed an 'upper bound' or 'trade-off' between permeability and selectivity. The upper bound was first reported in 1991 [6] and then revised in 2008 [7]. Each gas pair has a unique upper bound, e.g., as shown in **Figure 1.1** for CO_2/N_2 and O_2/N_2. The upper bound provides an empirical guidance on the performance of polymer membranes for gas separation. A polymer membrane exhibiting good performance in separating one gas pair usually also performs well another gas pairs. The α and P (defined in **Section 1.3.3**) represent gas selectivity and permeability, respectively.
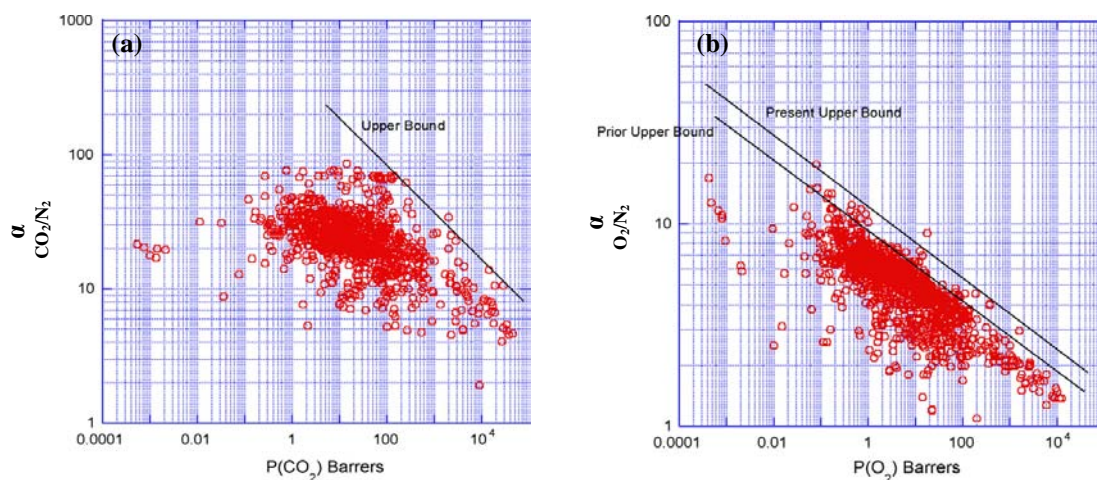
Figure 1.1 Robeson upper bound 2008 for (a) CO_2/N_2 (b) O_2/N_2.

With the objective to achieve high performance for gas separation, continuous efforts have been attempted to develop new polymer membranes that may exceed the upper bound. For instance, functionalized polymers [8-10], block copolymers [11-13], polymer blends [14-18], mixed-matrix membranes [19-26], chemically cross-linked [27-31], grafted polymers [32-34], and thermally annealing polymers [35-38] have been explored for gas separation. Most these modified polymers are effective to tailor membrane structures and enhance membrane performance.

1.2 Industrial Applications

A handful of technologies are used in the market for gas separation, such as cryogenic distillation and pressure swing adsorption. These technologies are energy intensive, quite mature, and little room available for further improvement. As a comparison, polymer membranes offer several advantages for gas separation [39-43]:

1. Easy for installation, operation, and scaling up

2. Low capital cost and energy consumption,

3. Small footprint,

4. Compatible with other units and easy to be integrated into a separation system.

Several decades ago, polymer membranes fabricated were thick and exhibited low gas flux. Therefore, large membrane areas would be required to overcome the deficiency of low flux. This was the primary obstacle to commercialize polymer membranes from laboratory to industrial scale. One solution to this obstacle was the invention of asymmetric polymer membranes achieved by Loeb and Sourirajan when they prepared cellulose acetate membranes for reverse osmosis [44]. Another breakthrough was the development of hollow fiber membranes by Monsanto [45]. Since then, polymer membranes have been increasingly used for gas separation in industry. The business of polymer membrane-based gas separation increased from

120 M\$ in 1996 to 250 M\$ in 2000 (M\$: million US dollar). Despite relatively small percentage in the whole global market, polymer membrane-based gas separation shows extremely promising perspective.

Most gas separation processes involve gas mixtures such as CO_2/CH_4 (acid gas treatment in natural gas), O_2/N_2 (oxygen enrichment), H_2/hydrocarbons (hydrogen recovery), CO_2/N_2 (carbon capture), H_2/CO (syngas ratio adjustment), etc. In 1977, Monsanto invented the first commercial polymer membrane named as Prism$^®$ to produce H_2 [45]. This success encouraged other companies to develop their own membranes for gas separation. In the mid-1980's, Generon fabricated poly(4-methyl-1-penetene) membrane to separate N_2 from air. Meanwhile, Cynara, UOP, and GMS produced cellulose acetate membranes to separate CO_2 from natural gas [43]. In 1985, Ube Industries Ltd. developed a PI-resin hollow fiber membrane for H_2 recovery. Signal Company produced silicone membrane with a porous PSf-support for O_2 recovery.

Table 1.1 Commercial polymer membranes for gas separation.

Company	Principal market	Membrane material
GKSS	Dehydration	Silicone
Monsanto	Hydrogen	PSf
IMS	Hydrogen	PI
Medal	Nitrogen	PI/Polyaramide
GMS	Methane	Cellulose acetate
UOP	Carbon dioxide	Cellulose acetate
Cynara	Carbon dioxide	Cellulose acetate
Ube	Hydrogen	PI
Signal	Oxygen	PSf-supported silicone
Dow	Oxygen	Polyolefin
GASEP$^®$	Sour gas	Cellulose triacetate

To date, numerous polymer membrane-based separation systems have been constructed worldwide. For instance, there are more than 230 Prism®-based systems for different separation applications, including ammonia process, petrochemical, oil refinery, and CO_2 removal. It is interesting to point out despite extensive studies conducted on a wide variety of polymer membranes, only a few membranes as listed in **Table 1.1** have been commercialized for gas separation. However, these membranes possess at least 90% market of polymer membrane-based separation.

1.3 Basic Concepts

In this Section, basic concepts commonly used for gas permeation and separation in polymer membranes will be presented, including solution-diffusion mechanism, free volume, permeability, and selectivity.

1.3.1 Solution-Diffusion Mechanism

Solution-diffusion mechanism was firstly proposed by Graham [2] and has been widely used to elucidate gas permeation in polymer membranes. The basic idea is that gas first dissolves at feed side, then diffuses through the membrane under a concentration gradient, and finally desorbs at permeate side. Several assumptions can be further introduced in this process: (1) the rates of gas adsorption and desorption at the membrane interfaces are assumed to be substantially higher than the transport rate in the membrane, and thus the time for adsorption and desorption can be neglected. (2) gas transport on either side of the membrane is in equilibrium, leading a continuous gradient of chemical potential in the membrane. (3) pressure in the membrane is approximately uniform [46,47]. Based on these assumptions, the solution-diffusion process is schematically shown in **Figure 1.2**. It can be derived that permeability P is a product of a thermodynamic factor (solubility) and a kinetic factor (diffusivity)

$$P = S \cdot D \qquad\qquad (1\text{-}1)$$

For a gas mixture, separation in the membrane is achieved by the difference in solubility and diffusivity.
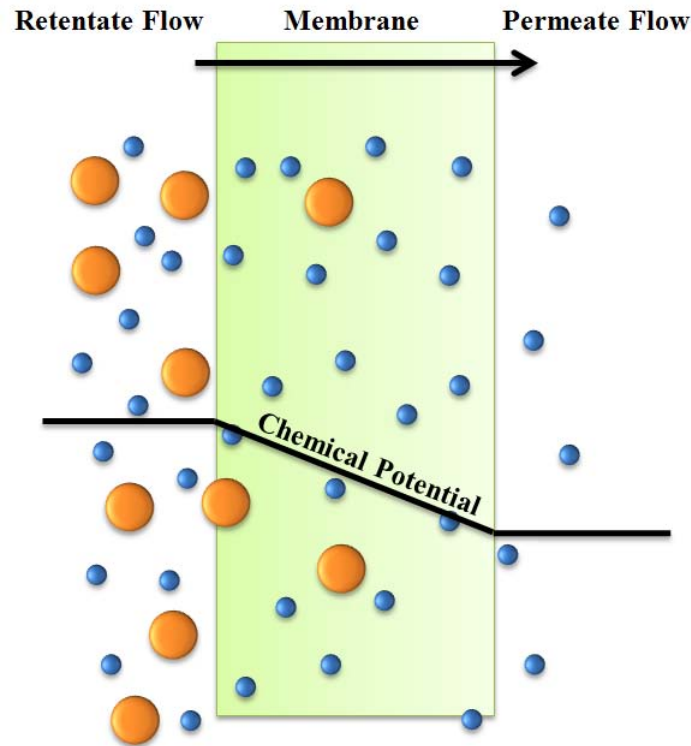
Figure 1.2 Schematic representation of solution-diffusion mechanism. The orange and blue spheres represent gas molecules with different sizes.

1.3.2 Free Volume

Free volume in a polymer membrane plays a central role in governing the diffusion of penetrant. In a polymer network, polymer chains fluctuate and thus create free volume. **Figure 1.3** shows the diffusion of penetrant in a polymer network from the initial to next position. The diffusion consists of a series of jumps through temporary free volumes (cavities) created by polymer chains. Initially, penetrant exhibits rapid oscillation within the cavities. Due to the movement of polymer chains, the 'old' cavities are closed and 'new' cavities are created. Therefore, the diffusion of penetrant

is facilitated. Consequently, the mobility of polymer chains, free volume, and penetrant size are the primary factors governing the diffusion.
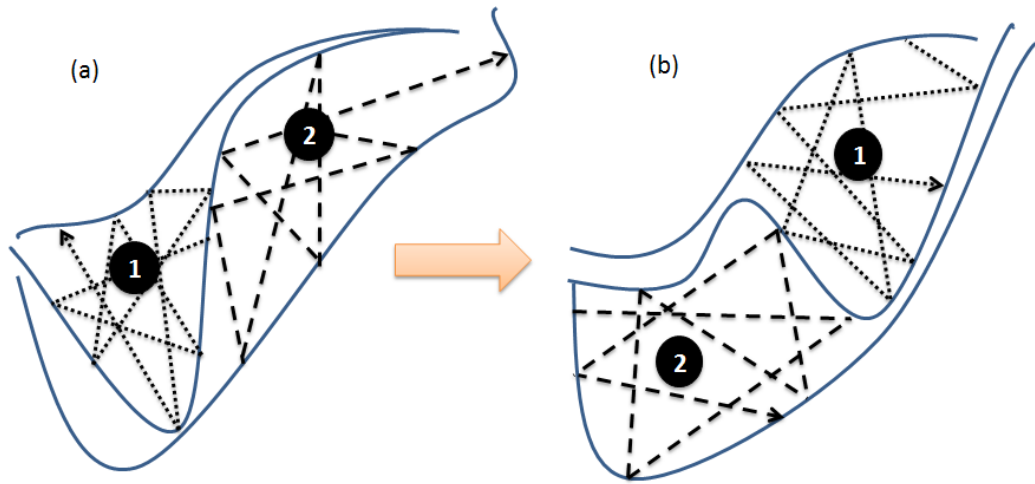
Figure 1.3 Penetrant diffusion in a polymer network from (a) initial (b) next position.

Free volume is usually expressed as fractional free volume (FFV), which is the ratio of free volume to specific volume in a membrane. In other words, FFV is the fraction of the volume not occupied by polymers. Various experimental methods can be used to measure free volume, such as positron annihilation lifetime spectroscopy (PALS) [48,49], low-pressure N_2 adsorption [50], Xe sorption and ^{129}Xe NMR spectroscopy [51], wide angle X-ray diffraction (WAXD) [52]. Alternatively, free volume can also be estimated by theoretical or simulation methods, e.g. Williams-Landel-Ferry equation [53], Bondi group contribution [54], Voorintholt method [55], and energetic-based cavity-sizing method [56].

1.3.3 Permeability and Selectivity

In any polymer membrane, permeability is an important intrinsic transport property. Based on flux and membrane thickness, permeability can be evaluated by

$$P = \frac{J \cdot l}{\Delta p} \tag{1-2}$$

where J is flux, l is membrane thickness and Δp is pressure difference across the membrane. In the SI unit, permeability is expressed as $mol \cdot (m^2 \cdot s \cdot Pa)$. Nevertheless, the more commonly used unit is barrer

$$1 \text{ barrer} = 10^{-10} \text{ cm}^3(\text{STP}) \text{ cm}/(\text{cm}^2 \text{ s cmHg}) \tag{1-3}$$

The other approach to estimate permeability is via equation (1-1). Apparently, permeability depends on both solubility and diffusivity.

To quantify the capability of a membrane for separation, the selectivity between components A and B is estimated by the ratio of their permeabilities

$$\alpha = \frac{P_A}{P_B} \tag{1-4}$$

where P_A and P_B are the permeability of components A and B, respectively. The selectivity can be calculated from either pure-gas permeability or mixed-gas permeability. Usually, the pure- and mixed-gas selectivities are different due to mixing effect. In some rubbery membranes, however, they are close to each other [57].

1.4 Scopes and Outline of the Thesis

The development of new polymer membranes for gas separation by experiment alone is a very laborious process. Towards this end, deep understanding of membrane structures and properties from molecular simulation is indispensable. With the ever-growing computational power and advances in mathematical algorithms, simulation has become a robust tool in polymer sciences and engineering. Insights provided by simulation are useful for the characterization, screening and design of novel polymer membranes for high-performance gas separation.

In this thesis, simulation is applied to investigate gas permeation and separation in two newly synthesized polymer membranes, namely polymers of intrinsic

microporosity (PIMs) and poly(ionic liquid)s (PILs). With unique chemical structures, these two polymers exhibit outstanding performance. However, few/no simulation studies have been reported on PIMs/PILs. This thesis aims to investigate their performance in gas permeation and separation from a microscopic level. Specifically, the scopes of the thesis include (a) two PIM membranes with different structures (b) effects of functional groups on gas separation (c) effects of residual solvent on membrane structure and gas permeation (d) CO_2 capture in PILs.

The thesis consists of eight chapters. The current Chapter is to introduce polymer membranes for gas separation. Chapter 2 is focused on the literature review of simulation studies for gas permeation and separation in polymer membranes, as well as experimental studies in PIMs and PILs. A basic knowledge about simulation methodology used in this thesis is briefly described in Chapter 3. Chapter 4 represents the simulation results of PIM-1 and PIM-7 membranes. In Chapter 5, the effects of functional groups on gas separation are simulated. Chapter 6 examines the effects of residual solvents (CH_3OH, $CHCl_3$ and H_2O) on membrane structure and gas permeation. In Chapter 7, the first simulation study is reported for CO_2 capture in PILs with a common polycation but different anions. Finally, conclusions and future work are summarized in Chapter 8.

CHAPTER 2 LITERATURE REVIEW

Molecular simulation of polymer membranes was initially reported about 50 years ago [58-62]. With the continuous growth of computational power, simulation has been increasingly used in the past a few decades to examine polymer membranes. In this Chapter, a literature review is focused on the simulation studies of polymer membranes for gas permeation and separation. Firstly, simulation studies are presented in Section 2.1 for a number of common polymer membranes, such as polyolefins, polysiloxanes, poly[1-(trimethylsilyl)-1-propyne], polyimides, polysulfones, polycarbonates, and mixed-matrix membranes. In Sections 2.2 and 2.3, experimental studies and available simulation reports are presented for polymers of intrinsic microporosity and poly(ionic liquid)s. These two polymer membranes are specifically investigated in this thesis.

2.1 Molecular Simulation Studies

Polyolefins

Polyolefins are one of the most important and widely used petrochemical products. Early simulation studies in polyolefins were focused on gas diffusion, and later also on gas sorption. Takeuchi and Okazaki simulated the diffusion of small penetrants in polymethylene with 20 repeat units, and found both fractional free volume (FFV) and void size distribution (VSD) played a dominant role in governing diffusion rate [63]. Choi et al. observed that increasing polyethylene chain rigidity would lead to a decreased gas diffusivity but increased selectivity [64]. Simulation of O_2 diffusion in butadiene-styrene copolymer showed that the diffusivity of O_2 was related to polymer chemical structure and FFV [65]. Pricl et al. conducted a detailed simulation study of gases (He, Ne, O_2, N_2, and CO_2) in ten polyolefins [66]. The calculate properties such

as polymer density, solubility parameter, and gas diffusivity agreed well experimental results. Boyd et al. investigated CH_4 diffusion in polyethylene membrane over a wide range of temperature from 300 to 400 K, and observed a hopping-jumping mechanism [67]. Similar mechanism was also observed for CH_4 in *cis*-1,4-polybutadine [68] and CO_2 in amorphous polyethylene melt [69] and in polystyrene [70]. It is interesting to note CH_4 diffusion in polyethylene showed a non-Arrhenius dependence on temperature [68,69]. Additionally, Boyd and co-workers also examined CH_4 diffusion in atactic polystyrene [71] and *cis*-1,4-polybutadiene [68] using united-atom simulation. The results revealed that glass transition occurring in temperature range from 380 to 500 K had a negligible effect on CH_4 diffusion. Müller-Plathe studied H_2, O_2 and CH_4 diffusion in atactic polypropylene and suggested a polymer model with well-equilibrated starting structure should be used to improve the accuracy of simulation results [72]. A good correlation was identified between diffusivity and molecular size. Boshoff et al. investigated the effects of polymer motion and model size on He diffusion in atactic polypropylene [73]. It was unraveled that polymer motion plays an important role in gas diffusion, changing from activated diffusion in flexible polymer chains to kinetic motion in frozen polymer chains. Moreover, anomalous diffusion time could be reduced using a large sized molecular model.

As pointed out early, gas permeation in polymer membranes is based on solution-diffusion mechanism. In addition to diffusion, sorption in polyolefins has been reported in simulation studies. van der Vegt estimated Gibbs free energies, solvation entropies and solvation enthalpies of various gases (He, Ne, H_2, CO_2, CH_4, etc) in polyethylene [74]. Using osmotic ensemble, Lachet et al. simulated the solubilities of N_2, CH_4 and CO_2 in semicrystalline polyethylene [75,76]. Good agreement was obtained between experimental and simulated solubilities of CO_2, suggesting that

accurate description of the permeable phase of a polymer membrane is important. In addition, the simulated solubilities of gas mixtures (CH_4/CO_2 and CH_4/H_2) were also consistent well with experiments [77]. Sanguigno et al. investigated CO_2 sorption, particularly the maximum adsorption capacity and preferential orientation of CO_2 in crystalline syndiotactic polystyrene using grand canonical Monte Carlo (GCMC) simulation [78]. Combining *NPT* and pseudo-μVT ensemble molecular dynamics (MD) simulations, Eslami and Plathe examined Ar, H_2, N_2, CO_2, CH_4, and C_3H_8 in polystyrene [79]. Whilst the calculated solubilities were constantly higher than measured values, the solubility selectivities were in good accordance with experiments.

Polysiloxanes

Polysiloxanes, also known as the silicones, are hybrid organic-inorganic rubbery polymers. They are composed by inorganic Si-O polymer backbone and organic polymer side chains such as halogens and alkyl groups. Charati and Stern simulated gas (He, O_2, N_2 and CH_4) diffusion in four silicone polymers using CFF91 force field [80]. The calculated properties such as density and cohesive energy density were consistent with experimental data, and diffusivity was very sensitive to model density. In addition, two modes of motion were observed including 'jumping' from one void to the other, and 'oscillating' inside a cavity. The influence of force field on gas permeation in polysiloxanes was examined by Segooa et al. [81] Upon comparison with PCFF, it was found the diffusion and solubility coefficients predicted from COMPASS force field were in better agreement with experimental data.

As the most widely used polysiloxanes, polydimethylsiloxane (PDMS) is highly permeable. Sok et al. simulated gas (He and CH_4) diffusion in PDMS and observed hopping mechanism [82]. Because of the difference in size and polarizability between

He and CH_4, the residence time of He atom in a cavity was found to be much shorter than that of CH_4. Consequently, He exhibited nearly free diffusion, while CH_4 diffusion was majorly governed by the fluctuation frequency of polymer chains. Tamai et al. compared the diffusion and sorption of CH_4, H_2O and ethanol in PDMS and polyethylene [83-85]. The results showed that the diffusion coefficients in PDMS were larger than in polyethylene due to the broader VSD and larger FFV in PDMS. Ethanol exhibited a higher solubility than H_2O in both PDMS and polyethylene because of the stronger interaction between ethanol and polymers. The calculated permeabilities were in reasonable agreement with experimental data.

Poly[1-(trimethylsilyl)-1-propyne]

Poly[1-(trimethylsilyl)-1-propyne] (PTMSP) is a glassy polymer with exceptionally high permeability, which is comparable with or even higher than that in rubbery membranes (e.g. PDMS). From MD simulation, Yang et al. examined the difference of gas diffusion in PTMSP and PDMS [86]. Despite a higher rigidity of PTMSP chain, the diffusion coefficients of He and Ne in PTMSP were found to be higher than in PDMS. This was attributed to a higher FFV in PTMSP, suggesting the FFV is a dominant factor in gas diffusion. Fried and Goyal studied He, O_2, N_2, CO_2 and CH_4 diffusion in PTMSP [87]. The calculated diffusion coefficients of all the gases except CO_2 were consistent with experimental data. The authors suggested that the large discrepancy seen for CO_2 was due to the inappropriate force field parameters used. They also simulated the sorption of pure alkanes (CH_4, ethane, propane, and *n*-butane) and H_2/alkane mixture in PTMSP using GCMC method [88]. The solubility coefficients calculated at low pressures were satisfactory, but not at high pressures. Hofmann et al. conducted a comparison study for PDMS, PTMSP and PIs [89]. The density of PTMSP was predicted to be larger ($1.22 \ g/cm^3$) than experiment (c.a. 0.7 -

0.8 g/cm^3). This suggested the low experimental density was not the intrinsic 'equilibrium' density and two states of PTMSP could exist: fresh polymer (low density, non-equilibrium state) and physical aging polymer (high density, equilibrium state). The calculated diffusion coefficients of He and Ne in PTMSP were higher than in PDMS. Additionally, Hofmann et al. demonstrated that the combination of PALS experiment and molecular simulation could provide a better understanding of VSD by examining PTMSP and two polystyrene derivatives [90]. A much wider VSD (1.1 - 9 Å) in PTMSP was observed than two polystyrene derivatives (1.1 - 4.5 Å). Freeman and co-workers simulated gas diffusion in PTMSP and it derivatives, and found the addition of bulky benzene groups would increase the FFV and gas diffusion coefficients [91].

Polyimides

Since massive production in 1955, polyimides (PIs) have been widely used in industry for gas separation because of their high mechanical, thermal, chemical stabilities and excellent separation performance. Consequently, a larger number of simulation studies have been reported in PIs. Smit et al. examined CO_2 diffusion in 6FDA-4PDA and 6FDA-44ODA membranes and identified three types of motions (jumping, continuous, and trapped) in these PIs [92]. The diffusion coefficient obtained was three orders of magnitude larger than experimental value; the authors suggested that the short chain length, chain-end effect, and short simulation time (< 200ps) might account for the large discrepancy. Heuchel and Hofmann calculated solubility and diffusion coefficients of N_2, O_2 and CO_2 in seven PIs (6FDA-durene, 6FDA-3MPD, 6FDA-6MTP, 6FDA-TMB, 6FDA-BAAF, 6FDA-ODA, and PMDA-ODA) using transition state theory (TST) [93-95]. The estimated diffusion and solubility coefficients of O_2 and N_2 were in good agreement with experimental data.

For CO_2, however, the solubility coefficient was constantly higher in all PIs and the diffusion coefficient was 1-2 orders of magnitude lower compared to experimental measurement. A plausible reason was the TST failed to incorporate the structural relaxation of PIs due to the strong interaction with CO_2. In another study, they also observed that the diffusion and solubility coefficients of O_2, N_2 and CH_4 in ten PIs agreed well with experimental data, but not of CO_2 [96]. Zhang and Mattic investigated the diffusion of O_2 and N_2 in a PI polymer named as PI-2 at 500 K using MD simulation [97]. The calculated diffusion coefficients and selectivity agreed well with experimental results. In addition, the residence time of O_2 in cavity was estimated to be in the order of 100 ps, much larger than the translational motion of 10 ps. Shimazu et al. discussed the relationship between the molecular structure of 6FDA-BAAF with d-spacing, which is of central importance for gas permeation [98]. The calculated d-spacing agreed well with measurement and was affected by the intramolecular distance of fluorine-containing PIs. Hofman et al. examined the sorption and diffusion of H_2, O_2 and N_2 in PIs and poly(amide imide)s using Widom insertion and MD method, respectively [99]. H_2 exhibited predominantly Henry sorption pattern, while O_2 and N_2 showed Langmuir-type adsorption behavior. The simulated diffusion coefficients were higher than experimental data and could be improved by a longer simulation time and/or a larger membrane model.

It is well recognized that CO_2 sorption in PIs can lead to plasticization and reduced gas selectivity. Combining experimental and simulation techniques, Zhang et al. investigated CO_2-induced plasticization in 6FDA-ODA membrane [100]. From structural analysis, it was identified that imide groups were the preferential sorption sites. The calculated CO_2 sorption isotherm was in fairly good agreement with experimental measurement. The results revealed that CO_2 molecules were largely

trapped at low CO_2 loading, but enhanced with increasing CO_2 loading. Neyertz et al. studied CO_2 sorption and desorption in fluorinated PIs [101,102]. Good agreement between simulation and experiment was obtained such as CO_2 sorption and desorption and volume expansion of plasticized PIs. The simulation suggested polymer swelling could be attributed to the strong interactions between CO_2 and PIs.

The FFV and VSD are key factors to gas permeation and have been estimated by simulation in PIs [96,103]. Heuchel et al. examined the permeation of N_2, O_2, CH_4 and CO_2 in ten PIs and discussed the correlation between permeability and VSD [96]. It was suggested that a large-sized void plays a more important role in high permeability. In order to produce large voids, PIs should contain large substitution side groups such as methyl in the ortho position and maintain the 'stiffness' of amine moiety. Using MC and MD simulations, Chang et al. investigated the effects of residual solvent on gas separation performance in 6FDA-mPDA [104,105]. The residual solvent was found to increase chain mobility, free volume, gas diffusivity and solubility. In addition, bulky groups contributed to the formation of a large free volume and continuous cavities. Pandiyan et al. characterized three fluorinated PIs and found the differences of density, FFV and VSD in the three PIs were negligible [106].

Polysulfones

Polysulfones (PSfs) are commercially important polymers for industrial gas separation and have been attracted considerable attention [107-113]. Niemelä et al. simulated the effects of polymer structure on FFV and VSD in various PSfs [114]. PSfs with asymmetric structure were found to be more densely packed than the symmetric counterparts. Moreover, the substitution of methyl group in PSfs produced larger void and wider VSD. Hölck et al. examined volume dilation induced by sorbed

gases (CO_2 and CH_4) in PSfs and PIs [115]. They suggested the different dilation behavior by CO_2 sorption in PSfs and PIs could be attributed to different stiffness of polymer chains. Furthermore, they simulated CO_2 sorption in PSf at 308 K and pressures up to 50 bar [116]. It was found the dilation of PSf during CO_2 sorption could be separated into two regimes (diffusive/elastic and relaxational). Wang et al. conducted gas diffusion in *meta-* and *para-* PSfs and found that *para-*PSf had a larger cavity and a higher diffusion coefficient than *meta-*PSf [117].

Polycarbonates

Polycarbonates (PCs) have large selectivity for gas separation, large FFVs and good mechanical properties. Gusev et al. investigated He diffusion in bisphenol-A PC in temperature range from 110 to 300 K [118]. The diffusion showed an Arrhenius behavior versus temperature, and simulated and experimental diffusion coefficients were in the same order of magnitude. Gentile et al. used Delaunay tessellation method to calculate the FFVs of tetramethyl and tetrabromo derivatives of bisphenol-A PCs [119]. A good correlation was found to exist between the logarithm of diffusion coefficients of four gases (He, O_2, N_2 and CH_4) and the inverse of FFVs. Similarly, Arizzi et al. analyzed the FFVs of atactic polypropylene and bisphenol-A PC, in which penetrant was modeled as a hard sphere and a glassy polymer was represented as a rigid matrix of hard spheres [120]. López-González et al. demonstrated that TST could be a promising tool to predict gas permeation and separation in PCs [121].

Mixed-Matrix Membranes

Mixed-Matrix Membranes (MMMs) are hybrid membranes composed by polymer matrices filled with nanoparticles. Compared to neat polymer membranes, MMMs have stronger mechanical strength. Zhou et al. simulated gas diffusion in silica-filled PTMSP and found diffusion coefficients were enhanced upon adding silica particles

[122]. This was associated with the increase of FFV in PTMSP; however, diffusion coefficient decreased when silica particle size increased. Yang et al. also observed a higher ratio of large voids in poly(4-methyl-2-pentyne)/silica MMM compared to neat poly(4-methyl-2-pentyne) and a higher gas diffusion coefficient [123]. Hanson et al. investigated the diffusion of CO_2 and N_2 in polystyrene/C_{60} fullerene MMM using kinetic MC simulation [124]. The diffusion coefficients of CO_2 and N_2 were found to decrease with the addition of C_{60} fullerene particles. Rallabandi et al. examined the permeation of He and Ne in polymethylene/graphite MMM and found graphite loading in polymethylene could be used to tune gas permeability [125].

Other Polymers

Simulation studies have been also reported on other polymers, such as poly(ether-ether-ketone) (PEEK), poly(vinyl chloride) (PVC), poly(organophosphazenes), etc [126-132]. Tocci et al. examined the diffusion of O_2, CO_2, N_2 and CH_4 in cardo, sulfonated and nitrated PEEK membranes using TST-MC method, and found the modification of polymer structure substantially changed gas permeation [133,134]. Campa et al. explored the structure-property relationship of different poly(ether ketone)s and observed that bulky groups could significantly enhance gas permeability due to the increase of FFV [135].

Tiemblo et al. conducted a comparative study for gas permeation in PVC using experimental and simulation methods [136]. The simulated permeabilities from diffusion and solubility coefficients were in very good agreement with experimental results. Sacristan and co-workers presented a detailed investigation for PVC and fluorothiophenol modified PVC in temperature range of 375 – 450 K [137]. The modified PVC displayed a less ordered chain packing structure owing to the incorporation of bulky side groups, and exhibited a larger FFV and a higher gas

diffusivity. Moreover, gas diffusion mechanism was found to change from solid-like pattern at low temperatures to liquid-like pattern at high temperatures.

Fried et al. conducted a series of simulation studies on the diffusion and sorption of He, O_2, N_2, CH_4 and CO_2 in poly(organophosphazenes) [138-141]. The calculated diffusion and solubility coefficients were in good agreement with experimental results. In addition, diffusion coefficients were correlated well with the effective gas diameters, while a good correlation was found between solubility coefficients and the Lennard-Jones interaction strength. *Ab initio* calculations were employed to estimate the interactions of CO_2 with substituent groups in poly(organophosphazenes). CO_2 was observed to interact favorably with fluoroalkyl group, and pair-correlation function analysis showed strong interaction of CO_2 with trifluoromethyl group.

It is worthwhile to point out that poly(ethylene terephthalates) (PETs) are widely used for food packaging and thus simulation studies of O_2, N_2 and CO_2 permeation in PETs have been conducted [126,127,129,142]. Similar simulation studies have also been reported for O_2, N_2 and CO_2 permeation in polymethylmethacrylate [143] and polyvinyl alcohol polymers [144-146].

2.2 Polymers of Intrinsic Microporosity

In the continuous quest for novel polymer membranes, a new class of polymers, namely polymers of intrinsic microporosity (PIMs) has been synthesized [147-149]. PIMs are amorphous, glassy, and thermally stable. Independent on fabrication or processing history, microporosity exists in PIMs intrinsically due to unique rigid structures. As ladder polymers, PIMs have double stranded chains as illustrated in **Figure 2.1**. Consequently, PIMs generally possess rigid polymer chains which are difficult to bend. Moreover, PIMs consist of spiro-centers (i.e., a single tetrahedral

carbon atom shared by two five-membered rings). The spiro-center contributes to contortion and microporosity. Therefore, PIMs show unique structures and gas separation performance as compared to traditional polymer membranes.
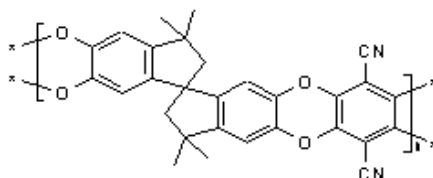
Figure 2.1 Schematic structure of PIM-1.

Several reviews have given detailed description on the structures and properties of PIMs [149-152]. Remarkably, PIMs are potentially useful for gas separation [151,153-155] storage [156-158], and heterogeneous catalysis [147,159,160]. A number of experimental studies as well as few simulation studies have been reported for gas permeation in PIMs, as presented below.

2.2.1 Experimental Studies

In 2003, Budd et al. first synthesized seven PIMs (PIM-1 to PIM-7)[161]. Gas separation measurements showed that PIM-1 and PIM-7 have excellent separation capability, exceeding the Robeson upper bound of 1991 [162]. Thereafter, PIMs have attracted considerable interest. Miranda et al. measured the free volumes in PIM-1 and PIM-7 using PALS, and found the average void radius in PIM-1 and PIM-7 is about 0.48 nm [163]. Ghanem and co-workers also demonstrated that PIM-7 has superior properties such as high surface area, good film-forming capability, and gas separation performance [164]. Staiger et al. investigated gas separation, void distribution, and physical aging in PIM-1 [155]. High gas permeability in PIM-1 was attributed to high solubility and diffusivity. It was found that gas permeability in PIM-1 decreased rapidly when residual solvent existed in PIM-1 during membrane-forming process.

Thomas et al. measured pure- and mixed-gas permeation and separation (*n*-butane/CH_4) in PIM-1 and compared to those in PTMSP and PDMS [153]. The selectivity in PIM-1 was similar to that in PTMSP, but 2.5-fold higher than in PDMS. In addition, PIM-1 showed excellent chemical resistance to hydrocarbons than PTMSP. Budd et al. found that gas permeability decreased if PIM-1 contacted with water during membrane preparation, but increased if soaking with methanol [165].

To further enhance gas separation performance, PIM-1 has been modified using different approaches. Du et al. conducted a series experimental studies to prepare PIM-1 derivatives by adding various functional groups such as disulfone [166], trifluoromethyl and phenylsulfone [52], dinaphthyl and thianthrene [167,168], carboxyl groups [169], and azide-based cross-linker [170]. Compared to original PIM-1, the functionalized PIM-1 membranes improved selectivity despite decreased permeability. Using tetrazole group, they also prepared a functionalized PIM-1 exhibiting unexpectedly and surprisingly good performance in CO_2/N_2 separation, far beyond the Robeson upper bound of 2008 [171]. More interestingly, mixed CO_2/N_2 selectivity in this polymer was substantially higher than pure CO_2/N_2 selectivity, which is an unusual phenomenon for gas separation in polymer membranes. Alternatively, Li et al. prepared a novel thermally self-cross linked PIMs, which showed high performance in gas separation, exceeding the Robeson upper bound of 2008 [172].

2.2.2 Simulation Studies

To date, only very few simulation studies have been reported on PIMs. Heuchel et al. built a molecular model of PIM-1 and examined gas permeation properties [173]. The predicted void distribution was consistent with experimental result (measured by sorption and further estimated by Horvath-Kawazoe method). From N_2 sorption

isotherm, it was suggested that PIM-1 behaves as a typical microporous material. Using a united atom model for PIM-1, Larsen et al. calculated the adsorption isotherm of CH_4 [174]. The density, void distribution, and surface area of PIM-1 were calculated and compared to experimental data. The discrepancy between experiment and simulation was attributed to three main factors, including residual solvent in experimental sample, film-forming history, and kinetically inaccessible voids in experimental sample. Furthermore, they also used a reverse MC method to build molecular models for PIM-1 and two bifunctional polymers, named PIM-1c and PIM-1n [175]. A new generic scheme called 21-step compression-relaxation scheme was used to equilibrate model membranes attempting to achieve experimental data. Recently, Zhao et al. reported a comparative study for H_2 and CH_4 adsorption in PIM-1 and silicalite-1 zeolite [176]. The results revealed that PIM-1 has CH_4 sorption capacity 60-68% higher than silicalite-1.

To the best of our knowledge, Ref. 173 - 176 are the only 4 simulation studies reported on PIMs. Thus, microscopic understanding of gas permeation and separation in PIMs is far from complete. A number of important issues need to be further addressed, e.g., the relation between membrane structure and permeation, the effects of functional groups as well as residual solvents. These issues will be investigated in this thesis by simulation.

2.3 Polymeric Ionic Liquids

As a unique class of solvents, ionic liquids (ILs) are molten salts at room temperature. With nonvolatile/nonflammable feature and high affinity for CO_2, ILs have been considered to be promising for CO_2 capture [177]. As in a liquid state, however, ILs are not readily to be operated. Synthesized from ILs, polymeric ionic liquids (PILs) are solid-state materials and possess good mechanical strength.

Recently, considerable experimental studies have been reported on the potential application of PILs for CO_2 capture [178-184].

Tang et al. synthesized various vinyl imidazolium-based PILs, such as poly[1-(4-vinylbenzyl)-3-butylimidazolium] (poly[VBI]$^+$) with tetrafluoroborate ([BF$_4$]$^-$) and hexafluorophosphate ([PF$_6$]$^-$) as anions, poly[2-(1-butylimidazolium-3-yl)ethyl methacrylate (poly[BIM]$^+$) with [BF$_4$]$^-$ as anion [185,186]. All these PILs showed CO_2 sorption capacity much higher than the corresponding ILs [185,186]. Specifically, CO_2 sorption capacity in poly[VBI][BF$_4$], poly[VBI][PF$_6$] and poly[BIM][BF$_4$] were determined to be 1.7, 2.1 and 1.4 times higher than in non-polymeric counterpart, viz. 1-butyl-3-methyl-imidazolium based [BMIM][BF$_4$]. Furthermore, CO_2 sorption in these PILs was found to be totally reversible and much faster than in ILs [178,185]. Similarly, CO_2 sorption capacity in 1-(p-vinylbenzyl)-3-butyl-imidazolium (poly[VBBI]$^+$) and 1-[2-(methacryloyloxy)ethyl]-3-butyl-imidazolium (poly[MABI]$^+$) with [BF$_4$]$^-$, [PF$_6$]$^-$, o-benzoicsulphimide ([Sac]$^-$) and [TF$_2$N]$^-$ were measured to be in the range of 1.7 - 3.1 mol% and higher than in [BMIM][BF$_4$] (1.34 mol%).

In addition, Tang et al. also synthesized ammonium-based PILs including poly[(*p*-vinylbenzyl)trimethylammonium] (poly[VBTMA]) with different anions ([BF$_4$]$^-$, [PF$_6$]$^-$, [Sac]$^-$ and [TF$_2$N]$^-$). These PILs exhibited CO_2 sorption capacity higher than imidazolium-based PILs [180]. Supasitmongkol and Styring measured CO_2 solubility in poly[VBTMA][PF$_6$], which was found to be higher in imidazolium- and pyridinium-based ILs. Particularly, poly[VBTMA][PF$_6$] adsorbed 77 wt% CO_2 [183]. Meanwhile, adsorbed CO_2 could be readily desorbed from poly[VBTMA][PF$_6$]. Blasig et al. measured CO_2 solubility in poly[VBTMA][BF$_4$] up to 180 bar at 348 K

[184]. The results showed that CO_2 sorption capacity in ammonium-based PILs is higher than in imidazolium-based counterparts.

Besides CO_2 sorption, gas separation in PILs has been also experimentally investigated, especially for flue gas separation (CO_2/N_2). Bara and co-workers conducted systematic studies on gas separation in PILs [187-199]. Styrene- and acrylate-based PILs with varying *n*-alkyl substituents were synthesized and gas permeation of CO_2, N_2 and CH_4 was measured [187]. The length of polycation side chain was found to have a large impact on gas diffusivity. It was revealed that these 'first generation' PILs would be superior to traditional polymer membranes. Furthermore, they modified PILs by oligo(ethylene glycol) or nitrile-terminated alkyl polar substituents and observed excellent CO_2/N_2 separation, exceeding the Robeson upper bound of 1991 [188]. They also showed PILs grafted with polyethylene glycol were less brittle and performed well in CO_2/N_2 separation [189].

Despite high selectivity for CO_2 capture, PILs generally have low permeability. For example, CO_2 permeability ranges from 4 to 32 barrer, and N_2 and CH_4 permeability is even smaller (< 3 barrer) [188]. To improve permeability, PIL/IL composite membranes have been developed [190-192]. Bara et al. found CO_2 permeability increased by adding 20 mol% ILs into PILs, in addition to 33% enhancement of CO_2/N_2 selectivity [191]. Carlisle et al. also demonstrated PILs with free ILs could enhance CO_2 permeability and selectivity [192]. Chung and co-workers prepared imidazolium-based PIL/IL composite membranes, which exhibited good selectivity and high CO_2 permeability varying from 100 - 559.5 barrer [190]. Furthermore, they found the end groups of polycation side chain had a large impact on gas diffusivity; specifically, CO_2 diffusivity increased about 170 times upon changing from ethyl group to hepty group [193]. Hudiono et al. induced SAPO-34 zeolite into PIL/IL to

form PIL/IL/zeolite MMMs and the increase in both CO_2 permeability and CO_2/CH_4 selectivity was observed [194]. The authors proposed that liquid ILs acted as wetting agent and thus improved the adhesion between PIL and SAPO-34 zeolite.

It has been recognized that anions rather than cations dominate CO_2 solubility in ILs [195]. For the time being, however, the effects of anions and/or cations for CO_2 capture in PILs are ambiguous. Tang et al. found that cations play a more important role in tuning CO_2 sorption capacity in PILs [178] and similar trend was also observed by Samadi and co-workers [196]. Moreover, the influence of anions was found to be very subtle on the selectivity of CO_2/N_2 and CO_2/CH_4 [197]. Nevertheless, Bhavsar et al. observed anions could have a large effect. Specifically, PILs with carboxylate anions particularly $[CH_3COO]^-$ exhibited unprecedented higher CO_2 sorption capacity and CO_2/N_2 selectivity than other anions [198].

To the best of our knowledge, there is no any simulation study reported for gas in PILs. In this thesis, the first simulation study is performed for CO_2 capture in four PILs with a common cation and different anions. Microscopic insights into the role of cation and anion will be provided.

CHAPTER 3 SIMULATION METHODOLOGY

3.1 Interaction Potentials

For a physical system of interest, the interaction potential includes two terms

$$U_p = U_{bonded} + U_{non-bonded} \tag{3-1}$$

where U_{bonded} is intramolecular potential and $U_{non-bonded}$ is intermolecular potential. U_{bonded} usually consists of three contributions

$$U_{bonded} = U_b + U_\theta + U_\phi \tag{3-2}$$

where U_b is bond-stretching potential between two connected atoms, U_θ is bond-bending potential among three successive atoms, and U_ϕ is torsional potential from four successive atoms.

$U_{non-bonded}$ can be decomposed into U_{VDW} and U_Q

$$U_{non-bonded} = U_{VDW} + U_Q \tag{3-3}$$

where U_{VDW} is van der Waals potential and U_Q is Coulombic potential.

In this thesis, U_{VDW} is described by the 9-6 potential [199]

$$U_{VDW} = \sum_{i,j} \varepsilon_{ij} \left[2 \left(\frac{\sigma_{ij}}{r_{ij}} \right)^9 - 3 \left(\frac{\sigma_{ij}}{r_{ij}} \right)^6 \right] \tag{3-4}$$

where r_{ij} is the distance between atoms i and j, ε_{ij} and σ_{ij} are well depth and collision diameter estimated by the Lorentz-Berthelot combining rules

$$\varepsilon_{ij} = \sqrt{\varepsilon_i \varepsilon_j} \tag{3-5}$$

$$\sigma_{ij} = (\sigma_i + \sigma_j)/2 \tag{3-6}$$

The Coulombic potential U_Q is

$$U_Q = \frac{1}{4\pi\varepsilon_0} \sum_{i,j} \frac{q_i q_j}{r_{ij}}$$

(3-7)

where ε_0 is the permittivity of vacuum and q_i the atomic charge of atom i.

3.2 Force Fields

A force field consists of a set of potential functions and numerical parameters to describe interaction potential. In the past, a number of force fields have been developed for a variety of systems. For example, Molecular Mechanics (MM) force field is suitable for organic compounds, free radicals, and ions [200]; Assisted Model Building with Energy Refinement (AMBER) force field performs well for proteins, nucleic acids, and polysaccharides [201]; Chemistry at HARvard Macromolecular Mechanics (CHARMM) force field is for organics, solutions, polymers and biomolecules [202]; Consistent Valence force field (CVFF) is largely for amino acids, water, proteins, peptides, organics, etc [203].

The force fields listed above are considered as the first-generation due to their simple mathematical form. To calculate complex properties such as molecular structures, spectra, and conformations, the second-generation force fields have been developed in which the parameters were obtained by combining quantum mechanical calculations with experimental data. The second-generation force fields include CFF91 (Consistent Force Field 91, for hydrocarbons, proteins, and permanent gases), PCFF (Polymer Consistent Force Field, for polymers, polycarbonates, polysaccharides, inorganic metals, and zeolites) [204], MMFF93 (Merck Molecular Force Field 93, for receptor-ligand involving nucleic acids and proteins), and COMPASS (Condensed-phase Optimized Molecular Potentials for Atomistic

Simulation Studies, for polymers, organic, and inorganic materials) [205]. PCFF and COMPASS have the same functional form and belong to the family of CFF. Specifically, PCFF was developed on the basis of CFF91 and has been applied to polymers and organic materials. Based on PCFF, COMPASS is the first *ab initio* force field. COMPASS enables accurate predictions for a wide range of molecules in both isolated and condensed phases. In this thesis, both PCFF and COMPASS are used to investigate gas permeation and separation in polymer membranes.

3.3 Monte Carlo Simulation

Monte Carlo (MC) simulation is a stochastic method based on statistical mechanics to generate representative configurations [256,257]. A set of statistical ensembles can be produced during MC simulation, for example, canonical (*NVT*, in which the number of particles, volume, and temperature are constant), microcanonical (*NVE*, in which number of particles, volume, energy are constant), isobaric-isothermal (*NPT*, in which number of particles, pressure, temperature are constant), grand-canonical (*μVT*, in which the chemical potential, volume and temperature are constant), etc.

Because only interaction energies rather than forces are evaluated, MC simulation is very efficient in configurational sampling. Furthermore, MC simulation can be performed with physically unnatural trial moves. Depending on the system of interest, various types of trial moves can be attempted such as translation, rotation, displacement, regrowth, etc. A trial move is accepted or rejected based on a criterion proposed by Metropolis [206]

$$P_{acc}(o \rightarrow n) = \min\left(1, \exp\left\{-\left[U(n) - U(o)\right]/k_{\mathrm{B}}T\right\}\right) \tag{3-8}$$

where k_B is Boltzmann's constant, U is potential energy, '*n*' and '*o*' refer to new and old states, respectively. After the trial move, a pseudorandom number is generated

within (0, 1). If this random number is less than $P_{acc}(o \to n)$, then the trial move is accepted. After a sufficiently large number of trials moves, system properties can be ensemble averaged.

3.4 Molecular Dynamics Simulation

Molecular dynamics (MD) simulation mimics the natural pathway of motion. In contrast to MC simulation, the configurations generated in MD are successive. Consider a system of N particles, the force $\vec{F}_i$ on particle i is the gradient of potential energy U_p

$$\vec{F}_i = -\nabla_i U_p = -(\vec{i}\frac{\partial}{\partial x_i} + \vec{j}\frac{\partial}{\partial y_i} + \vec{k}\frac{\partial}{\partial z_i})U_p \tag{3-9}$$

The acceleration is calculated from the Newton's second law of motion

$$\vec{a}_i = \frac{\vec{F}_i}{m_i} \tag{3-10}$$

By integrating (3-10), the velocity and position of atom i can be predicted

$$\vec{v}_i = \vec{v}_i^0 + \vec{a}_i \Delta t \tag{3-11}$$

$$\vec{r}_i = \vec{r}_i^0 + \vec{v}_i^0 \Delta t + \frac{1}{2}\vec{a}_i \Delta t^2 \tag{3-12}$$

where $\vec{v}_i$ is the velocity, $\vec{r}_i$ the position, and '0' denotes the initial values.

The commonly used integration method is Velocity Verlet Algorithm (VVA), which is a derivative of Verlet algorithm. To predict the position, velocity, and force at $(t + \Delta t)$, the VVA algorithm includes three steps. Firstly, the velocity at $(t + \frac{1}{2}\Delta t)$ is estimated by

$$\vec{v}(t) + \frac{1}{2}\Delta t\frac{\vec{f}(t)}{m} \to \vec{v}(t + \frac{1}{2}\Delta t) \tag{3-13}$$

Secondly, the position $\vec{r}(t+\Delta t)$ is calculated from

$$\vec{r}(t)+\Delta t\ \vec{v}(t+\frac{1}{2}\Delta t) \rightarrow \vec{r}(t+\Delta t) \tag{3-14}$$

With this new position, the force $\vec{f}(t+\Delta t)$ can be evaluated. Finally, the velocity $\vec{v}(t+\Delta t)$ is derived from

$$\vec{v}(t+\frac{1}{2}\Delta t)+\frac{1}{2}\Delta t\ \frac{\vec{f}(t+\Delta t)}{m} \rightarrow \vec{v}(t+\Delta t) \tag{3-15}$$

Through the three-step calculations, the position $\vec{r}(t+\Delta t)$, velocity $\vec{v}(t+\Delta t)$, and force $\vec{f}(t+\Delta t)$ can be predicted. The time step Δt is chosen to ensure the total energy is conserved. The average properties can be determined from simulation trajectory.

3.5 Technical Issues

In this Section, a few technical issues used to analyze membrane structure and gas properties are briefly described.

3.5.1 Free Volume and Void Size Distribution

Polymer membranes are usually characterized by fractional free volume (FFV) and void size distribution (VSD). In this thesis, FFVs and VSDs are estimated from a geometrical point of view by MC simulation using an in-house developed code. A probe is randomly inserted into simulation box and the insertion is considered to be successful if the probe does not overlap with any polymer atom. The ratio of successful insertion to the total number of insertion gives the FFV. VSD is estimated by a method previously used for microporous materials [207,208]. In brief, the simulation box is divided into three-dimensional fine grids with a size of approximately 0.1 Å. The void size at a grid is determined as the diameter of the

maximum cavity that encloses the grid but has no overlap with any polymer atom, as

shown in **Figure 3.1**.
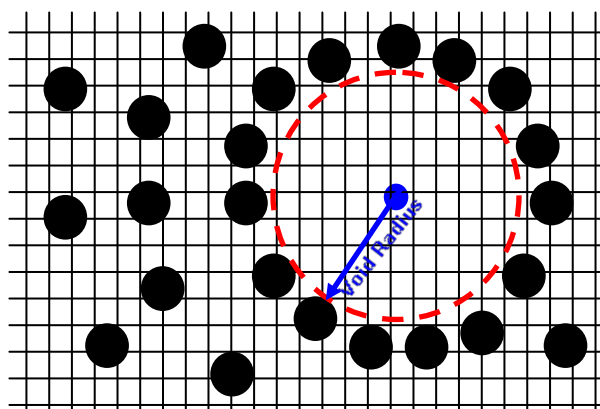
Figure 3.1 Schematic representation of a void. The black dot denotes particles in the simulation system.

3.5.2 Radial Distribution Function

Radial distribution functions or pair correlation function $g(r)$ describes the variation

of particle density as a function of distance relative to average density.

Mathematically, $g(r)$ is defined as

$$g(r) = \frac{\rho(r)}{\rho} \tag{3-16}$$

where $\rho(r)$ is the local density at position r and ρ is the system density.
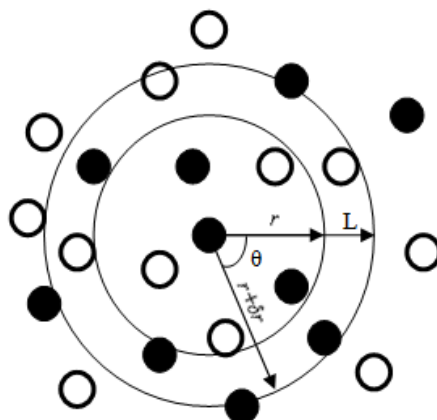
Figure 3.2 Schematic representation of radial distribution function.

In a MC or MD simulation, $g(r)$ can be estimated by

$$g(r) = \frac{dN(r, r + \delta r)}{\rho 4\pi r^2 dr} \tag{3-17}$$

where $dN(r, r + \delta r)$ is the number of particles within an interval $(r, \ r + \delta r)$ as illustrated in **Figure 3.2**.

3.5.3 Mean Squared Displacement

The mobility of particle can be evaluated by mean squared displacement (MSD)

$$\text{MSD}(t) = \frac{1}{N} \sum_{i=1}^{N} \left| \Delta \vec{\mathbf{r}}_i(t) \right|^2 \tag{3-18}$$

where N is the number of particles and $\Delta \vec{\mathbf{r}}_i(t)$ is the displacement of ith ion at time t. MSD is calculated from the ensemble average of MD simulation trajectory. In the calculation, the multiple-origin method is usually used to improve statistical accuracy. For normal (also called Einstein) diffusion, diffusivity can be estimated from MSD by Einstein relationship

$$D = \frac{1}{6} \frac{\text{d}}{\text{d}t} \lim_{t \to \infty} \text{MSD}(t) \tag{3-19}$$

CHAPTER 4 POLYMERS OF INTRINSIC MICROPOROSITY

4.1 Introduction

Polymers of intrinsic microporosity (PIMs) are amorphous, thermally stable, and glassy polymers. Remarkably, they have microporous character and are potentially useful for gas separation, storage, and catalysis. To date only a few studies have been reported on the preparation and modification of PIMs for gas separation. For instance, two PIM (PIM-1 and PIM-7) cast into membranes were found to have high performance in gas separation [162,165], and indeed exceed the trade-off between permeability and selectivity proposed by Robeson [6]. Mixed matrix membranes (MMMs) are a class of novel membranes containing organic polymers (such as polyimides) and inorganic particles (such as zeolite and MOF) to form hybrid membranes. MMMs formed by PIM-1 and silica nanoparticles showed enhancement in gas permeability due to the cavities between organic and inorganic phases [209]. PIM-1 derived membranes with functionalized side groups such as trifluoromethyl, phenylsulfone, and carboxyl outperformed the prototypical PIM-1 membrane in gas separation [52,166,169]. PIM-PI copolymers were found to exceed the Robeson's upper bound and show potential for gas separation [210]. An atomistic packing model was built for PIM-1 and the FFV, VSD, and gas transport properties in the model membrane were examined [173].

A detailed study of PIMs is desired toward the development of next-generation polymer membranes for high-performance gas separation. In this Chapter, the solution, diffusion, and permeation in two PIMs (PIM-1 and PIM-7) are simulated. In Section 4.2, simulation models and methods are introduced, including MC and MD to

calculate solubility and diffusion, respectively. In Section 4.3, the FFVs and VSDs are presented for PIM-1 and PIM-7. The solubility, diffusivity, and permeability of four industrially important gases (H_2, O_2, CO_2 and CH_4) are reported and compared with available experimental data. In addition, the ideal selectivities of CO_2 with respect to H_2, O_2, and CH_4 are evaluated.
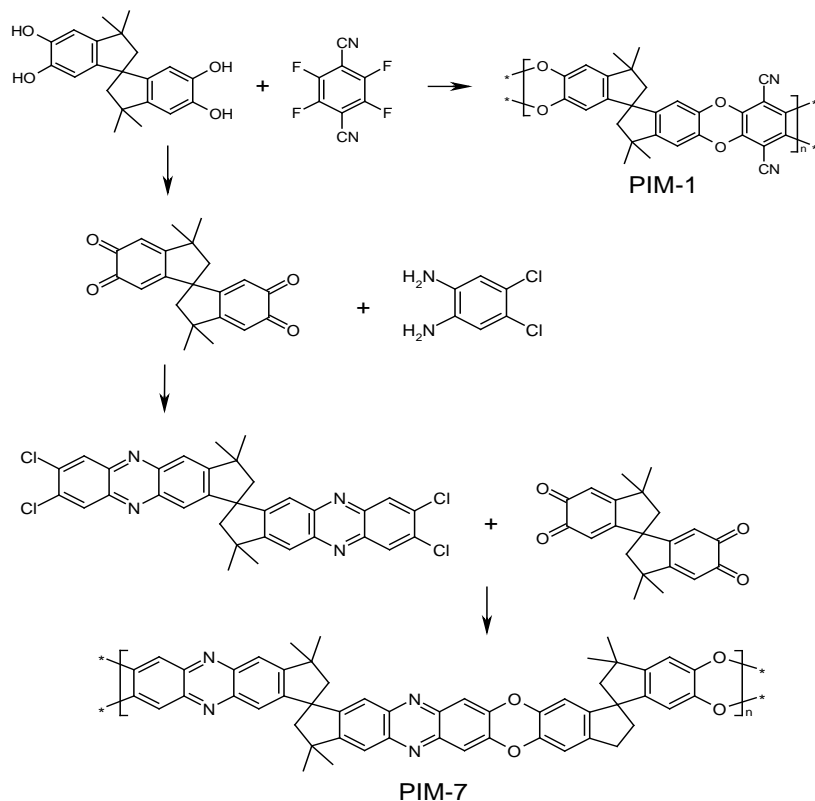
Figure 4.1 Schematic synthesis processes and structures of PIM-1 and PIM-7.

4.2 Models and Methods

4.2.1 Atomistic Models

PIM-1 and PIM-7 were experimentally synthesized from 5,5',6,6'-tetrahydroxy-3,3,3',3'-tetramethyl-1,1'-spirobisindane by polycondensation reaction [147,149,152]. **Figure 4.1** shows the synthesis processes and structures of PIM-1 and PIM-7. The backbones of PIM-1 and PIM-7 contain aromatic rings that are connected by spiro-centers (i.e. tetrahedral carbon atoms shared by two rings). As a consequence, the

atomic packing is not efficient and intrinsic porosity exists in PIM-1 and PIM-7. The primary difference between PIM-1 and PIM-7 is the presence of cyano ($-C \equiv N$) groups in PIM-1. As we shall see below, this causes differences in FFV, solubility and diffusion coefficients in the two PIMs.

To construct the model membranes, the polymer chains of PIM-1 and PIM-7 were terminated by hydrogen atoms. Each polymer chain consisted of a number of repeat units (15 for PIM-1 and 10 for PIM-7) arranged in a random torsional angle. Compared to PIM-1, the number of atoms in the repeat unit of PIM-7 is larger; therefore, a shorter PIM-7 chain was constructed in order to have a comparable number of atoms in the two polymer chains. PIM-1 and PIM-7 membranes were built by the *Amorphous Cell* in Materials Studio 4.3 (Accelrys Inc.) using the scheme of Theodorou and Suter [211]. Each membrane was composed of three polymer chains in a periodic cubic simulation box, with an initial density of 0.1 g/cm^3 and a target density of 1.0 g/cm^3. Ten configurations were generated and three of them were selected for equilibration by the following procedure: (1) energy minimization at zero Kelvin with 5 million steps; (2) 500 ps NVT-MD simulation at 600 K; (3) 500 ps NPT-MD simulation at 600 K at 1 bar; (4) annealing at 1 bar from 600 K to 300 K with a temperature interval 50 K. (5) 100 ps NPT-MD simulation at 10 bar with a time step of 0.1 fs. (6) 2000 ps NPT-MD simulation at 300 K and 1 bar with a time step of 1 fs.

The energy minimization and MD simulations were conducted in DL_POLY [212,213]. To do so, an in-house code was developed to convert the structure files created by Materials Studio to DL_POLY. In such a way, the computational time was reduced by one to two orders of magnitude. The polymers were mimicked by the

PCFF [214-217] with bonded and non-bonded terms. The bonded term U_{bonded}

consists of

$$
\begin{aligned}
U_{\text{bonded}} = &\sum_b \left[k_2^b (b-b_0)^2 + k_3^b (b-b_0)^3 + k_4^b (b-b_0)^4 \right] \\
&+ \sum_\theta \left[k_2^\theta (\theta-\theta_0)^2 + k_3^\theta (\theta-\theta_0)^3 + k_4^\theta (\theta-\theta_0)^4 \right] \\
&+ \sum_\phi \left[k_1^\phi (1-\cos\phi) + k_2^\phi (1-\cos 2\phi) + k_3^\phi (1-\cos 3\phi) \right] \\
&+ \sum_\chi k^\chi (\chi-\chi_0)^2
\end{aligned}
\tag{4-1}
$$

where b, θ, ϕ and χ represent bond length, bond angle, dihedral angle or out-of-plane

angle formed by pairs, triplets and quadruplets, respectively. The non-bonded term

$U_{non-bonded}$ consists of Lennard-Jones (LJ) and Coulombic potentials

$$
U_{non-bonded} = \frac{1}{4\pi\varepsilon_0} \sum_{i,j} \frac{q_i q_j}{r_{ij}} + \sum_{i,j} \varepsilon_{ij} \left[2\left(\frac{r_{ij}^0}{r_{ij}}\right)^9 - 3\left(\frac{r_{ij}^0}{r_{ij}}\right)^6 \right]
\tag{4-2}
$$

where ε_0 is the permittivity of vacuum, q_i the atomic charge on atom i, and r_{ij} is the

distance of between atoms i and j; ε_{ij} and r_{ij}^0 are the well depth and collision diameter

of the LJ potential. The LJ interactions were calculated with a cutoff of 13 Å and the

Coulombic interactions were treated by the Ewald sum with a precision of 10^{-5}. The

VVA algorithm was used in the MD simulation. Temperature and pressure were

controlled by the Berendsen method [218] with a decay constant of 0.6 ps.

The equilibrated models of PIM-1 and PIM-7 membranes were characterized by

solubility parameter, FFV, and VSD. The solubility parameter was evaluated by the

cohesive energy of polymer. The FFV and VSD in a polymer membrane play a

crucial role in gas transport. Experimentally, positron annihilation lifetime

spectroscopy (PALS) is commonly used to determine free volume by measuring the

life time of positronium [219]. In this study, the FFV and VSD were estimated

geometrically by MC simulation using the in-house developed code described in Section 3.5.1.

4.2.2 Sorption and Diffusion

The four gases considered (H_2, O_2, CO_2 and CH_4) were also mimicked by the PCFF [214-217]. At a given pressure p, the solubility c of a gas is governed by the solubility coefficient $S(c, p)$

$$c = S(c, p)p \tag{4-3}$$

In this study, the solubility coefficient was evaluated at infinite dilution and hence $S(c, p)$ was equal to the Henry's constant K_H. From statistical mechanics, it is easy to derive

$$K_H = \beta \exp\left(-\beta \mu_{ex}\right) \tag{4-4}$$

where $\beta = 1/k_B T$ is the reciprocal temperature and μ_{ex} is the excess chemical potential at infinite dilution. From the Widom insertion method [220], equation (4-4) becomes

$$K_H = \langle \beta \int \exp[-\beta u_a(\mathbf{r}, \varpi)] \, d\mathbf{r} d\varpi \rangle \tag{4-5}$$

where $u_a(\mathbf{r}, \varpi)$ is the interaction energy between membrane and a single gas molecule at position $\mathbf{r}$ and orientation ϖ.

Diffusion in PIM-1 and PIM-7 was simulated by MD method. Three gas molecules were inserted into the simulation box of the model membrane. At least half of the box length existed between the gas molecules in order to minimize their interactions. In this regard, the diffusion was examined at infinite dilution. MD simulation was performed in NVT ensemble for 12 ns. The first 5 ns was used for equilibration and the remaining 7 ns for analysis. Similar to the MD simulation for the equilibration of

37

polymer membrane, the LJ and Coulombic interactions were also calculated with a cutoff of 13 Å and the Ewald sum. Temperature was controlled by the Berendsen method [218] with a decay constant of 0.6 ps. The mobility of polymer chains and gas molecules were estimated by the mean-squared displacement.

4.3 Results and Discussion

4.3.1 Membrane Characterization

Figure 4.2 shows the typical atomistic models of PIM-1 and PIM-7 membranes after MD equilibration. The backbones of PIM-1 and PIM-7 are rigid due to the considerable amount of aromatic rings; consequently, intramolecular rotation only occurs at the spiro-centers. As discussed below, interconnected voids are formed due to the inefficient packing of the polymer chains.
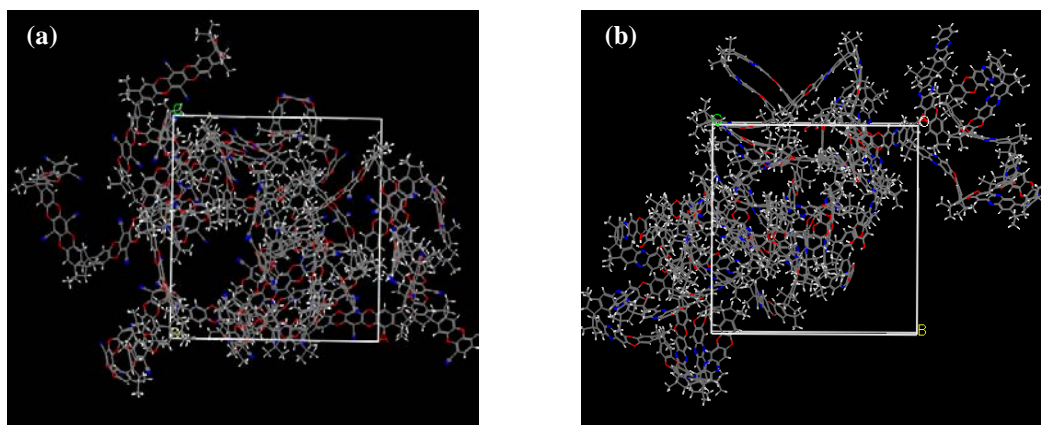
Figure 4.2 Typical atomistic models of (a) PIM-1 and (b) PIM-7. Color code: carbon, grey; nitrogen, blue; oxygen, red; hydrogen, white.

Table 4.1 lists the predicted properties of PIM-1 and PIM-7 model membranes averaged from three independent runs with different initial configurations. The densities of both models are close to the experimentally determined values of PIM-1 ($1.061 \sim 1.092$ g/cm^3) [173] and PIM-7 (1.086 g/cm^3) [221]. The deviations between the predicted and experimental densities are $3 \sim 4\%$. This indicates that the PCFF force field is fairly good in predicting the densities of PIM-1 and PIM-7 membranes.

However, further improvement is desired to achieve a better agreement such as using a more accurate force field. We note that the precise prediction of density for a membrane is critical to accurately describe its sorption, diffusion, and permeation.

Table 4.1 PIM-1 and PIM-7 model membranes.

Membrane	PIM-1	PIM-7
Density [g/cm^3]	1.031 ± 0.004	1.041 ± 0.002
CED [J/cm^3]	218.45 ± 6.81	216.97 ± 5.51
Solubility parameter δ [(J/cm^3)$^{1/2}$]	14.78 ± 0.23	14.73 ± 0.18
Number of atoms	2487	3192
Box length [Å]	32.15	34.96

Solubility parameter is one of the important characteristics of polymer defined as

$$\delta = \sqrt{\frac{E_{coh}}{V}} = \sqrt{\frac{E_{vac} - E_{bulk}}{V}}$$
(4-6)

where E_{coh} is the cohesive energy obtained from the energy difference between the molecule in vacuum (E_{vac}) and in amorphous bulk state (E_{bulk}). V is the molar volume and E_{coh}/V is the cohesive energy density (CED). CED can be interpreted as the energy that keeps polymer molecules staying together. As shown in **Table 4.1**, the CED and δ of PIM-1 and PIM-7 are very close, implying that the interactions of PIM-1 and PIM-7 are similar due to their similar chain structures.

The FFVs in PIM-1 and PIM-7 were calculated by averaging 100 frames and found to be 47.7% and 46.6%, respectively. These FFVs are substantially larger than in common PI membranes (30 ~ 38%) [96]. They are also larger than that in silicalite (37%), but smaller than those in metal-organic frameworks (MOFs) and covalent-organic frameworks (COFs) [222,223]. MOFs and COFs are emerging novel class of hybrid nanoporous materials and have shown high potential in gas storage and separation [224,225]. **Figure 4.3** illustrates the void morphologies in PIM-1 and PIM-

7. The voids are mostly interconnected due to the intrinsic porosity. In other words, there exist continuous voids (holes) in the membranes. This implies that the PIM membranes are zeolite-like from the geometrical point of view. The voids in a membrane vary in size and have different contributions to gas transport. As shown in **Figure 4.4**, both PIM-1 and PIM-7 membranes exhibit a wide range of VSDs with diameter in the range of 0 ~ 9 Å. A comparison between PIM-1 and PIM-7 indicates that PIM-1 has a larger FFV and a slightly higher percentage of voids with diameter > 6.5 Å. This is attributed to the cyano groups in PIM-1, which lead to a steric hindrance and inefficient packing of PIM-1 membrane. The larger voids contribute predominantly to gas diffusion; consequently, as we will see below that the diffusion coefficients in PIM-1 are generally greater than those in PIM-7.
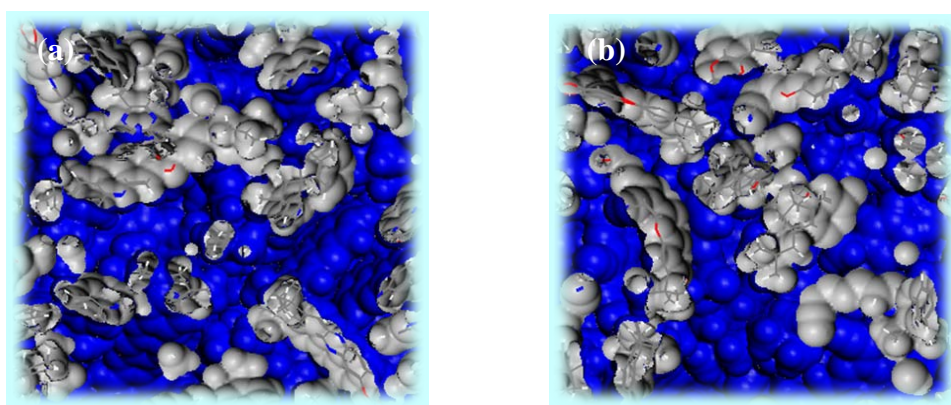
Figure 4.3 Void morphologies in (a) PIM-1 and (b) PIM-7 as denoted by the blue regions. The grey regions are polymer chains.
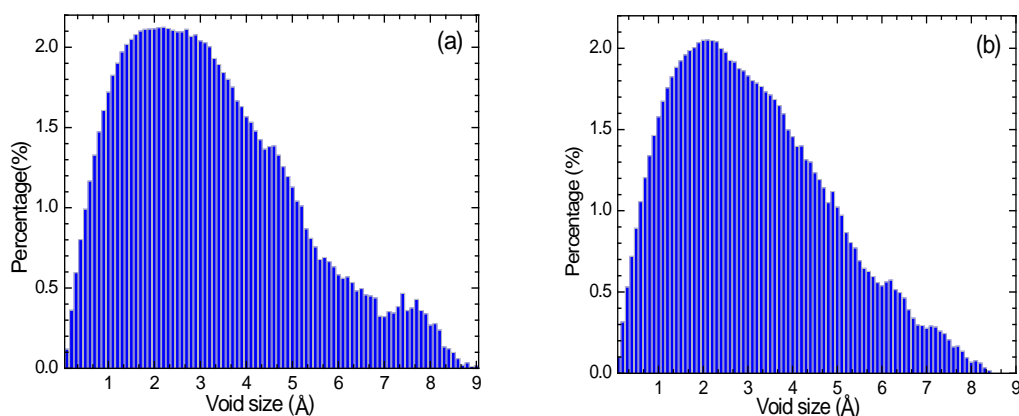
Figure 4.4 Void size distributions in (a) PIM-1 and (b) PIM-7.

The mobility of polymer chains in a membrane plays an important role in gas transport. Upon the motion of polymer chains, the voids in the membrane change their size and shape, which would activate or block gas molecules to transport. **Figure 4.5** shows the MSDs of polymer chains in PIM-1 and PIM-7. As seen, the mobility of polymer chains is very small due to the stiffness of the polymer chains.
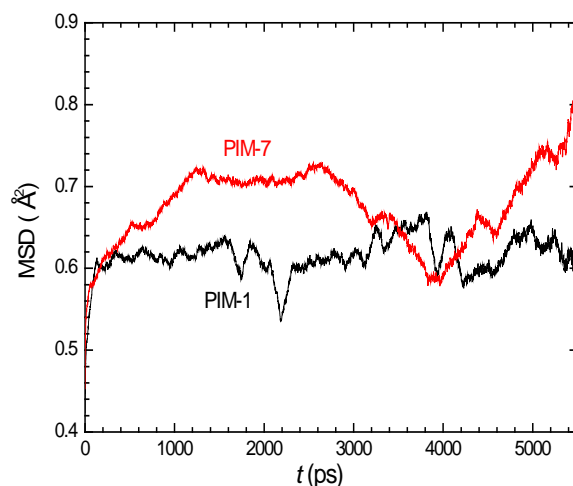
Figure 4.5 Mean-squared displacements of polymer chains in PIM-1 and PIM-7.

Table 4.2 Simulated and experimental solubility coefficients [cm^3 (STP)/cm^3 (polymer) bar] and diffusion coefficients [10^{-8} cm^2/s] in PIM-1 and PIM-7 at 300 K. The experimental pressure was approximately 200 mbar [162].

	Gas	S_{sim}	S_{exp} [162]	D_{sim}	D_{exp} [162]
PIM-1	H_2	0.46 ± 0.03	0.58	6630 ± 215	1700
	O_2	4.1 ± 0.6	3.5	452 ± 81	81
	CO_2	50.7 ± 9.1	66.9	151 ± 47	26
	CH_4	14.2 ± 3.1	13.7	112.0 ± 27.4	6.8
PIM-7	H_2	0.44 ± 0.01	0.61	6860 ± 689	1100
	O_2	4.01 ± 0.26	2.35	346 ± 100	62
	CO_2	50.6 ± 5.7	39.5	130 ± 13	21
	CH_4	15.5 ± 3.1	9.1	60.7 ± 6.6	5.1

4.3.2 Sorption

Table 4.2 lists the solubility coefficients of four gases (H_2, O_2, CO_2, and CH_4) in PIM-1 and PIM-7 at 300 K. The simulated results were the averages of three independent runs with different initial configurations. Fairly good agreement is observed between simulation and experiment for all the four gases. The predicted solubility coefficients here match with experiment better than those evaluated by the coarse-grained TST methods [173]. Compared to all other polymers reported to date, PIM-1 and PIM-7 show the largest solubility coefficients as a consequence of the presence of microporous structure and polar sorption sites [162,165]. This is unique for these glassy PIMs because large solubility is usually observed in rubbery polymers. The solubility coefficients in PIM-1 appear to be slightly larger than in PIM-7 (particularly in experimental data). The reason is PIM-1 contains the cyano groups that enhance the affinity for gas molecules.
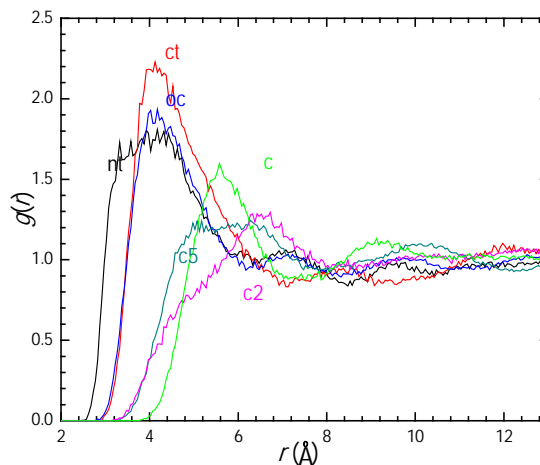
Figure 4.6 Radial distribution functions of CO_2 and atoms in PIM-1.
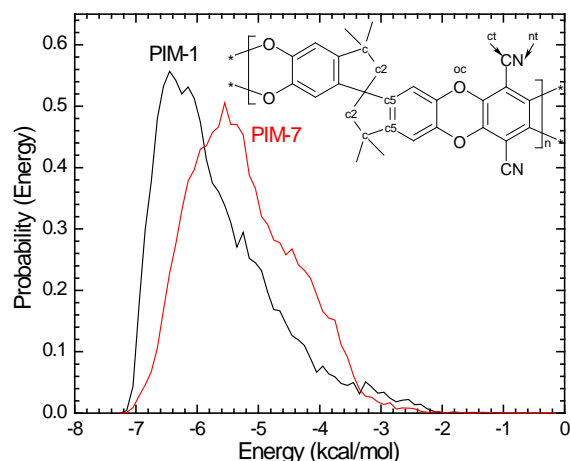
Figure 4.7 Energy distribution of a single CO_2 molecule in PIM-1 and PIM-7.

To further elucidate, the structural and energetic properties were calculated for CO_2 in the membranes. **Figure 4.6** shows the radial distribution functions between CO_2 and atoms in PIM-1. The cyano group (**ct** and **nt** atoms), as well as the oxygen atom (**oc**), have the strongest interactions with CO_2. Consequently, PIM-1 exhibits a larger solubility for CO_2. **Figure 4.7** shows the interaction energy distribution of a single CO_2 molecule in PIM-1 and PIM-7. As can be seen, the energy in PIM-1 is larger (more negative) than in PIM-7, which implies that CO_2 interacts with PIM-1 more strongly than PIM-7 and thus has a larger solubility in PIM-1.

In the two membranes, the solubility coefficients increase in the order of $H_2 < O_2 < CH_4 < CO_2$. This reveals that the membranes have the largest affinity for CO_2 and the least for H_2. It is commonly recognized that the solubility coefficients can be correlated with the critical temperature T_c of sorbate [226],

$$\ln S = \ln S_0 + K_c T_c \tag{4-7}$$

where S_0 and K_c are constants, specifically K_c is independent of the chemical structure of polymer membrane. The critical temperatures of the four gases are given in **Table 4.3**. Fairly good correlations are found in **Figure 4.8** between the calculated

semi-logarithmic solubility coefficients and critical temperatures. We note that T_c is the signature of condensability and a gas with higher T_c has a stronger interaction with the membrane and therefore a larger solubility.

Table 4.3 Critical temperature, kinetic diameters d_k, collision diameters d_c, and effective diameters d_{eff} of H_2, O_2, CO_2, and CH_4. The diameters are in angstrom (Å).

Gas	T_c (K)	d_k [227]	d_c	d_{eff} [228]
H_2	33.2	2.89	2.83	2.85
O_2	154.6	3.46	3.47	3.46
CO_2	304.2	3.30	3.94	3.61
CH_4	190.6	3.80	3.76	3.78
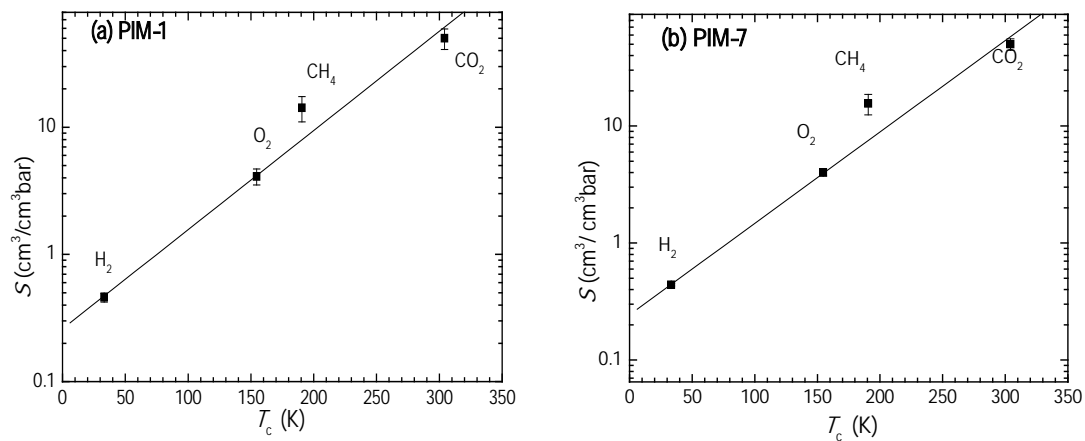
Figure 4.8 Simulated solubility coefficients in (a) PIM-1 and (b) PIM-7 as a function of critical temperature T_c.

4.3.3 Diffusion

The underlying mechanism of gas diffusion in a polymer membrane is regarded as activated process. A molecule is trapped in a void for a certain amount of time and then crosses energy barrier to jump into a neighboring void. The frequency of jumping depends on how large is the energy barrier, which in turn is governed by the specific polymer membrane and gas molecule. This process continues repeatedly as a result of the opening and close of voids in the polymer matrix. **Figure 4.9** shows the

representative displacement of a single gas molecule as a function of time within 8-ns simulation duration in PIM-7. Similar behavior was observed in PIM-1 and thus not shown here. In general, three types of motions are observed in **Figure 4.9** for different gases. The first type is that H_2 molecule is seldom trapped because of its small diameter and frequent jumping. The second type is for O_2 or CO_2 molecule, which is trapped in a void for 2 ~ 4 ns and then jumps to another void. As illustrated for O_2, in the first 4 ns the molecule is trapped and oscillates with a maximum magnitude of 8 ~ 8.5 Å. This is consistent with the largest void in PIM-7 membrane shown in **Figure 4.4**. At the subsequent duration, the molecule jumps to adjacent void. The third type is for CH_4 molecule with trapped as a significant motion. This is because CH_4 is relatively larger in diameter and not readily to jump into another void. As a consequence, H_2 moves the fastest and CH_4 the slowest.
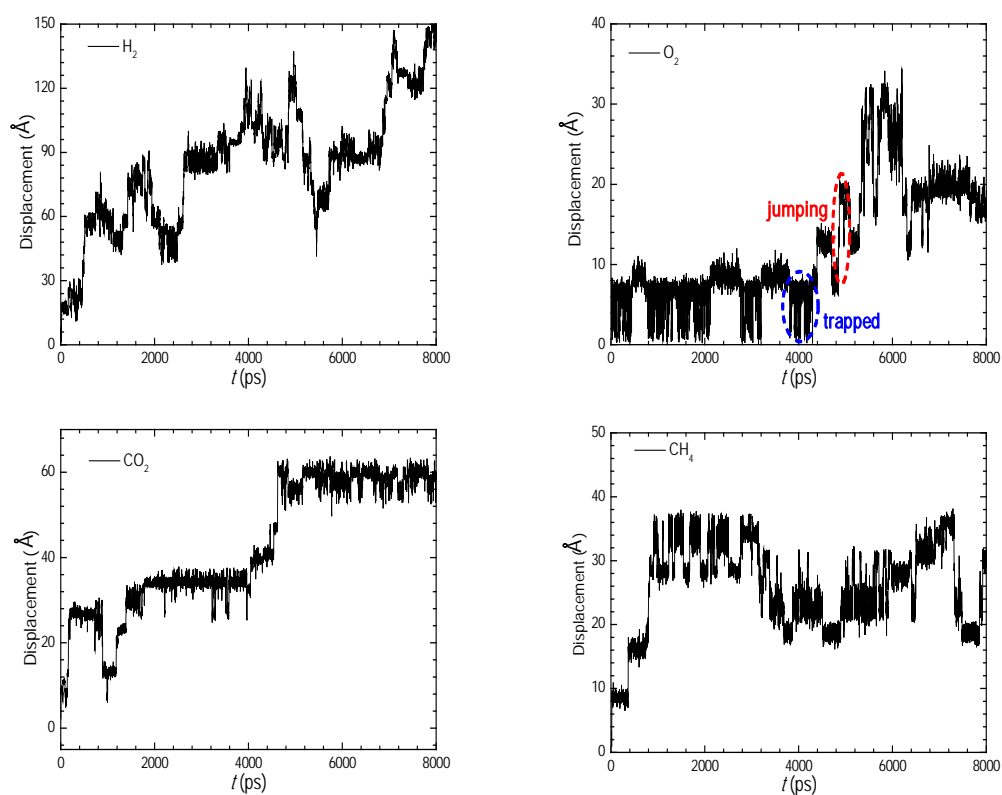
Figure 4.9 Representative displacement of a single gas molecule as a function of time in PIM-7. The trapped and jumping motions are schematically indicated for O_2.

Gas diffusion can be described by MSD versus time t as $\text{MSD}(t) \propto t^{\gamma}$, where scaling index γ is the signature of different types of diffusion. Specifically, $\gamma < 1, > 1$ and $= 1$ correspond to sub-, super- and normal-diffusion, respectively. The sub-diffusion is usually observed within short time and attributed to the structural correlation of immediate environment that retards diffusion. The super-diffusion occurs under convective or hydrodynamic transport. The normal (also called Einstein) diffusion takes place if molecules move randomly. For the four gases in PIM-1 and PIM-7 membranes, normal diffusion was observed at sufficiently long time. Consequently, the diffusion coefficient was estimated using the Einstein relationship

$$D = \frac{1}{6N}\frac{d}{dt}\lim_{t\to\infty}\sum_{k=1}^{N}\left\langle \left| r_k(t) - r_k(0) \right|^2 \right\rangle \tag{4-8}$$

Table 4.2 lists the diffusion coefficients of four gases (H_2, O_2, CO_2, and CH_4) at 300 K. The simulation values were the averages of three independent runs with different initial configurations. The experimental diffusion coefficients in both membranes increase following the order of $CH_4 < CO_2 < O_2 < H_2$, which is well captured by simulation. For a given gas, the diffusion coefficients in PIM-1 are slightly larger than in PIM-7, particularly seen in the experimental data. This is due to the cyano groups in PIM-1, which increase the d-spacing and FFV of PIM-1.

The simulated diffusion coefficients overestimate experimental results by approximately five-fold except for CH_4, which is usually acceptable in the simulation of gas diffusion in polymer membranes. The primary reason for overestimation is the lower densities predicted in the model membranes. As discussed above, the predicted densities are 3 ~ 4% lower than the measured values. Compared to experimental samples, the model membranes are a bit looser and contain a larger degree of free volume. Therefore, gas diffuses faster in the model membranes. After a closer look, it

is found that the deviation between the simulated and experimental diffusion coefficients of CH_4 is larger than other gases. This is because CH_4 has a larger molecule size and the density of membrane exerts a greater impact on its diffusion. In this sense, it is important to construct a model membrane with density matching closely to experimental value. There are many other factors causing the deviation of diffusion coefficients between simulation and experiment. For example, simulation gives self-diffusion coefficient, whereas experiment typically reports transport diffusion coefficient by time-lag measurement. The self- and transport diffusion coefficients are identical only at infinite dilution, but experimental condition is usually at finite pressure/concentration. Accurate prediction of diffusion coefficient requires not only a good force field, but also a well equilibrated polymer model. It was found that the equilibration procedure to construct the model membrane affects gas diffusivity [229]. With 'self-avoiding' random-walk method to build membrane, anisotropy could exist and the polymer chains might distribute non-uniformly. Even if the overall density is close to experimental density, the void distribution in the model membrane mat not be the same as in a real polymer material. Furthermore, polymer chain length also plays an important role in gas diffusion [230]. The model built with short polymer chains has a larger fraction free volume than the model with long polymer chains. Consequently, the diffusion coefficient predicted in the former is greater than in the latter. For PIM-1, the weight-average molar mass was determined experimentally as 370,000 g/mol [165], which means the degree of polymerization of PIM-1 is 797. However, in our simulation, the PIM-1 model had 15 monomers and this would lead to a faster diffusion than measured by experiment. In addition, the short polymer chains have a greater mobility, which in turn facilitates diffusion.
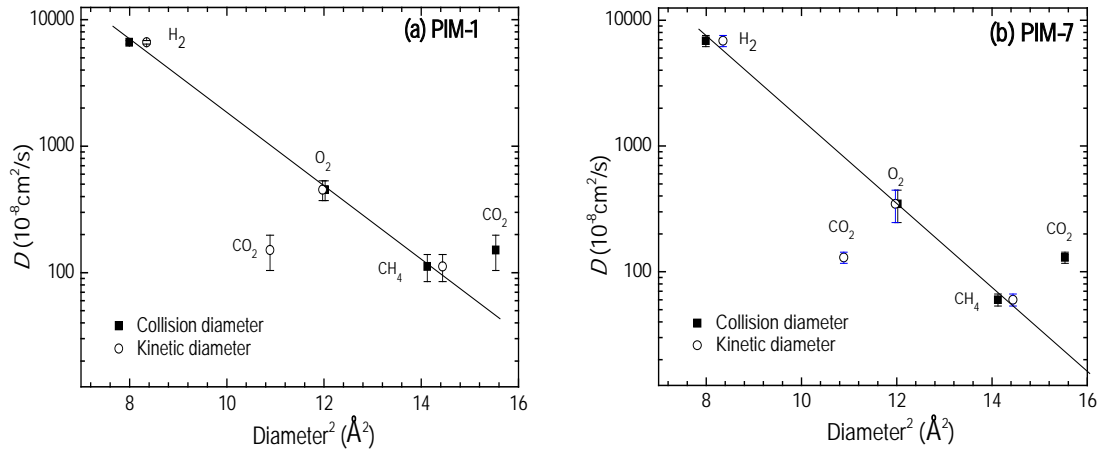
Figure 4.10 Simulated diffusion coefficients in (a) PIM-1 and (b) PIM-7 as a function of squared collision and kinetic diameters.

It is instructive to compare gas diffusion in PIM-1 and PIM-7 with that in other polymers and porous structures. As a result of microporous feature, the two PIMs have diffusion coefficients larger than most glassy polymers, though smaller than extremely permeable PTMSP, poly(4-methyl-2-pentyne) and Teflon AF [162]. In contrast, the diffusion coefficients in the two PIMs are 2 - 3 orders of magnitude lower than in silicalite and MOFs [231-233]. This is because the pores/voids are irregular in amorphous PIMs, but well defined and highly ordered in silicalite and MOFs.
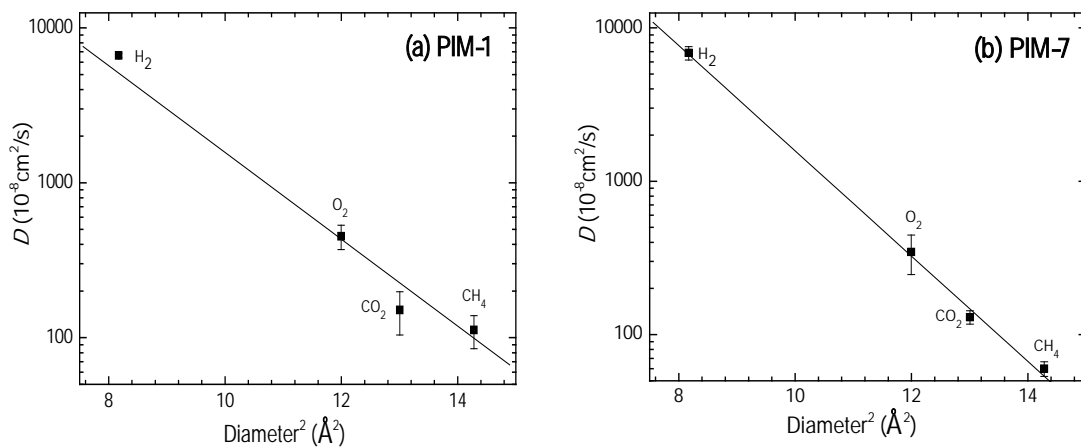
Figure 4.11 Simulated diffusion coefficients in (a) PIM-1 and (b) PIM-7 as a function of squared effective diameter.

Several studies have proposed a correlation between diffusion coefficient and diameter [49,234,235]. For the four gas molecules in this study, **Table 4.3** lists the kinetic diameter d_k related to the molecular sieve dimension, the LJ collision diameter d_c related to the intermolecular separation distance, and the effective diameter $d_{eff} = \sqrt{d_c d_k}$. **Figure 4.10** shows the correlations of the semi-logarithmic diffusion coefficients with d_k and d_c. In general, the correlations are good except CO_2, which is a linear molecule and cannot be described well by either d_k or d_c. To improve the correlations particularly for CO_2, the effective diameter d_{eff} is used instead. As shown in **Figure 4.11**, the correlations are better with the effective diameter for all the four gases in both membranes, which can be described by the Teplyakov-Meares equation [236]

$$\log D = K_1 - K_2 d_{eff}^2 \tag{4-9}$$

where K_1 and K_2 are constants only depending on the intrinsic properties of membranes. With the molecular-based correlations, the diffusion coefficients of other gases can be predicted.

4.3.4 Permeation

Based on the solution-diffusion mechanism, permeability in a polymer membrane can be expressed by $P = S \cdot D$. The separation factor between two species i and j in a membrane is usually evaluated by the ideal permeation selectivity

$$\alpha_{i/j} = \frac{P_i}{P_j} = \frac{S_i}{S_j} \frac{D_i}{D_j} \tag{4-10}$$

where S_i / S_j is the sorption selectivity and D_i / D_j is the diffusion selectivity.

Table 4.4 Sorption, diffusion, and permeation selectivities of CO_2 over H_2, O_2, and CH_4 in PIM-1 and PIM-7 at 300 K.

	Gas	$S_{CO_2} / S_{(i)}$		$D_{CO_2} / D_{(i)}$		$P_{CO_2} / P_{(i)}$	
		Sim.	Exp.	Sim.	Exp.	Sim.	Exp.
PIM-1	H_2	109	117	0.023	0.015	2.51	1.76
	O_2	12.2	19.1	0.33	0.32	4.03	6.11
	CH_4	3.52	4.92	1.35	3.82	4.8	18.8
PIM-7	H_2	115.0	64.8	0.019	0.019	2.15	1.23
	O_2	12.5	16.8	0.37	0.34	4.63	5.71
	CH_4	3.23	4.35	2.17	4.12	7.0	17.9

Table 4.4 gives the sorption, diffusion, and permeation selectivities for CO_2 over H_2, O_2, and CH_4 in PIM-1 and PIM-7 membranes. It should be noted that the separations of CO_2/H_2, CO_2/O_2, and CO_2/CH_4 are practically important for H_2 production, food packaging, and natural gas purification. The simulated sorption selectivities match well with experimental values. The diffusion and permeation selectivities are also close to experimental values except CO_2/CH_4. The reason, as mentioned earlier, is that the simulated diffusion coefficient of CH_4 is larger than experimental result. CO_2 is more permeable in PIM-1 and PIM-7 compared to the other three gases and the sorption selectivity dominates the overall permeation selectivity. As demonstrated experimentally, PIM-1 and PIM-7 exhibit not only high solubility and diffusion coefficients, but high selectivity; and surpass the Robeson's upper bound [162].

4.4 Conclusions

The permeation of four gases (H_2, O_2, CH_4, and CO_2) in PIM-1 and PIM-7 membranes has been examined by simulation. The PIMs have rigid contorted structures with FFV of 47.7% and 46.6%, substantially larger than in common glassy

PIs. A wide range of interconnected voids exist in the membranes with diameter up to 9 Å. The predicted densities are close to experimentally determined data. Compared to PIM-7, PIM-1 possesses a lower density and a larger FFV due to in the presence of cyano groups. The two PIMs have the largest affinity for CO_2 and the least for H_2. The solubility coefficients of the four gases increase following $H_2 < O_2 < CH_4 < CO_2$. Good agreement was observed between simulation and experiment. As a consequence of microporous structure and polar sites, the solubility coefficients in PIM-1 and PIM-7 are substantially higher than in other polymers. The solubility coefficients correlate well with the critical temperatures of gases. The cyano groups in PIM-1 enhance the affinity for gas, and PIM-1 thus exhibits a larger solubility coefficient than PIM-7.

In the two PIMs, the diffusion coefficients increase following $CH_4 < CO_2 < O_2 < H_2$. The simulated diffusion coefficients overestimate experimental values, as the model membranes have 3 - 4% lower densities compared to real samples. Therefore, improved models are desirable to achieve better predictions. Because of the microporous nature, the two PIMs show larger diffusion coefficients than do most glassy polymers. The diffusion coefficients correlate well with the effective diameters of gases. PIM-1 is more diffusive than PIM-7 as the former has larger d-spacing and fractional free volume. The simulated sorption, diffusion, and permeation selectivities generally match well with experimental data. The overall permeation selectivities of three gas pairs CO_2/H_2, CO_2/O_2, and CO_2/CH_4 are dominated by the sorption selectivities. Both PIM-1 and PIM-7 membranes show high permeabilities and selectivities. With the intrinsic porosity and microporous character, the PIMs are attractive for gas separation.

CHAPTER 5 FUNCTIONALIZED POLYMERS OF INTRINSIC MICROPOROSITY

5.1 Introduction

A desired polymer membrane for gas separation should have large permeability, high selectivity, good mechanical and thermal stability. Toward this end, extensive studies have been conducted on various polymers such as PIs [237-240], PSfs [113,241] and PCs [242-244]. In particular, functionalized membranes have been examined on their separation performance. For example, Kim et al. prepared two PIs with different chemical structures (PMDA-ODA and 6FDA-ODA) and found the reduced number of $-O-$ linkages and the presence of mobility-restricted $-C(CF_3)_2-$ groups enhanced permeability (He, CO_2, O_2, N_2 and CH_4) and selectivity (x/CH_4, x = CO_2, O_2, N_2) [245]. The enhancement was attributed to the simultaneous inhibition of intra-segmental mobility by introducing $-C(CF_3)_2-$ and inter-segmental packing by reducing $-O-$ linkage number. Likewise, Stern et al. suggested a similar scenario to synthesize glassy polymer membranes (e.g. PIs) based on the fact that bulky functional groups can act as inter-chain spacer without significantly reducing free volume [246]. As such, polymer chains maintain stiffness and are loosely packed, thus behave as molecular sieve with high performance. In a series PMDA-, BPDA- and 6FDA-based PI membranes, Calle et al. found 6FDA-PIs with *tert*-butyl groups at *ortho-* positions in the central rings of backbones exhibited high permeability and selectivity [247]. Sridhar et al. prepared PPO membranes for CO_2/CH_4 separation and they observed a higher selectivity in sulfonated PPO, but a larger permeability in unmodified polyphenylene oxide [248]. Sen and Banerjee introduced $-C(CF_3)_2-$ groups into polyetherimide (PEI) and the fluorinated PEI membrane had

an exceptionally larger permeability and a higher CO_2/CH_4 selectivity than the unmodified counterpart [249]. All these experimental studies reveal that the functional groups in polymer membranes play a pivotal role in separation performance.

Recently, Du et al. prepared PIM membranes functionalized by trifluoromethyl, phenylsulfone [52] and carboxyl group [169]. From experimental permeabilities, they observed higher permselectivities in the functionalized PIMs for CO_2/N_2 and other gas mixtures. However, the solubility and diffusion coefficients were not measured and it remains elusive whether the enhanced permselectivity is governed by sorption or diffusion selectivity.

In this Chapter, we combine molecular simulation and *ab initio* calculation to investigate the permeation and separation of CO_2/N_2 in PIM membranes with different functional groups (cyano, carboxyl, trifluoromethyl and phenylsulfone). The objective is to provide microscopic insight into the effects of functional groups on membrane performance. Particularly, we attempt to identify the dominant factor, between sorption and diffusion selectivity, which governs permselectivity in the functionalized PIMs. This information is crucial for further improvement on permselectivity and facilitates the design of new membranes for gas separation. In Section 5.2, the models and methods are described, including a robust protocol to construct model membranes, MC and MD simulation to examine solubility and diffusion, and *ab initio* calculation to estimate binding energies between CO_2 and functional groups. In Section 5.3, the model membranes are characterized in terms of FFV, VSD and wide angle X-ray diffraction; the relationship between binding energy and solubility is discussed; the simulated solubility and diffusion coefficients of CO_2

and N_2 are presented and compared with available experimental data; in addition, the permeabilities and selectivities are examined in terms of different functional groups.

5.2 Models and Methods

5.2.1 Atomistic Models

PIM-1   **TFMPS-PIM**   **CX-PIM**
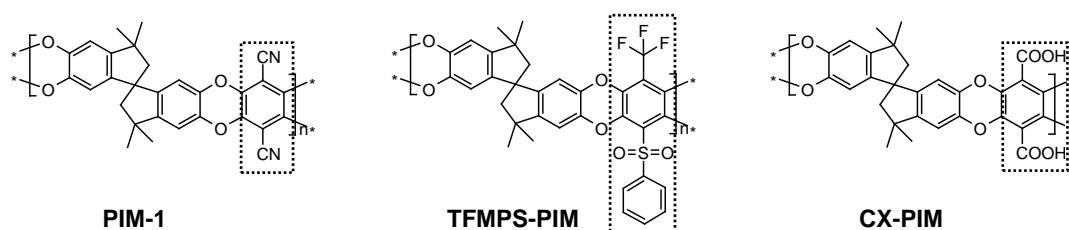
Figure 5.1 Structures of PIM-1, TFMPS-PIM and CX-PIM. The fragmental structures within dotted lines were saturated with hydrogen atoms and then used to calculate the binding energies with CO_2.

Figure 5.1 illustrates three PIM membranes considered here including PIM-1 with cyano, TFMPS-PIM with both trifluoromethyl and phenylsulfone, and CX-PIM with carboxyl. They share the same backbone but differ in functional groups. The atomistic models of the membranes were constructed by the *Amorphous Cell* module in Materials Studio 4.3 (Accelrys Inc., San Diego, CA, USA) using Theodorou and Suter's scheme [211,250]. Each model membrane was composed of three polymer chains in a cubic simulation box with an initial density of 0.1 g/cm^3. The target densities for PIM-1, TFMPS-PIM and CX-PIM were 1.06 g/cm^3, 1.214 g/cm^3, and 1.237 g/cm^3, respectively. Each polymer chain consisted of 15 repeat units arranged in a random torsional angle. To prevent ring catenation during model construction, 200 CH_4 molecules were inserted into the simulation box and removed afterwards. Fifty configurations were generated and three lowest-energy configurations were selected for equilibration by the following procedure: (1) 5×10^6 steps of energy minimization at 0 K. (2) 300 ps NVT-MD simulation at 300 K. (3) 300 ps NVT-MD simulation at 800 K. (4) Repeat step 2 and 3 ten times. (5) 2000 ps NPT-MD

simulation at 300 K and 1 bar. Through extensive tests, this equilibration protocol was found highly efficient to equilibrate model membranes. As presented below, the predicted densities match very closely with experimental data.

Similar to Chapter 4, energy minimization and MD simulation were conducted with DL_POLY 2.20 by converting Materials Studio files into DL_POLY using our in-house code. The Lennard-Jones interactions were calculated with a cutoff of 13 Å and the Coulombic interactions were treated by the Ewald summation with a precision of 10^{-5}. The VVA algorithm was used in MD simulation. Temperature and pressure were controlled by the Berendsen method with a decay constant of 0.6 ps.

The equilibrated model membranes were characterized by FFV, VSD and wide angle X-ray diffraction (WAXD). The former two quantities play an important role in governing gas permeation in polymer membranes, and they were estimated using the method described in Section 3.5.1. The probe size used here was set to be zero, that is, the maximum FFV was estimated. The WAXD was generated by the *Forcite* module in Materials Studio.

5.2.2 Ab Initio Calculations

To quantify how functional groups interact with gas species, the fragmental structures in the dotted lines of **Figure 5.1** were saturated by hydrogen atoms and then used to calculate the binding energies with CO_2. For each group, the second-order Møller-Plesset (MP2) method and 6-31++G** basis set were used to optimize the energetically minimal position of CO_2 near the group. Thereafter, the binding energy was calculated by the MP2 method and a larger basis set namely 6-311++G**. The basis set superposition errors were corrected by the counterpoise method. The *ab initio* calculations were carried out using Gaussian 09 program [251].

5.2.3 Sorption and Diffusion

The solubility coefficients of CO_2 and N_2 were evaluated at 300 K and infinite dilution. The reason is that the effects of functional groups at infinite dilution are the most distinct, particularly on solubility. Consistent with the force field used for polymer chains, CO_2 and N_2 were also mimicked by the PCFF. Gas solubilities are estimated by the Widom insertion method described in Section 4.2.2.

The diffusion of CO_2 and N_2 was simulated by MD method. For each species, three gas molecules were inserted into the simulation box. At least half of the box length existed between the gas molecules in order to minimize their interactions. MD simulation was performed in NVT ensemble for 20 ns. The first 2 ns was used for equilibration and the remaining 18 ns for production. Similar to the MD simulation for model construction, the LJ and Coulombic interactions were also calculated with a cutoff of 13 Å and the Ewald summation with a precision of 10^{-5}. Temperature was at 300 K and controlled by the Berendsen method with a decay constant of 0.6 ps. The mobility of gas species was estimated by the MSD.

5.3 Results and Discussion

5.3.1 Membrane Characterization

Table 5.1 lists the densities of PIM-1, TFMPS-PIM and CX-PIM membranes from simulation and experiment. The densities increase in the order of PIM-1 < TFMPS-PIM < CX-PIM. Good agreement is found between simulated and experimental densities, with only 0.5% deviations. This implies that the model membranes were well equilibrated and the PCFF force field is suitable for the PIMs. As shown in Chapter 4, the deviation between simulated and experimental densities of PIM-1 was about 3%. With the new equilibration protocol, however, the deviation is largely reduced. To construct well-equilibrated model membranes, several factors should be

considered. Firstly, equilibration time should be sufficiently long. Secondly, quenching turns out to be more effective than annealing. Temperature in quenching drops rapidly, while temperature change in annealing is moderate. Thirdly, quenching with a large temperature drop reaches equilibration faster. A sharp temperature drop facilitates polymer chains to cross energy barrier and reach an energetically favorable state. Overall, the new protocol appears to be highly effective to construct reliable model membranes.

Table 5.1 Simulated and experimental densities of PIM-1, TFMPS-PIM and CX-PIM membranes.

Membrane	PIM-1	TFMPS-PIM	CX-PIM
Sim. density (g/cm^3)	1.069 ± 0.026	1.208 ± 0.002	1.236 ± 0.004
Exp. density (g/cm^3)	1.06 ~ 1.09 [173]	1.214 [52]	1.237 [169]
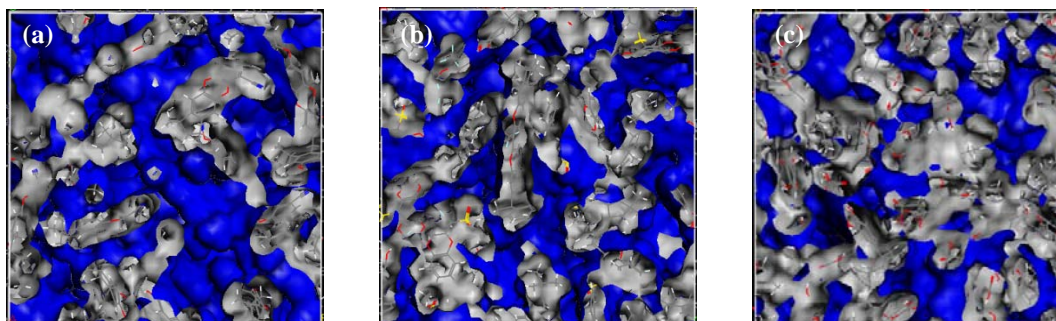
Figure 5.2 Void morphologies in (a) PIM-1, (b) TFMPS-PIM and (c) CX-PIM as denoted by the blue regions. The grey regions are polymer networks.

The voids in a polymer membrane govern the microscopic properties of gas molecules. **Figure 5.2** illustrates the void morphologies in PIM-1, TFMPS-PIM and CX-PIM. There exist substantial interconnected voids in PIM-1, implying PIM-1 is zeolite-like from the geometrical point of view. Upon comparison, the voids are less interconnected in the other two membranes, especially CX-PIM.
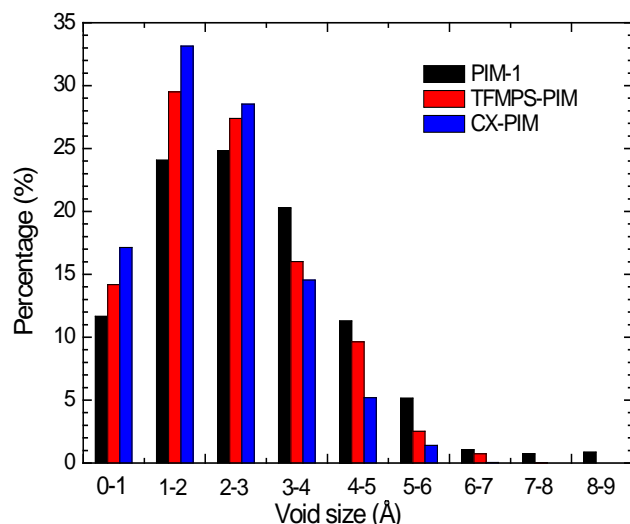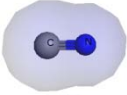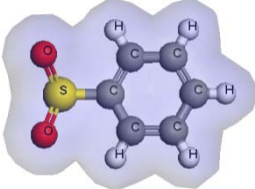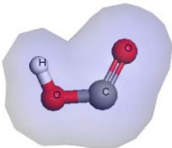
Figure 5.3 Void size distributions in PIM-1, TFMPS-PIM and CX-PIM.

Figure 5.3 further shows the void size distributions (VSDs) in the three membranes. The percentage of large voids (> 3 Å) decreases in the order of PIM-1 > TFMPS-PIM > CX-PIM. Specifically, the largest void size is 9 Å in PIM-1, 7 Å in TFMPS-PIM and 6 Å in CX-PIM. The kinetic diameters of CO_2 and N_2 are 3.30 and 3.64 Å, respectively, and thus the large voids (> 3 Å) contribute predominantly to gas diffusion. Consequently, we will see below that the diffusion coefficients in PIM-1 are greater than in TFMPS-PIM and CX-PIM. On the other hand, there are more small voids in TFMPS-PIM and CX-PIM than in PIM-1. The percentage of small voids (0 – 3 Å) increases as PIM-1 < TFMPS-PIM < CX-PIM. The reason is that polymer chains in PIM-1 are not efficiently packed due to the presence of rigid spiro carbons and large voids are formed. With bulky trifluoromethyl and phenylsulfone in TFMPS-PIM, the large voids are partially occupied and thus become smaller. As seen in **Table 5.2**, trifluoromethyl and phenylsulfone, particularly the latter, have a larger van der Waals volume than cyano. However, this argument is not applicable to CX-PIM as carboxyl only has a slightly larger volume compared with cyano. Instead, hydrogen bonds are speculated to form in CX-PIM.

Table 5.2 Schematic structures and van der Waals volumes of functional groups, and binding energies between CO_2 and functional groups.

Functional Group	Structure	van der Waals Volume (Å^3)	Binding Energy (kJ/mol)
Cyano		26.39	−8.96
Trifluoromethyl		41.82	−5.88
Phenylsulfone		122.26	−12.52
Carboxyl		36.45	−13.29
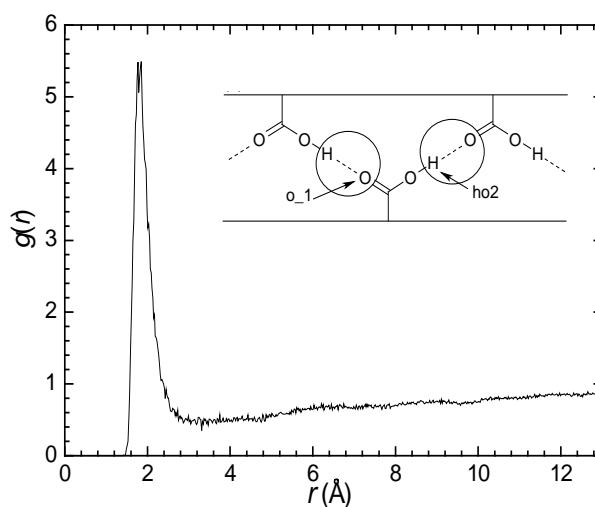
Figure 5.4 Radial distribution function between hydrogen and oxygen atoms of carboxyl groups in CX-PIM. The inset demonstrates hydrogen bonds.

To provide a deeper insight, radial distribution function was calculated to investigate the interactions between hydrogen and oxygen atoms of carboxyl groups in CX-PIM. As shown in **Figure 5.4**, a sharp peak is seen at 2 Å, indicating the formation of hydrogen bonds among carboxyl groups in polymer chains. A carboxyl

group can act as a donor as well as an acceptor to form hydrogen bonds. Consequently, the CX-PIM membrane is densely packed, possesses a higher density and a larger percentage of small voids compared to PIM-1 and TFMPS-PIM.

Furthermore, we estimate the FFVs in the three membranes. With a probe size equal to zero, the maximum FFVs are about 45.2%, 42.1% and 38.7% in PIM-1, TFMPS-PIM and CX-PIM, respectively. Consequently, the fractional van der Waals volumes ($V_{vdw}/V_{sp} = 1 - $ FFV) are 54.8%, 57.9% and 61.3%. Lee proposed an empirical method to calculate FFV [252]

$$FFV = 1 - 1.3 V_{vdw}/V_{sp} \qquad (5\text{-}1)$$

With this method, the FFVs in PIM-1, TFMPS-PIM and CX-PIM are estimated to be 28.8%, 24.7% and 20.3%, respectively. These agree quantitatively well with the FFVs calculated by Du et al. using the group contribution method [52]. The FFV decreases following PIM-1 > TFMPS-PIM > CX-PIM, which is consistent with void morphologies and void size distributions seen in **Figures 5.2** and **5.3**. Due to bulky groups in TFMPS-PIM or strong hydrogen bonds in CX-PIM, large voids are occupied or polymer chains are densely packed, and thus the FFV decreases.

Wide angle X-ray diffraction (WAXD) is commonly used to determine the crystallinity and intermolecular space of a membrane. From WAXD, d-spacing can be estimated using Bragg's law

$$d = \frac{\lambda}{2\sin\theta} \qquad (5\text{-}2)$$

where λ is the wavelength (1.789 Å) and θ the scattering angle.
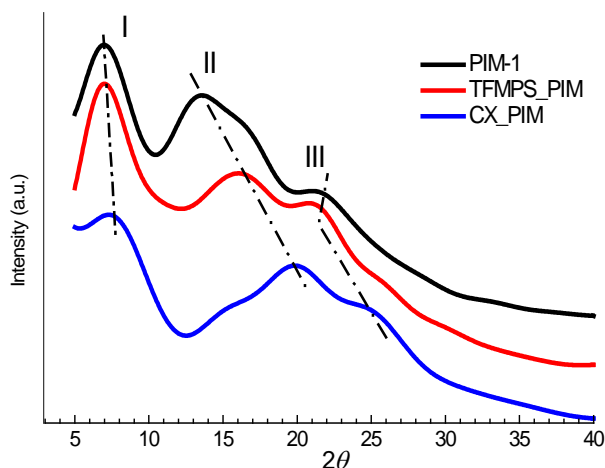
Figure 5.5 Simulated wide angle X-ray diffractions (WAXDs) in PIM-1, TFMPS-PIM and CX-PIM.

Figure 5.5 shows the calculated WAXDs of PIM-1, TFMPS-PIM and CX-PIM. They are in accord with the experimental data available for PIM-1 and TFMPS-PIM [52]. The broad distributions of WAXDs indicate that the three membranes are essentially amorphous. In each membrane, three peaks are observed. The first peak (I) is attributed to the neighboring spiro-carbon atoms. In PIM-1, the first peak is at $2\theta =$ 7° with a *d*-spacing of 14.69 Å, corresponding to the extended conformation of the PIM-1 backbone as illustrated in **Figure 5.6a**. This value is close to the spiro-carbon distance of 15 Å experimentally measured in PIM-1 [253]. It should be noted that Du *et al*. also observed by experiment that the spiro-carbon distance could be around 10 Å [169]. This is due to the bended conformation of backbone as shown in **Figure 5.6b**. Compared to PIM-1, the first peaks in TFMPS-PIM and CX-PIM shift marginally towards a higher angle, which implies a slightly shorter spiro-carbon distance. The second peak (II) is contributed from micropores in the PIM membranes [253]. The estimated *d*-spacing of peak II are 7.3 Å in PIM-1 and 6.4 Å in TFMPS-PIM, which match well with experimental values of 6.9 Å and 6.3 Å [52]. The *d*-spacing in CX-PIM is 5.2 Å and shorter than in PIM-1 and TFMPS-PIM because of the smaller free volume as discussed earlier. The third peak (III) is due to chain-to-chain correlations

between polymer backbones. The corresponding *d*-spacing is 4.7 Å in PIM-1 and close to the experimental 4.9 Å [52]. With bulky trifluoromethyl and phenylsulfone, particularly the latter, one might expect that the chain-to-chain distance in TFMPS-PIM would largely expand and subsequently the *d*-spacing would substantially increase from PIM-1. Nevertheless, **Figure 5.5** shows the increment is rather small. The plausible reason is that phenylsulfone acts as filler and occupies the large voids. The *d*-spacing of peak III in CX-PIM is 4.1 Å, shorter than in the other two membranes. This is because strong hydrogen bonds are formed between carboxyl groups; consequently, polymer chains are compactly packed and chain-to-chain distance is the shortest among the three membranes.
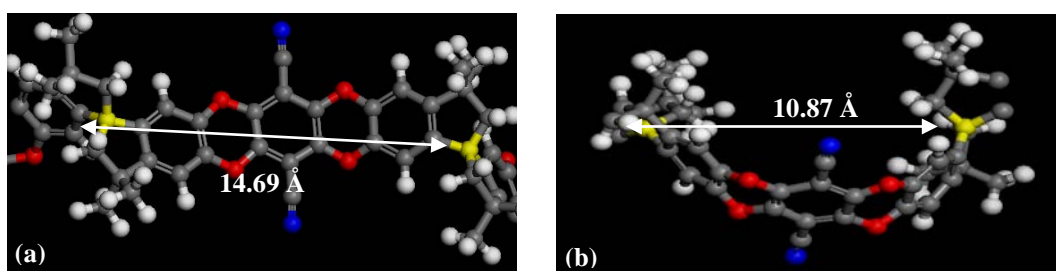
Figure 5.6 Distances between spiro-carbon atoms in PIM-1. (a) extended conformation (b) bended conformation. Color code: oxygen, red; nitrogen, blue; carbon, grey; hydrogen, white; spiro carbon, yellow.

5.3.2 Sorption

The sorption of a condensable gas species such as CO_2 in a membrane is largely related to the affinity of functional group. *Ab initio* calculations were used to evaluate the interactions between CO_2 and cyano, trifluoromethyl, phenylsulfone and carboxyl groups. The optimized structures and electrostatic potentials are illustrated in **Figure 5.7**, and the binding energies are listed in **Table 5.2**. Because of hydrogen bonds, carboxyl has the largest affinity for CO_2 (−13.29 kJ/mol) among the four functional groups. As indicated in **Figure 5.7d**, the distance from one oxygen atom in CO_2 to the

hydrogen atom in carboxyl is 2.06 Å, close to the distance observed in **Figure 5.4**.

With a large electro-negativity, phenylsulfone also strongly binds with CO_2 (−12.52

kJ/mol). Compared to carboxyl and phenylsulfone, cyano binds less strongly (−8.96

kJ/mol) and trifluoromethyl has the weakest affinity (−5.88 kJ/mol).

(a) cyano

(b) trifluoromethyl

(c) phenylsulfone

(d) carboxyl

2.06 Å

0.057 a.u.

-0.057 a.u.
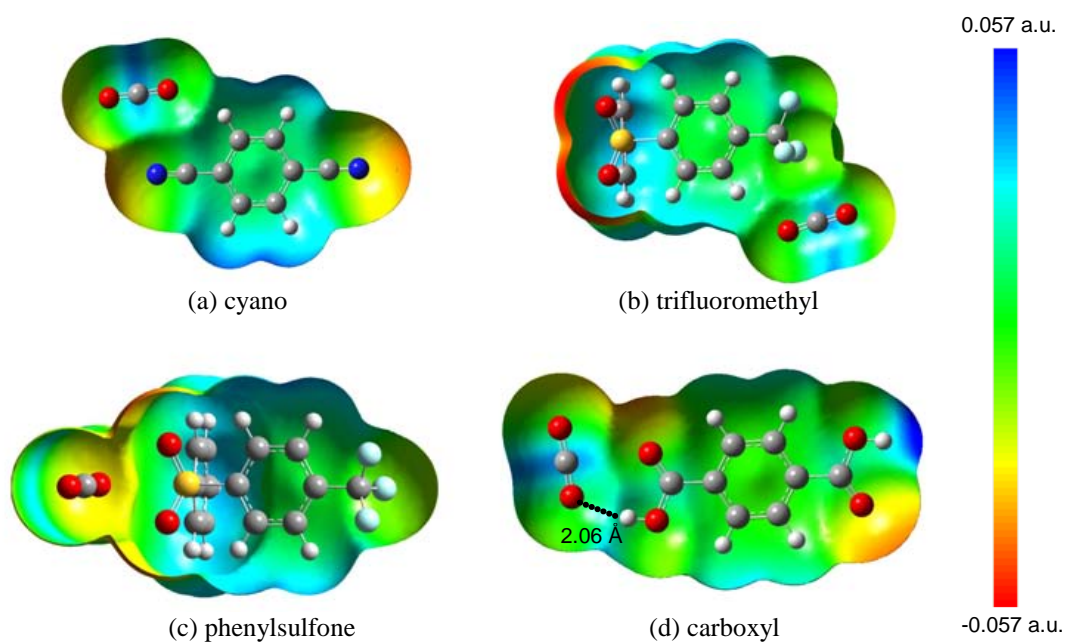
Figure 5.7 Optimized structures of CO_2 with functional groups (a) cyano (b) trifluoromethyl (c) phenylsulfone and (d) carboxyl. The scale of electrostatic potentials is in atomic unit (a.u.). Color code: oxygen, red; nitrogen, blue; carbon, grey; hydrogen, white; fluorine, cyan; sulfur, yellow. The distance between one oxygen atom in CO_2 and hydrogen atom in carboxyl is 2.06 Å.

Table 5.3 lists the simulated solubility coefficients of CO_2 and N_2 in PIM-1,

TFMPS-PIM and CX-PIM. For comparison, experimental data available in PIM-1

from the literature are also listed [155,162]. It should be noted that polymer

membranes are amorphous lacking well-defined crystalline structures, remarkably

different from crystalline materials (e.g. zeolites and MOFs). Therefore, experimental

data in polymer membranes could be significantly affected by preparation methods.

As seen in **Table 5.3**, there are large deviations in the experimental solubility data for

PIM-1 reported by different research groups or even the same research group.

Nevertheless, fairly good agreement is observed between simulation and experiment, particularly for CO_2 sorption in PIM-1. The deviations could be attributed primarily to two factors. First, the solubility in simulation was considered at 300 K and infinite dilution, which are not exactly identical to experimental conditions. Second, the force field for gas-polymer interactions may not be perfect and more accurate description is desired. Large deviations are usually seen in the literature between experimental and simulation data, e.g., 1−2 fold for N_2 and O_2 in polystyrenes [254], 1−5 fold for CO_2 and N_2 in PTMSP [255], 4−17 fold for CO_2 and N_2 in PEEK [256], and 1−55 fold for CO_2 and N_2 in polymides [96].

Table 5.3 Solubility coefficients [cm^3 (STP)/cm^3 (polymer) bar], diffusion coefficients [10^{-8} cm^2/s] and permeabilities [barrer] of CO_2 and N_2 in PIM-1, TFMPS-PIM and CX-PIM, respectively. The experimental temperature and pressure were 303 K and 0.2 bar [162], 298 K and 3.4 bar [52],[169], 308 K and 4 atm [155].

Membrane	Gas	S_{sim}	S_{exp}	D_{sim}	D_{exp}	P_{sim}	P_{exp}
PIM-1	CO_2	47.1 ± 7.6	66.0 [162], 22.2 [155]	102 ± 27	26 [162], 120 [155]	6390 ± 1981	2300 [162], 5366 [52], 8310 [169], 3496 [155]
	N_2	6.74 ± 0.53	3.2 [162], 1.54 [155]	223 ± 62	22 [162], 120 [155]	1999 ± 577	92 [162], 353 [52], 727 [169], 238 [155]
TFMPS-PIM	CO_2	48.4 ± 3.8	–	49.8 ± 17.8	–	3206 ± 1173	731 [52]
	N_2	5.58 ± 0.31	–	107.9 ± 5.7	–	801 ± 61	33 [52]
CX-PIM	CO_2	78.1 ± 8.0	–	9.8 ± 2.1	–	1018 ± 242	620 [169]
	N_2	6.47 ± 0.72	–	19.35 ± 10.66	–	166 ± 94	24 [169]

Table 5.3 also reveals the solubility of CO_2 in CX-PIM is substantially larger than in PIM-1 and TFMPS-PIM. This is consistent with the largest binding energy estimated from *ab initio* calculations, due to the formation of hydrogen bonds between CO_2 and carboxyl. In TFMPS-PIM, the averaged binding energy of CO_2 with phenylsulfone and trifluoromethyl is $(-12.52 - 5.88)/2 = -9.20$ kJ/mol, which is close to the binding energy between CO_2 and cyano (-8.96 kJ/mol). Therefore, the

solubility of CO_2 in TFMPS-PIM and PIM-1 is close. In remarkable contrast, different behavior is observed for incondensable N_2. N_2 solubility is, within statistical uncertainty, similar in the three membranes. The reason is that N_2 is a nonpolar molecule with a quadrupole moment smaller than CO_2. Consequently, the effect of functional group on N_2 solubility is not obvious.
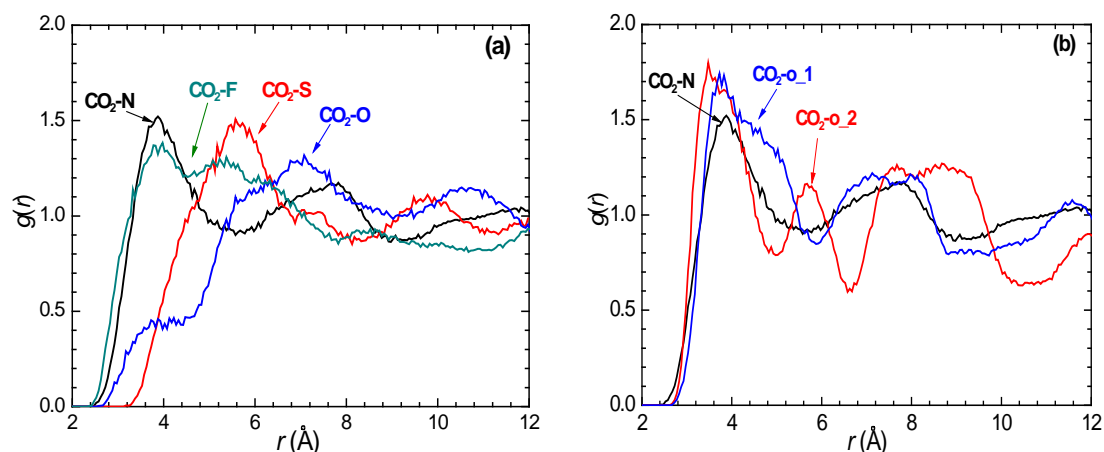
Figure 5.8 Radial distribution functions for CO_2 around (a) cyano, trifluoromethyl and phenylsulfone (b) cyano and carboxyl.

To characterize the structures of gas molecules adsorbed in the membranes, the radial distribution functions for CO_2 around functional groups were calculated in PIM-1, TFMPS-PIM and CX-PIM. As shown in **Figure 5.8a**, the peak height in the RDF of CO_2-N is similar to that of CO_2-S, and both are higher than the peak of CO_2-F or CO_2-O. This indicates that nitrogen atom in cyano and sulfur atom in phenylsulfone have similar affinity for CO_2 adsorption; however, fluorine atom in trifluoromethyl and oxygen atom in phenylsulfone have weaker affinity. On the other hand, **Figure 5.8b** shows that CO_2-O_1 and CO_2-O_2 have a higher peak than CO_2-N. As discussed above, this suggests carboxyl has a strong affinity than cyano for CO_2 and CO_2 solubility in CX-PIM is the largest.

5.3.3 Diffusion

Table 5.3 lists the simulated diffusion coefficients of CO_2 and N_2 in PIM-1, TFMPS-PIM and CX-PIM at 300 K. Comparison to an old set of experimental data in PIM-1[162] indicates that the simulation overestimates D_{CO_2} and D_{N_2} by 4−10 fold. With a new set of experimental data [155], however, good agreement between simulation and experiment is found particularly for D_{CO_2}. Similar to earlier discussion on the deviations between experimental and simulation solubility data, large deviation are also commonly observed between experimental and simulation diffusion data, e.g., 1−67 fold for CO_2 and N_2 in PEEK [256], up to 100 fold for N_2 and CO_2 in polyimides [96], and 8 fold for N_2 in poly(vinyl chloride) [136].

There are a number of factors that would cause discrepancies between simulated and experimental diffusion coefficients. (1) As pointed out earlier, the simulation was performed at 300 K and infinite dilution, differing from experimental conditions. (2) Simulation predicts self-diffusion coefficient, whereas experimental study typically reports transport diffusion coefficient. The self- and transport diffusion coefficients are identical only at infinite dilution, but experimental conditions are usually at finite pressure/concentration. (3) Accurate prediction of diffusion coefficient requires not only a good force field, but a well equilibrated model membrane. The procedure to construct a membrane can affect diffusion [257]. With the 'self-avoiding' random-walk method used to construct a membrane, anisotropy may exist and leads to a non-uniform distribution of polymer chains. Even if overall density is close to experimental density, the VSD in a model membrane may differ from that in a real membrane. (4) Polymer chain length also plays a role in diffusion [230]. A model membrane constructed with short chains tends to possess a larger FFV. Consequently, the predicted diffusion coefficient predicted is greater. For PIM-1, the weight-average

molar mass was determined experimentally as 370,000 g/mol [258], which means the degree of polymerization is about 797. In our simulation, however, the PIM-1 model had only 15 monomers and this would lead to a faster diffusion than measured. This result has been found in other simulation studies [63]. In addition, short polymer chains have a greater mobility, which in turn facilitates gas diffusion.

The diffusion coefficients of both CO_2 and N_2 in the three PIM membranes decrease in the order of PIM-1 > TFMPS-PIM > CX-PIM. Apparently for a membrane with a larger FFV, the coefficient is greater. To quantitatively evaluate the relationship, diffusion coefficients and FFVs were correlated using [259]

$$D = Ae^{-B/FFV} \tag{5-3}$$

where A and B are empirical constants related to the polymer and gas. As plotted in **Figure 5.9**, good correlations exist for both CO_2 and N_2 in the three membranes. With these molecular-based correlations, the diffusion coefficients in other membranes can be approximately predicted.
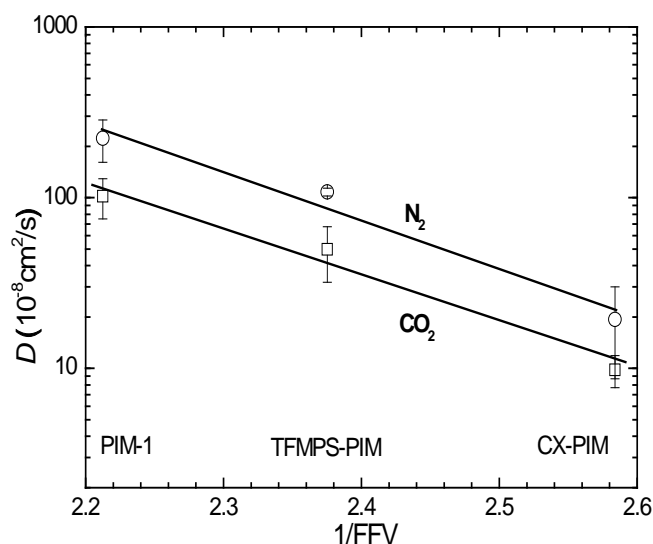
Figure 5.9 Correlations between diffusion coefficients of CO_2 and N_2 and fractional free volumes in PIM-1, TFMPS-PIM and CX-PIM.

5.3.4 Permeation and Selectivity

Permeation in a polymer membrane can be quantified by permeability $P = D \cdot S$ on the basis of the solution-diffusion mechanism. As listed in **Table 5.3**, the simulated permeabilities of CO_2 and N_2 are generally greater than experimentally measured values. For several reasons, as discussed above for the deviations between experimental and simulated solubility and diffusion data, thus certain degree of deviations are consequently observed between experimental and simulated permeabilities [260]. Moreover, as seen in **Table 5.3**, the discrepancies among different sets of experimental permeability data in PIM-1 are rather large. For both CO_2 and N_2, the permeabilities in the three membranes decrease following PIM-1 > TFMPS-PIM > CX-PIM. This is primarily due to the decreased diffusion coefficients, which roots in the reduced FFVs.
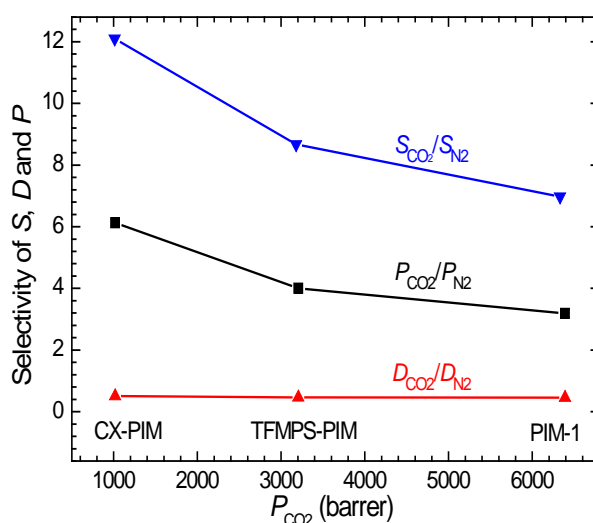
Figure 5.10 Sorption (S), diffusion (D) and permeation (P) selectivities of CO_2/N_2 in PIM-1, TFMPS-PIM and CX-PIM.

To evaluate the separation capability of a membrane, permselectivity between two species *i* and *j* is calculated by

$$\alpha_{i/j} = \frac{P_i}{P_j} = \frac{S_i}{S_j} \frac{D_i}{D_j} \tag{5-4}$$

where S_i / S_j is sorption selectivity and D_i / D_j is diffusion selectivity. **Figure 5.10** illustrates the simulated P_{CO_2} / P_{N_2}, S_{CO_2} / S_{N_2} and D_{CO_2} / D_{N_2} in PIM-1, TFMPS-PIM and CX-PIM. As can be seen, D_{CO_2} / D_{N_2} is nearly constant in the three membranes because CO_2 and N_2 possess similar kinetic diameters (3.30 Å for CO_2 and 3.64 Å for N_2). Nevertheless, S_{CO_2} / S_{N_2} increases in the order of PIM-1 < TFMPS-PIM < CX-PIM. S_{CO_2} / S_{N_2} in CX-PIM is twice of that in PIM-1. Similar to the increasing order of S_{CO_2} / S_{N_2}, P_{CO_2} / P_{N_2} also increases as PIM-1 < TFMPS-PIM < CX-PIM, which is consistent with experimental results [52,169]. This reveals that by tuning the functional groups from cyano in PIM-1 to trifluoromethyl and phenylsulfone in TFMPS-PIM, and then to carboxyl in CX-PIM, S_{CO_2} / S_{N_2} and P_{CO_2} / P_{N_2} increase.

5.4 Conclusions

Combining molecular simulation and quantum chemical calculation, the permeation and separation of CO_2/N_2 have been examined in three PIM membranes (PIM-1, TFMPS-PIM and CX-PIM). With a robust equilibration protocol to effectively construct model membranes, the predicted densities of model membranes match perfectly with experimental data (the deviations between experimental and predicted densities < 1%). Upon tuning cyano in PIM-1 to trifluoromethyl and phenylsulfone in TFMPS-PIM and to carboxyl in CX-PIM, the density increases and the FFV decreases. The bulky functional groups in TFMPS-PIM occupy large voids, leading to a decrease in the FFV; the polymer chains in CX-PIM are compactly packed due to the formation of hydrogen bonds among carboxyl groups. Consequently, CX-PIM exhibits the highest density and the lowest FFV. Three pronounced peaks are observed in the WAXDs of the model membranes. The

estimated peak positions and the correspondingly d-spacing distances agree well with experimentally measured results.

The simulated solubility and diffusion coefficients of CO_2 and N_2 match fairly well with available experimental data. As indicated by *ab initio* calculations and radial distribution functions, carboxyl has the strongest affinity for CO_2 and thus CO_2 has the highest solubility in CX-PIM. The diffusion coefficients of both gases decrease as PIM-1 > TFMPS-PIM > CX-PIM, following the reducing order of FFV. While the diffusion selectivity is largely independent on functional group, the sorption and permeation selectivity increase as PIM-1 < TFMPS-PIM < CX-PIM. This suggests that the sorption selectivity in functionalized PIM membranes dominate CO_2/N_2 separation. To achieve high-efficiency CO_2/N_2 separation, the PIM membranes should be tailored by functional groups which favor CO_2 sorption.

CHAPTER 6 EFFECTS OF RESIDUAL SOLVENT ON MEMBRANE STRUCTURE AND PERMEATION

6.1 Introduction

As reviewed in Chapter 2, extensive experimental studies have been conducted on gas permeation in polymer membranes, which is governed by several crucial factors such as polymer structure, backbone functionalization, and chain rigidity. In addition, a handful of experiments have revealed that the fabrication protocol of polymer membranes also affects performance. Joly et al. prepared 6FDA-*m*PDS PI films by spreading solutions from different solvents (CH_2Cl_2, dioxane, tetrahydrofurane, *N*-methyl-2-pyrrolidone and *N-N*-dimethyl acetamide) and found the solubilities, diffusivities and permeabilities of N_2 and CO_2 in the films were dependent on residual solvents [261]. Kostina et al. showed $CHCl_3$ resident in PEI could preferentially bind with oxygen atoms in membrane and lead to the conformational change of polymer chains [262]. Budd et al. observed a very strong sensitivity of gas permeability to casting method for PIM-1. In particular, PIM-1 membrane with residual H_2O exhibited a substantially low permeability [258].

Currently, it remains elusive how a residual solvent specifically interacts with a membrane and affects membrane microstructure and performance. In this regard, it is highly desired to understand the effects of residual solvent on membrane properties at a molecular-level. In this Chapter, simulation is performed for the effects of residual solvent on PIM-1 membrane structure and H_2 permeation. Three residual solvents (CH_3OH, $CHCl_3$ and H_2O) are considered and the simulation results are compared with the experimentally data by Budd et al. [258] The microscopic insight from simulation can assist in the fabrication of new membranes for gas purification. In

Section 6.2, the models and methods are described including how to construct PIM-1 membranes with residual solvents and to calculate H_2 sorption and diffusion. In Section 6.3, the membranes are characterized in terms of FFV and VSD. The interaction and mobility of solvent and polymer are discussed. The simulated solubility and diffusion coefficients of H_2 are presented and compared with experimental data.

6.2 Models and Methods

6.2.1 Membrane Construction
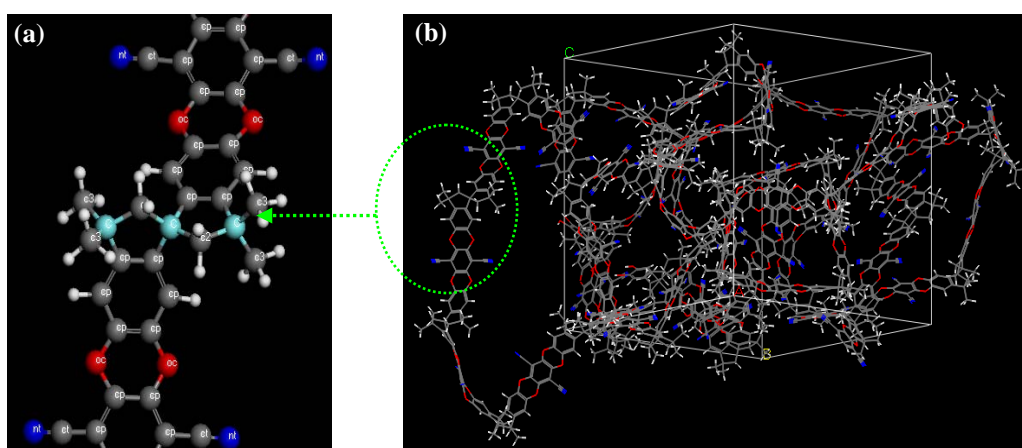
Figure 6.1 (a) Backbone of PIM-1 (the spiro carbons are denoted by 'C'). (b) Three dimensional simulation box of PIM-1 membrane (the box length is approximately 31.8 Å).

The atomistic model of PIM-1 membrane was constructed by *Amorphous Cell* module in Materials Studio 4.3 using Theodorou and Suter's scheme, as shown in **Figure 6.1** [211,250]. The model membrane was composed of three polymer chains in a periodic cubic simulation box (with a length of approximately 31.8 Å) and each polymer chain consisted of 15 repeat units. To prevent ring catenation during model construction, 200 CH_4 molecules were inserted into the box and removed after the model was built. Ten configurations were generated and three of them were selected for equilibration by the following subsequent procedure: (1) energy minimization; (2)

500 ps NVT-MD simulation at 600 K; (3) 500 ps NPT-MD simulation at 600 K at 1 bar; (4) thermal annealing at 1 bar from 600 K to 300 K with a temperature interval of 50 K. (5) 100 ps NPT-MD simulation at 10 bar with a time step of 0.1 fs. (6) 2000 ps NPT-MD simulation with a time step of 1 fs at 300 K and 1 bar.

Table 6.1 Physical properties of residue solvents [263].

Solvent	Molecular Weight	van der Waals Volume (Å^3)	Critical Volume (cm^3/mol)
CH_3OH	32.04	36.82	118
$CHCl_3$	119.38	70.55	239
H_2O	18.01	19.24	55.9

As in the experimental study [258], three residual solvents are considered including CH_3OH, $CHCl_3$ and H_2O. **Table 6.1** lists the physical properties of the three solvents [263]. Experimental thermogravimetric analysis revealed there were 0.5, 2.2 and 2.3% of CH_3OH, $CHCl_3$ and H_2O, respectively, in PIM-1 membrane [258]. Approximately, 4 CH_3OH, 4 $CHCl_3$ and 27 H_2O molecules existed in the simulation box shown in **Figure 6.1**. The residual solvent molecules were randomly inserted into the equilibrated PIM-1 model membrane, then equilibrated by 8000 ps NPT-MD simulation at 300 K and 1 bar, and finally by 2000 ps NVT-MD simulation.

All the energy minimization and MD simulation were conducted in DL_POLY [213]. The polymers were mimicked PCFF that has been demonstrated to be reliable for PIM membranes [264]. The Lennard-Jones interactions were calculated with a cutoff of 13 Å and the Coulombic interactions were treated by the Ewald summation with a precision of 10^{-6}. The VVA algorithm was used to integrate the equations of motion. Temperature and pressure were controlled by the Berendsen method with a decay constant of 0.6 ps. The equilibrated model membranes were characterized by FFV and VSD.

6.2.2 Sorption and Diffusion of H_2

Based on solution-diffusion mechanism, gas permeability P in a polymer membrane is equal to $S{\cdot}D$, in which S is solubility coefficient and D is diffusion coefficient. In this work, S and D of H_2 in the PIM-1/solvent membranes were calculated at room temperature and infinite dilution.

The sorption was calculated by Widom insertion method. The number of trial moves in the MC simulation was 2×10^7 with the first 10^7 moves for equilibration and the subsequent 10^7 moves for ensemble averages. Two types of trial moves were randomly attempted, namely, translation and rotation. In translation, H_2 molecule was translated with a random displacement in x, y or z dimension; and the maximum displacement was adjusted to an overall acceptance ratio of 50%. In rotation, H_2 molecule was rotated around x, y, or z dimension with a random angle; and the maximum angle was adjusted to an overall acceptance ratio of 50%.

The diffusion was simulated by NVT MD method. To improve statistical accuracy, three H_2 molecules were inserted into the membrane. At least half of the box length existed between the H_2 molecules to minimize their interactions. The MD simulation was performed for 13 ns, in which the first 2 ns was used for equilibration and the subsequent 11 ns for production. Similar to the MD simulation used for model construction, the LJ and Coulombic interactions were also calculated with a cutoff of 13 Å and the Ewald summation with a precision of 10^{-6}. Temperature was controlled by the Berendsen method with a decay constant of 0.6 ps. The mobility of H_2 was estimated from MSD.

6.3 Results and Discussion

6.3.1 Membrane Characterization

Table 6.2 lists the densities and FFVs of PIM-1/solvent membranes predicted from simulation. Compared to dry PIM-1 in the absence of solvent in Chapter 4, the density increases from 1.03 to 1.07 ~ 1.09 g/cm^3 and the FFV decreases from 47.7 to 44 ~ 45%. This is because the volume of membrane remains almost a constant in the absence/presence of solvent molecules and solvent molecules tend to occupy the voids in membrane; consequently, the density increases slightly. The increasing effect on density by residual solvent was also observed in PEI membranes [265]. It is worthwhile to note the FFVs in PIM-1 membranes are substantially larger than in common polyimide membranes (30 ~ 38%) [96], thus leading to a faster diffusion in PIM-1 membranes as discussed below.

Table 6.2 Predicted densities and fractional free volumes of PIM-1/solvent membranes.

Membrane	Density (g/cm^3)	FFV (%)
PIM-1/CH$_3$OH	1.07	44.88
PIM-1/CHCl$_3$	1.09	44.27
PIM-1/H$_2$O	1.09	43.67

Figure 6.2 shows the VSDs in PIM-1/solvent membranes. Due to the presence of solvent molecules, the largest voids (8 Å) in the three membranes are smaller than that (9 Å) in dry PIM-1 [264]. The percentage of large voids (> 6 Å) decreases following the order of PIM-1/CH$_3$OH > PIM-1/CHCl$_3$ > PIM-1/H$_2$O, in accordance with experimental PALS method [258]. As listed in **Table 6.1**, CHCl$_3$ has a van der Waals (vdW) volume larger than that of CH$_3$OH; therefore, CHCl$_3$ occupies a greater void space and PIM-1/CHCl$_3$ has a smaller percentage of large voids. Although H$_2$O has the smallest vdW volume among the three solvents, 27 H$_2$O molecules (vs. 4

CH_3OH or $CHCl_3$ molecules) exist in PIM-1/H_2O membrane and occupy a larger number of voids. Consequently, PIM-1/H_2O contains fewer large voids compared with PIM-1/CH_3OH and PIM-1/$CHCl_3$. Gas diffusion in a polymer membrane is largely governed by large voids. As expected, the diffusion coefficient of H_2 in PIM-1/H_2O is lower than in the other two membranes.
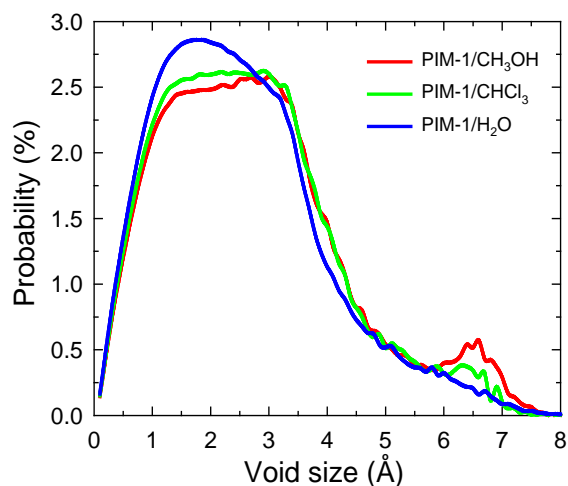
Figure 6.2 Void size distributions in PIM-1/solvent membranes.

It was observed from simulation that 4 CH_3OH molecules in PIM-1/CH_3OH or 4 $CHCl_3$ molecules in PIM-1/$CHCl_3$ remain essentially separated during the entire simulation. Nevertheless, H_2O molecules in PIM-1/H_2O behave differently. As shown in **Figure 6.3**, initially 27 H_2O molecules are randomly distributed in membrane, but they form into clusters after 5 ns. Indeed, experimental IR spectroscopy indicated that alcohol in PIM-1 exists as monomers but H_2O as associates [265]. Therefore, we infer that PIM-1 is a hydrophobic membrane, in which highly polar H_2O is not preferentially to interact with the polymer network and tends to aggregate. As a result of the formation of large clusters occupying large voids, PIM-1/H_2O membrane possesses the lowest percentage of large voids among the three PIM-1/solvent membranes.
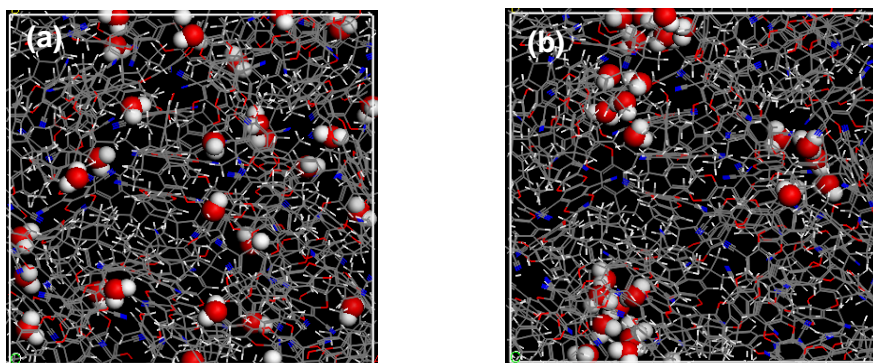
Figure 6.3 Simulation snapshots of PIM-1 with 27 residual water molecules. (a) Initial structure with water molecules randomly inserted in simulation box. (b) Equilibrium structure after 5 ns simulation.

6.3.2 Polymer-Solvent Interaction and Mobility

To quantify polymer-solvent interaction, **Figure 6.4** shows the distributions of interaction energy between a single solvent molecule and PIM-1. A sharp peak is seen for $CHCl_3$ and CH_3OH, but not for H_2O. The probability and energy value decrease in the order of $CHCl_3 > CH_3OH > H_2O$, which is consistent with the decreasing order in solvent hydrophobicity. Among the three solvents, $CHCl_3$ is the most hydrophobic, then CH_3OH and finally H_2O. Therefore, the interaction between $CHCl_3$ and hydrophobic PIM-1 is the strongest and the weakest interaction is seen for H_2O. This implies that the primary interaction between solvent and PIM-1 is hydrophobic.
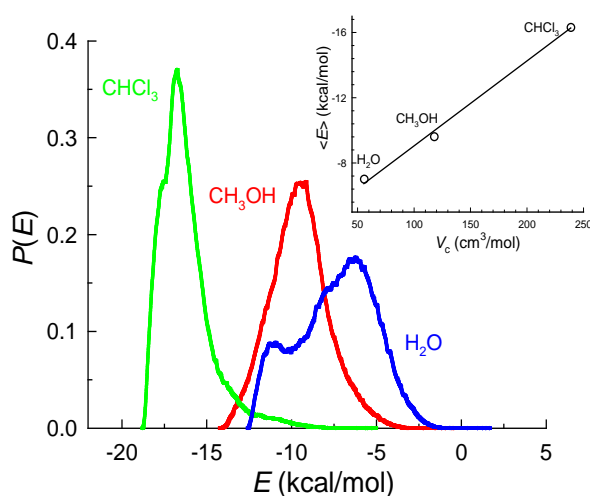
Figure 6.4 Distributions of interaction energy E between a single solvent molecule and PIM-1. The inset is the ensemble averaged energy $<E>$ versus solvent volume.

Based on the energy distribution, ensemble averaged energy $<E>$ was evaluated from

$$<E>=<\frac{\int E(\mathbf{r},\varpi)\exp[-\beta E(\mathbf{r},\varpi)]\mathrm{d}\mathbf{r}\mathrm{d}\varpi}{\int \exp[-\beta E(\mathbf{r},\varpi)]\mathrm{d}\mathbf{r}\mathrm{d}\varpi}> \qquad (6\text{-}1)$$

For $CHCl_3$, CH_3OH and H_2O, $<E>$ are approximately -16.3, -9.6 and -7.0 kcal/mol, respectively. The experimentally measured values are -14.4 and -10.2 kcal/mol for $CHCl_3$ and CH_3OH (not available for H_2O). Fairly good agreement is found between predicted and experimental $<E>$. It is recognized that hydrophobic interaction is largely proportional to molecular size [266]. Therefore, we plot $<E>$ as a function of the critical volume of solvent V_c. As shown in the inset of **Figure 6.4**, $<E>$ increases when V_c becomes larger. A good correlation (the correlation determinant $R^2 = 0.9957$) is found between $<E>$ and V_c:

$$<E> = -3.89 - 0.051V_c \qquad (6\text{-}2)$$

This molecular-based structure-property relationship can be used to predict the interaction energies for other solvents in PIM-1.

A polymer chain contains various groups that experience different interactions with residual solvent. To elucidate this, radial distribution functions (RDFs) between solvent molecules and (a) nitrogen atoms in cyano groups, (b) oxygen atoms in dioxanes, (c) carbon atoms in phenyl rings, and (d) spiro carbon atoms were calculated. A common feature in the RDFs observed in **Figure 6.5** is that H_2O exhibits a peak at the shortest distance because it has the smallest size among the three solvents, in contrast to CH_3Cl with a peak at the longest distance. More importantly, different profiles are observed in the RDFs for the four different types of atoms in PIM-1. As shown in **Figure 6.5a**, the peak around nitrogen atoms in cyano

groups drops following the order of $CH_3OH > H_2O > CHCl_3$, implying CH_3OH has the strongest interaction with cyano groups. A similar trend is observed in **Figure 6.5b** around oxygen atoms in dioxanes, except that $CHCl_3$ exhibits a higher peak than H_2O because of the favorable interaction between $CHCl_3$ and carbon atoms in dioxanes. It is also seen in **Figures 6.5c** and **6.5d** that $CHCl_3$ as well as CH_3OH have a higher peak than H_2O around carbon atoms. Overall, the structural analysis in **Figure 6.5** reveals that polar cyano and dioxane groups interact more preferentially with hydrophilic CH_3OH and H_2O, whereas less polar carbon atoms favor the interaction with hydrophobic $CHCl_3$. This is a consistent with the interaction energies discussed above.
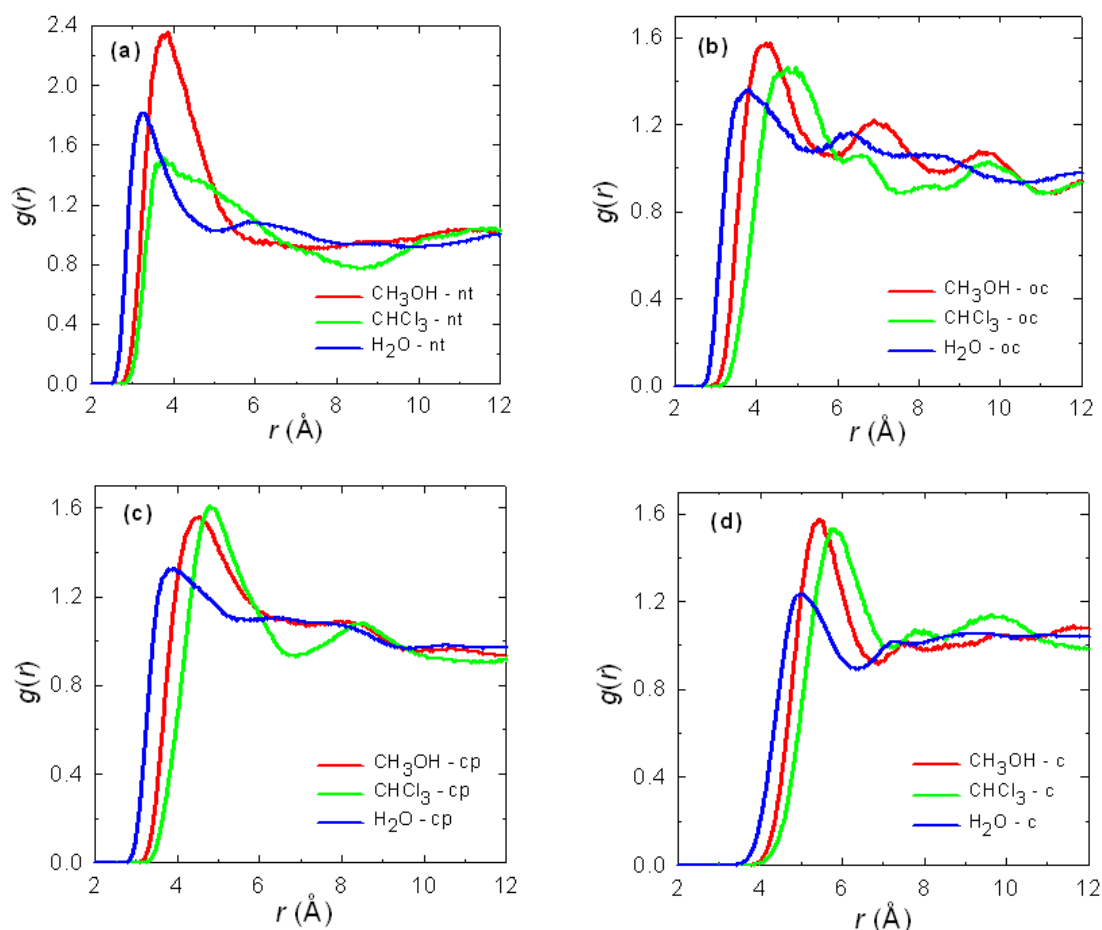
Figure 6.5 Radial distribution functions $g(r)$ between solvent molecules and (a) nitrogen atoms in cyano groups, (b) oxygen atoms in dioxanes, (c) carbon atoms in phenyl rings, and (d) spiro carbon atoms.

Figure 6.6 shows the MSDs of solvent molecules in PIM-1/solvent membranes. The mobility decreases in the order of $H_2O > CH_3OH > CHCl_3$ as attributed to two factors. First, the molecular weight increases following $H_2O < CH_3OH < CHCl_3$. However, H_2O tends to form clusters with heavier weight than CH_3OH, thus the molecular weight may not be the major factor. Second, the interaction strength with polymer increases with increasing degree of hydrophobicity $H_2O < CH_3OH < CHCl_3$. We speculate this may play a more dominant role in governing the mobility of solvent.
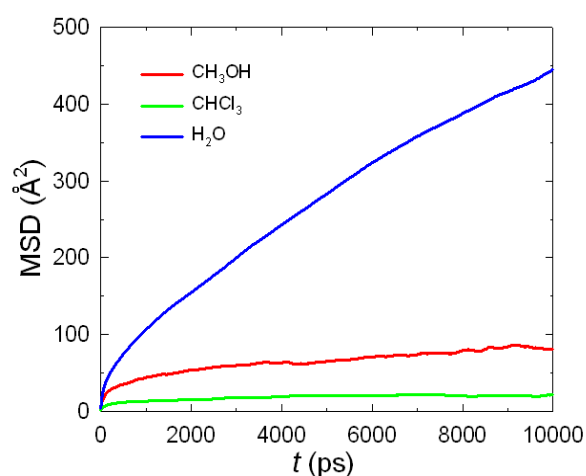
Figure 6.6 Mean-squared displacements of solvent molecules in PIM-1/solvent membranes.
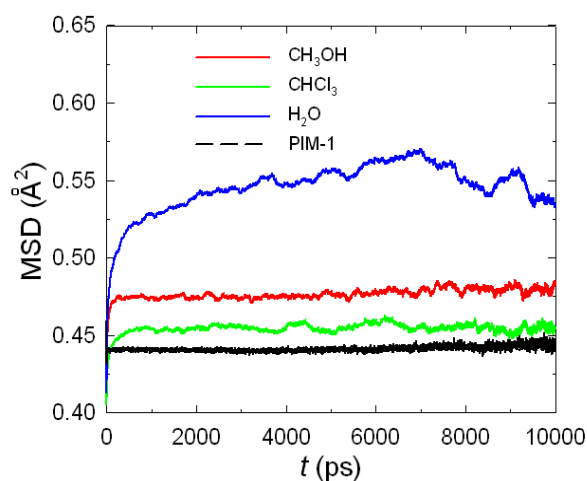
Figure 6.7 Mean-squared displacements of polymer chains in PIM-1/solvent membranes.

Figure 6.7 shows the MSDs of polymer chains in PIM-1/solvent membranes. Compared to residual solvents, the mobility of polymer chains is negligible. Nevertheless, the mobility increases in the same order as observed in **Figure 6.6**. The reason is that solvent molecules in membrane can be considered as a part of membrane skeleton. Therefore, the mobility of solvent and polymer is cooperative and a larger mobility of the former facilitates the mobility of the latter. Moreover, **Figure 6.7** indicates the mobility of polymer chains is enhanced in the presence of residual solvent. This is because solvent-polymer interaction leads to a relatively weaker polymer-polymer interaction and a looser polymer network. Such a phenomenon is analogous to CO_2-included plasticization of 6FDA-ODA membrane [267].

6.3.3 H_2 Sorption and Diffusion

Table 6.3 Solubility coefficients S [10^{-3} cm^3 (STP)/cm^3 cmHg] and diffusion coefficients D (10^{-8} cm^2/s) of H_2 in PIM-1/solvent membranes.

Solvent	$S_{sim.}$	$S_{exp.}$ [258]	$D_{sim.}$	$D_{exp.}$ [258]
PIM-1/CH$_3$OH	5.0 ± 0.1	6.6	6471 ± 481	5000
PIM-1/CHCl$_3$	4.8 ± 0.1	6.9	3513 ± 423	2900
PIM-1/H$_2$O	4.2 ± 0.1	2.7	2326 ± 604	1000

Table 6.3 lists the solubility coefficients of H_2 in PIM-1/solvent membranes. Good agreement is found between predicted and experimental data. The solubility decreases following PIM-1/CH$_3$OH > PIM-1/CHCl$_3$ > PIM-1/H$_2$O, which is in accordance with the decreasing order of FFV in the three membranes and implies solubility is proportional to FFV. Compared to dry PIM-1 membrane, the solubility in the presence of solvent is smaller as observed experimentally [258]. The reason is solvent molecules can bind/block sorption sites and thus lead to a reduction in H_2 sorption.

This effect induced by residual solvent was also observed for the solubility of N_2 in 6FDA-mPDA [261].
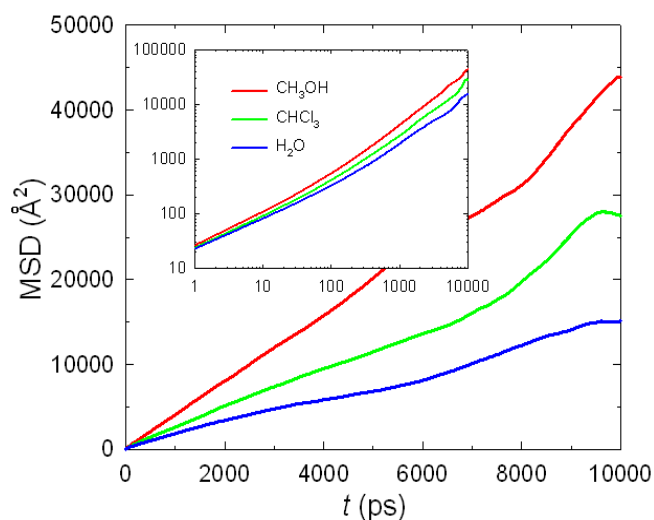
Figure 6.8 Mean-squared displacement of H_2 in PIM-1/solvent membranes. The inset is in log-log scale.

Figure 6.8 shows the MSDs of H_2 in PIM-1/solvent membranes. As indicated by the inset, the MSDs scale with t after approximately 1000 ps. This implies that H_2 reaches normal diffusion in the three PIM-1/solvent membranes after 1000 ps. Consequently, diffusion coefficient can be estimated using the Einstein equation (4-6). It is commonly recognized that diffusion is faster in a membrane with a larger FFV, which is observed in **Table 6.3**. The diffusion coefficient in the PIM-1/solvent membranes decreases in the order of PIM-1/CH_3OH > PIM-1/$CHCl_3$ > PIM-1/H_2O. The trend is consistent with the decreasing order of FFV. The presence of solvent molecules reduces free volume and diffusion coefficient. Particularly, H_2O clusters occupy the large voids in PIM-1/H_2O and cause the largest reduction in free volume and diffusion. For the same reason, the diffusion in wet PIM-1 membrane is slower than that in dry PIM-1 membrane as experimentally observed [258].

Table 6.3 also compares the simulated and experimental diffusion coefficients of H_2. Fairly good agreement is found, despite one-fold overestimation in PIM-1/H_2O. There are a number of factors that would cause the discrepancy between simulation and experiment, as discussed in Section 5.3.3.

6.4 Conclusions

We have examined how residual solvents (CH_3OH, $CHCl_3$ and H_2O) in PIM-1 affect the microscopic structure of membrane and gas permeation. It is observed that the fractional free volume and large voids in PIM-1/solvent membranes decrease following $CH_3OH > CHCl_3 > H_2O$, in accordance with the measurement by positron annihilation lifetime spectroscopy. Among the three solvents, $CHCl_3$ interacts most strongly with hydrophobic PIM-1. However, H_2O does not preferentially interact with PIM-1 and thus aggregates into clusters. The average interaction energies predicted for $CHCl_3$, CH_3OH and H_2O are -16.3, -9.6 and -7.0 kcal/mol, respectively, which agree well with available experimental data. On this basis, a structure-property relationship is proposed between the critical volume of solvent and interaction energy. The analysis of radial distribution functions reveals that cyano and dioxane groups in PIM-1 interact preferentially with hydrophilic CH_3OH and H_2O, whereas carbon atoms favor the interaction with hydrophobic $CHCl_3$. It is found that the mobility of residual solvent decreases as $H_2O > CH_3OH > CHCl_3$, opposite to the increasing order of molecular weight and interaction strength with PIM-1. The mobility of polymer is vanishingly small but facilitated by solvent due to the cooperative interaction between polymer and solvent.

Both solubility and diffusion coefficients of H_2 in PIM-1/solvent membranes decrease in the order of $CH_3OH > CHCl_3 > H_2O$, which follows the decreasing order

of free volume. The predicted coefficients are in fairly good agreement with experimental results. The solubility and diffusion coefficients are smaller compared to those in dry PIM-1 membrane in the absence of solvent. This is because solvent molecules bind/block sorption sites and decrease free volume, thus leading to a reduction in both sorption and diffusion.

CHAPTER 7 POLY(IONIC LIQUID) MEMBRANES FOR CO_2 CAPTURE

7.1 Introduction

Since the industrial revolution, CO_2 concentration in the atmosphere has constantly increased due to the combustion of huge amount of fossil fuels such as coal, oil and gas [268]. The increased CO_2 has caused global warming and environmental problems. Several techniques have been proposed for CO_2 capture, including amine scrubbing, cryogenic distillation, adsorption and membrane-based separation. Proposed in the early 1930's, amine scrubbing has been practically used for CO_2 capture in power generation plants. However, amine regeneration at approximately 120 ℃ is energy intensive and there has been considerable interest in the development of energetically favorable new solvents. Recently, ionic liquids (ILs) have been considered as promising candidates for CO_2 capture [177]. Emerging as a unique class of green solvents, ILs are nonvolatile and nonflammable with high thermal stability. Numerous ILs can be synthesized with a wide range of cations and anions. Particularly, imidazolium-based ILs have been extensively investigated because of their high affinity for CO_2 [195,269,270].

There are two major problems to use ILs for CO_2 capture, i.e., the cost and high viscosity of ILs. As an alternative, supported IL membranes (SILMs) have been proposed with ILs impregnated into the pores of porous supports. SILMs reduce the amount needed and viscosity, thus increase separation efficiency. However, the primary disadvantage of SILMs is the weak stability of ILs. This is because supported ILs are retained by capillary force and may leach into liquid phase under high transmembrane pressure difference.

An intriguing attempt to overcome the stability limitation of SILMs is to use mechanically stable solid-state membranes of polymeric ILs (PILs) [186,187]. Since 2005, a handful of experimental studies have been carried out to investigate CO$_2$ sorption and separation in PILs. Shen and coworkers first reported trimethylammonium-based PILs exhibit unprecedentedly higher CO$_2$ adsorption capacity than ILs, as well as substantially faster CO$_2$ adsorption/desorption rates [178,185]. Upon grafting polyethylene glycol (PEG) onto PILs, they further found PEG-grafted PILs are less brittle than neat PILs and perform well in CO$_2$/N$_2$ separation [189]. Bara et al. measured gas permeation (CO$_2$, N$_2$ and CH$_4$) in styrene and acrylate containing, imidazolium-based PILs with varying *n*-alkyl substituents and observed a better performance compared to other polymer membranes [187]. They also demonstrated that PILs containing oligo(ethylene glycol) or nitrile-terminated alkyl polar substituents have excellent CO$_2$/N$_2$ separation and surpass the Robeson upper bound [188]. Li et al. synthesized vinyl functionalized imidazolium based PILs, which exhibit higher CO$_2$ permeability than the counterparts with polystyrene and polyacrylate backbones. In addition, they found gas solubility, diffusivity and permeability increase upon blending with free ILs [190,193].

For CO$_2$ in ILs, it has been recognized that anions generally play a more dominant role than cations [195]. Nevertheless, the effects of polyions and corresponding counterions for CO$_2$ in PILs remain elusive. For example, CO$_2$ sorption capacity in trimethylammonoium-based PILs was found to be influenced marginally by anions [196]. On the other hand, diallyldimethylammonium-based PILs with carboxylate anions, particularly the acetate anions, exhibit higher CO$_2$ sorption and CO$_2$/N$_2$ selectivity compared to sulphonate and inorganic anions [198]. Therefore, both polyions and counterions appear to have strong effects on CO$_2$ capture. However,

there is no quantitative understanding on these effects. Currently, the mechanisms of gas sorption, diffusion and permeation in PILs are not fully understood. In this context, simulation investigation of CO$_2$ capture in PILs is indispensable. To the best of our knowledge, however, there has not been any simulation study reported for gas separation in PILs.
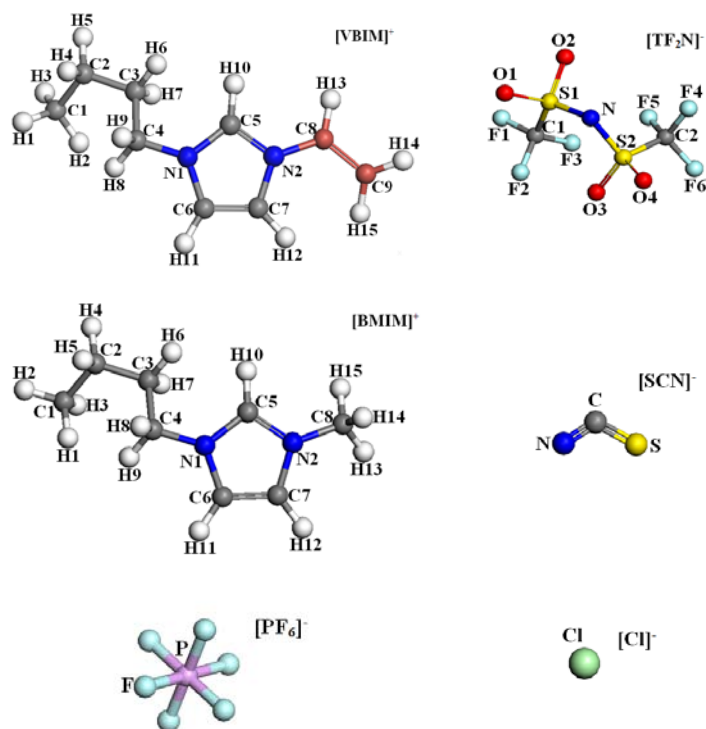
Figure 7.1 Chemical structures of [VBIM]$^+$, [TF$_2$N]$^-$, [BMIM]$^+$, [SCN]$^-$, [PF$_6$]$^-$ and [Cl]$^-$. The C8 and C9 atoms in [VBIM]$^+$ are the head and tail to form polymeric [VBIM]$^+$ chain.

In this Chapter, we conduct the first simulation study to examine the separation of CO$_2$/N$_2$ in PIL membranes. Four PILs based on 1-vinyl-3-butylimidazolium ([VBIM]$^+$) are considered with four anions of bis(trifluoromethylsulfonyl)imide ([TF$_2$N]$^-$), thiocyanate ([SCN]$^-$), hexafluorophosphate ([PF$_6$]$^-$) and chloride ion ([Cl]$^-$). Consequently, the effect of counterions can be quantitatively analyzed. In addition, two monomeric ILs namely [BMIM][TF$_2$N] and [BMIM][SCN] are considered. The cation [BMIM]$^+$ (1-butyl-3-methylimidazolium) has a structure very

similar to [VBIM]$^+$, as illustrated in **Figure 7.1**. By this comparison, the underlying difference between PILs and ILs membranes can be elucidated.

The simulation models and methods are described in Section 7.2 including the force fields used to represent PILs, ILs, CO$_2$ and N$_2$ molecules; MC and MD methods to simulate sorption, diffusion and permeation. In Section 7.3, the PIL and IL membranes are characterized in terms of density, solubility parameter, vaporization enthalpy, structure, dynamics, FFV and VSD. Thereafter, the interactions between gases (CO$_2$ and N$_2$) and membranes are examined. Following these, the solubility, diffusivity and permeability of CO$_2$ and N$_2$, as well as CO$_2$/N$_2$ selectivities are presented and compared with available experimentally measured data.

7.2 Models and Methods

7.2.1 Atomistic Models

The interactions of PILs and ILs include bonded and non-bonded terms. The bonded term U_{bonded} consists of

$$
\begin{aligned}
U_{\text{bonded}} = & \sum_b \left[k_2^b (b - b_0)^2 + k_3^b (b - b_0)^3 + k_4^b (b - b_0)^4 \right] \\
& + \sum_\theta \left[k_2^\theta (\theta - \theta_0)^2 + k_3^\theta (\theta - \theta_0)^3 + k_4^\theta (\theta - \theta_0)^4 \right] \\
& + \sum_\phi \left[k_1^\phi (1 - \cos \phi) + k_2^\phi (1 - \cos 2\phi) + k_3^\phi (1 - \cos 3\phi) \right] \\
& + \sum_\chi k^\chi (\chi - \chi_0)^2
\end{aligned}
\tag{7-1}
$$

where b, θ, ϕ, and χ represent bond length, bond angle, dihedral angle or out-of-plane angle formed by pairs, triplets and quadruplets, respectively. The non-bonded term $U_{\text{non-bonded}}$ has Lennard-Jones (LJ) and Coulombic potentials

$$
U_{\text{non-bonded}} = \sum_{i,j} \frac{q_i q_j}{4 \pi \varepsilon_0 r_{ij}} + \sum_{i,j} \varepsilon_{ij} \left[2 \left(\frac{r_{ij}^0}{r_{ij}} \right)^9 - 3 \left(\frac{r_{ij}^0}{r_{ij}} \right)^6 \right]
\tag{7-2}
$$

where ε_0 is the permittivity of vacuum, q_i is the atomic charge on atom i, and r_{ij} is the distance of between atoms i and j; ε_{ij} and r_{ij}^0 are the well depth and collision diameter of the LJ potential. The bonded and LJ potential parameters were adopted from the PCFF, which has been demonstrated to be accurate for polymeric systems [214]. The atomic charges in [VBIM]$^+$, [BMIM]$^+$ and [TF$_2$N]$^-$ were evaluated from density functional theory (DFT) calculations using the *Dmol^3* module in Materials Studio. The DNP basis set and BLYP functional were adopted. For [SCN]$^-$ and [PF$_6$]$^-$, DFT calculation was carried out with 6-311+G(d,p) basis set using Gaussian 09 package [271]. The atomic charges were estimated by fitting to the electrostatic potentials [272]. The atomic charge of [Cl]$^-$ was set as −1. **Tables 7.1-7.6** list the atomic charges in [VBIM]$^+$, [TF$_2$N]$^-$, [SCN]$^-$, [PF$_6$]$^-$, [Cl]$^-$ and [BMIM]$^+$.

Table 7.1 Atomic charges in [VBIM]$^+$. The C8 and C9 atoms are the head and tail to form polymeric [VBIM]$^+$ chain.

Atom	C1	C2	C3	C4	C5	C6	C7	C8	C9
Charge	-0.455	0.008	0.016	-0.416	-0.263	-0.128	-0.268	-0.084	-0.254
Atom	H1	H2	H3	H4	H5	H6	H7	H8	H9
Charge	0.155	0.120	0.133	0.065	0.062	0.067	0.071	0.182	0.185
Atom	H10	H11	H12	H13	H14	H15	N1	N2	
Charge	0.290	0.210	0.290	0.156	0.181	0.172	0.247	0.258	
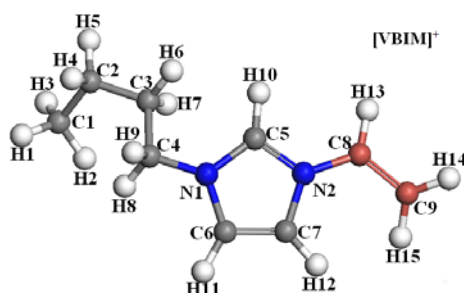
Table 7.2 Atomic charges in [TF$_2$N]$^-$.

Atom	C1	C2	S1	S2	O1	O2	O3	O4
Charge	0.268	0.219	0.721	0.773	-0.395	-0.444	-0.438	-0.400
Atom	N	F1	F2	F3	F4	F5	F6	
Charge	-0.569	-0.130	-0.123	-0.121	-0.126	-0.088	-0.147	

[TF$_2$N]$^-$
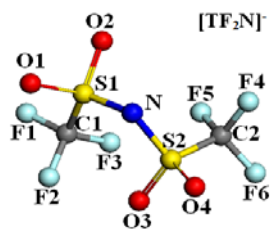
Table 7.3 Atomic charges in [SCN]$^-$.

Atom	C	N	S
Charge	0.459	-0.737	-0.722

[SCN]$^-$
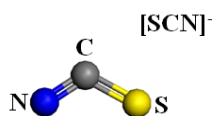
Table 7.4 Atomic charges in [PF$_6$]$^-$.

Atom	P	F
Charge	1.34	-0.39

[PF$_6$]$^-$
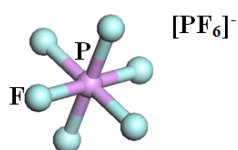
Table 7.5 Atomic charges in [Cl]$^-$.

Atom	Cl
Charge	-1.00

[Cl]$^-$
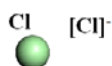
Table 7.6 Atomic charges in [BMIM]$^+$.

Atom	C1	C2	C3	C4	C5	C6	C7	C8	N1	N2
Charge	-0.486	0.048	0.027	-0.392	-0.257	-0.200	-0.224	-0.463	0.280	0.232
Atom	H1	H2	H3	H4	H5	H6	H7	H8	H9	H10
Charge	0.130	0.159	0.135	0.053	0.052	0.066	0.055	0.172	0.178	0.286
Atom	H11	H12	H13	H14	H15					
Charge	0.242	0.273	0.213	0.208	0.213					
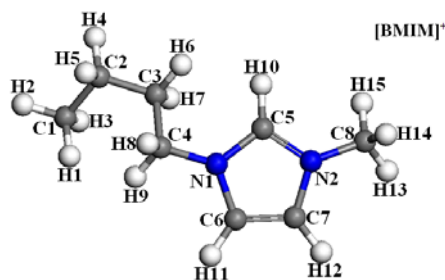
For each membrane, the model was constructed by the *Amorphous Cell* module in Materials Studio 5.5 (Accelrys Inc., San Diego, USA) using Theodorou and Suter's scheme [211,250]. A cubic simulation box with periodic boundary conditions was used. Polycation was mimicked to contain 30 [VBIM]$^+$ (denoted as poly[VBIM]$^{30+}$) arranged in a random torsional angle. The poly([VBIM][TF$_2$N]), poly([VBIM][SCN]), poly([VBIM][PF$_6$]) and poly([VBIM][Cl]) models were composed of two, three, two and three poly[VBIM]$^{30+}$ chains, respectively; and 60 [TF$_2$N]$^-$, 90 [SCN]$^-$, 60 [PF$_6$]$^-$ and 90 [Cl]$^-$ were included for electroneutrality. The monomeric [BMIM][TF$_2$N] and [BMIM][SCN] contained 60 pairs of [BMIM][TF$_2$N] and 80 pairs of [BMIM][SCN], respectively. The target membrane densities were 1.43, 1.06, 1.55, 1.10, 1.50 and 1.30 g/cm^3 for [BMIM][TF$_2$N], [BMIM][SCN], poly([VBIM][TF$_2$N]), poly([VBIM][SCN]), poly([VBIM][PF$_6$]) and poly([VBIM][Cl]), respectively. Fifty configurations were generated for each model membrane and ten configurations with lowest-energy were selected for equilibration using the robust protocol proposed in Chapter 5: (1) 5 × 10^6 steps of energy minimization at 0 K. (2) 300 ps NVT-MD simulation at 300 K. (3) 300 ps NVT-MD simulation at 800 K. (4) Repeat step 2 and 3 ten times. (5) 2000 ps NPT-MD simulation at 300 K and 1 bar. The energy minimization and MD simulation were conducted in DL_POLY 2.20 (Daresbury Laboratory, Warrington, UK) [273]. The structure files created by Materials Studio were converted to DL_POLY by an in-house developed code. The non-bonded

interactions were calculated with a cutoff of 12.5 Å and the Coulombic interactions were treated by Ewald summation with a precision of 10^{-6}. VVA algorithm was used in the MD simulations. Temperature and pressure were maintained by Berendsen method with a decay constant of 0.6 ps. After equilibration, the structural and dynamical properties of ions in the model membranes were examined. In addition, the membranes were characterized by FFV and VSD.

7.2.2 Gas Sorption and Diffusion

In this study, the sorption and diffusion of CO_2 and N_2 in the six membranes were evaluated at 308 K and infinite dilution. CO_2 was represented by the PCFF with a three-site partial charge model to mimic its quadrupole moment, while N_2 was represented as a two-site model by the COMPASS force filed [274]. The detailed parameters for CO_2 and N_2 are listed in **Table 7.7**.

Table 7.7 The van der Waals interaction parameters (nonbonded 9-6) and atomic partial charges for CO_2 and N_2. The CO_2 and N_2 parameters were from the PCFF and COMPASS, respectively.

Gas	Atom	σ_i [Å]	ε_i [kcal/mol]	Charge
CO_2	C	4.0100	0.0640	0.24
	O	3.5350	0.0600	-0.12
N_2	N	3.8008	0.0598	0.00

The solubility coefficient was calculated from the Widom insertion method as described in Section 4.2.2. The diffusion was simulated from MD method. For each species (CO_2 or N_2), three gas molecules were inserted into the simulation box. At least half of the box length existed between the gas molecules in order to minimize their interactions. MD simulation was performed for 8 ns with the first 2 ns used for

equilibration and the remaining 6 ns for production. The diffusivity was estimated from MSD and the multiple-origin method was used to calculate MSD.

7.3 Results and Discussion

7.3.1 Densities, Solubility Parameters and Vaporization Enthalpies

Table 7.8 lists the densities of six membranes [BMIM][TF$_2$N], [BMIM][SCN], poly([VBIM][TF$_2$N]), poly([VBIM][SCN]), poly([VBIM][PF$_6$]) and poly([VBIM][Cl]). The simulated values at 300 K and 1 atm were averaged from 10 independent configurations, and the small statistical uncertainties indicate the equilibration protocol to construct membranes is efficient. Except poly([VBIM][SCN]), poly([VBIM][PF$_6$]) and poly([VBIM][Cl]) for which measured densities are unavailable, the simulated and experimental densities of the other three membranes agree well with deviations of about $2 - 3\%$. Such a level of agreement is satisfactory because the PCFF was not specifically developed for ILs and PILs, and no parameters were adjusted to match experimental data. This suggests that the PCFF force filed is accurate to mimic the PILs and ILs under current study. The density increases in the order of [BMIM][SCN] < poly([VBIM][SCN]) < poly([VBIM][Cl]) < [BMIM][TF$_2$N] < poly([VBIM][PF$_6$]) < poly([VBIM][TF$_2$N]). As expected, monomeric ILs become more densely packed upon polymerization; therefore, PILs have a higher density than the counterpart ILs.

Table 7.8 Densities (g/cm^3) of [BMIM][TF$_2$N], [BMIM][SCN], poly([VBIM][TF$_2$N]), poly([VBIM][SCN]), poly([VBIM][PF$_6$]) and poly([VBIM][Cl]) membranes. The densities in ref. 274 and 275 are at 298.15 K. The density in ref. 190 is at 301.15 K. All the simulated densities are at 300 K.

Membrane	Sim.	Exp.
[BMIM][TF$_2$N]	1.473 ± 0.004	1.430 [190], 1.434 [275], 1.436 [275]
[BMIM][SCN]	1.040 ± 0.002	1.070 [276]
poly([VBIM][TF$_2$N])	1.583 ± 0.012	1.556 [190]
poly([VBIM][SCN])	1.124 ± 0.006	–
poly([VBIM][PF$_6$])	1.524 ± 0.012	–
poly([VBIM][Cl])	1.153 ± 0.009	–

For PILs, the density increases in the order of poly([VBIM][SCN]) < poly([VBIM][Cl]) < poly([VBIM][PF$_6$]) < poly([VBIM][TF$_2$N]). [PF$_6$]$^-$ and [TF$_2$N]$^-$ have a larger molecular weight than [SCN]$^-$ and [Cl]$^-$, thus their PILs exhibit a higher density. While [SCN]$^-$ has a larger molecular weight than [Cl]$^-$, [Cl]$^-$ has a smaller size and therefore poly([VBIM][Cl]) is more compact and exhibits a slightly higher density than poly([VBIM][SCN]).

For [BMIM][TF$_2$N] and [BMIM][SCN], experimental solubility parameters and/or vaporization enthalpies are available. These quantities were also estimated from simulation to further validate the force field. As a measurement of inter-molecular interaction, the solubility parameter δ is obtained from

$$\delta = \sqrt{\frac{E_{coh}}{V}} = \sqrt{\frac{E_{vac} - E_{bulk}}{V}} \tag{7-3}$$

where E_{coh} is the cohesive energy per mole and V is the molar volume. E_{vac} is the potential energy of a single IL pair in vacuum and E_{bulk} is that of a bulk IL. Since IL is nonvolatile, vaporization enthalpy ΔH^{vap} can be calculated approximately from

$$\Delta H^{vap} = E_{coh} + RT \tag{7-4}$$

where R is gas constant and T is temperature. **Table 7.9** lists the δ and ΔH^{vap} of [BMIM][TF$_2$N] and [BMIM][SCN] at 298 K and 1 atm. The simulated δ of [BMIM][TF$_2$N] is 24.5, within the range between 19.8 and 26.7 experimentally measured. Similarly, the ΔH^{vap} of [BMIM][TF$_2$N] from simulation is also within the experimental range. For [BMIM][SCN], the simulated and experimental δ agree fairly well. The comparison here further reveals that the force field used is accurate.

Table 7.9 Solubility parameters δ [(J/cm^3)$^{0.5}$] and vaporization enthalpies ΔH^{vap} [kJ/mol] of [BMIM][TF$_2$N] and [BMIM][SCN] at 298 K and 1 atm.

	Solubility Parameter δ		ΔH^{vap}	
	Exp.	Sim.	Exp.	Sim.
[BMIM][TF$_2$N]	19.8 [277], 20.9 [278], 21.2 [279], 25.5 [280], 26.7 [281]	24.5	134.0 [279], 191.0 [280], 208.2 [281]	174.3
[BMIM][SCN]	24.6 [282]	30.4	–	175.9

7.3.2 Membrane Structural Properties

To quantitatively examine the structural properties of ions in the membranes, radial distribution functions were calculated. **Figure 7.2** shows the $g(r)$ in [BMIM][TF$_2$N] and poly([VBIM][TF$_2$N]). In [BMIM][TF$_2$N], the $g(r)$ of cation–anion has two sharp peaks at distance $r = 4.2$ and 6.0 Å, respectively. This indicates the strong attraction between the oppositely charged cation and anion. In contrast, the $g(r)$ of cation–cation and anion–anion are broad and located at long distance $r = 8 - 10$ Å due to repulsion. In poly([VBIM][TF$_2$N]), the $g(r)$ of [TF$_2$N]$^-$–C8 and [TF$_2$N]$^-$–N2 exhibit pronounced peaks at approximately $r = 4.5$ Å. C8 atom is on the backbone of poly[VBIM]$^{30+}$ and N2 atom is next to the backbone; therefore, the pronounced peaks observed for both C8 and N2 atoms reveal anion [TF$_2$N]$^-$ interacts strongly with the backbone of poly[VBIM]$^{30+}$ chain. When the atom is away from the backbone, the peak height

drops and moves to a long distance as seen in the $g(r)$ of [TF$_2$N]$^-$–N1 and [TF$_2$N]$^-$–

C1. This implies the interaction of [TF$_2$N]$^-$ with the side-chain N1 and C1 atoms is

weaker compared to C8 and N2 atoms. The $g(r)$ of cation–cation and anion–anion in

[BMIN][TF$_2$N] and poly([VBIM][TF$_2$N]) are similar, i.e., with less pronounced peaks

at long distance.
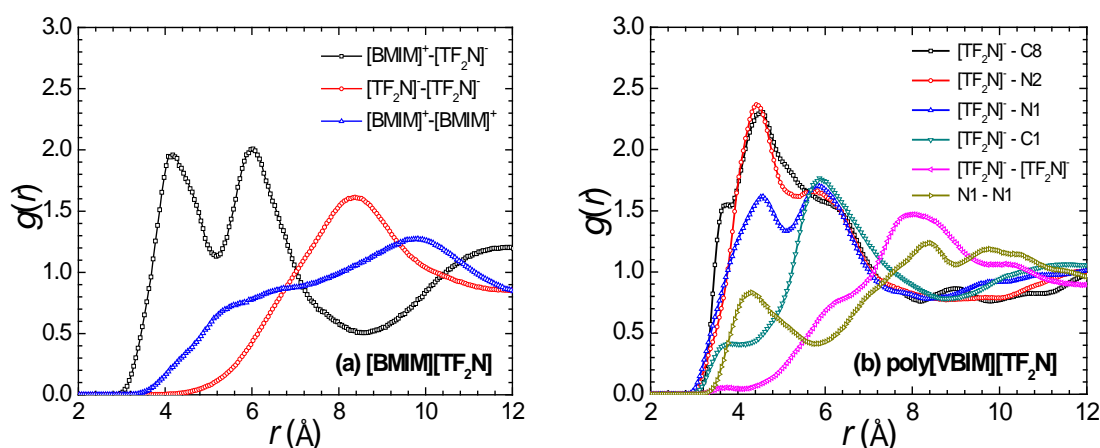
Figure 7.2 Radial distribution functions in (a) [BMIM][TF$_2$N] (b) poly([VBIM][TF$_2$N]).
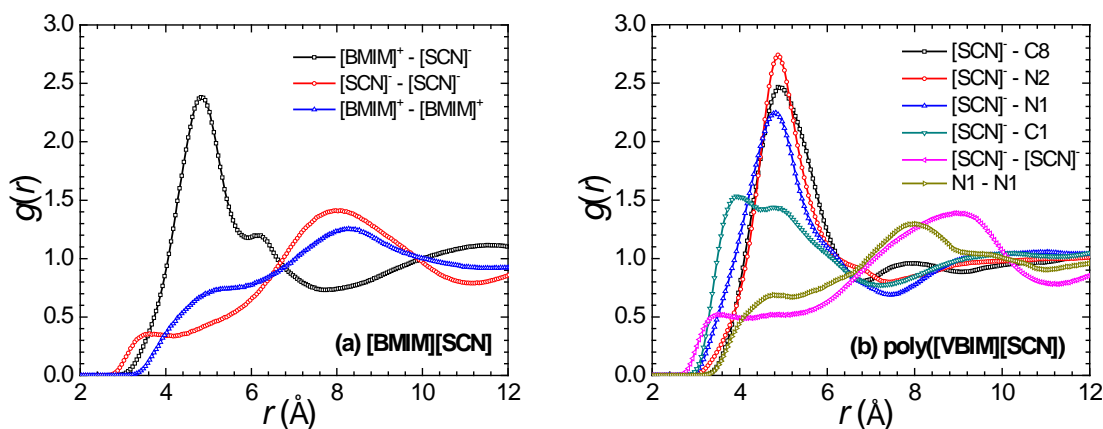
Figure 7.3 Radial distribution functions in (a) [BMIM][SCN] (b) poly([VBIM][SCN]).

Figure 7.3 shows the $g(r)$ in [BMIN][SCN] and poly([VBIM][SCN]), which

behave in the same pattern as in [TF$_2$N]$^-$-based counterparts. The primary difference

is that the peaks here are more pronounced than in **Figure 7.2**. This is attributed to the

smaller size of [SCN]$^-$ compared to [TF$_2$N]$^-$ and thus less steric restriction in [SCN]$^-$-based IL and PIL. Furthermore, the $g(r)$ in poly([VBIM][PF$_6$]) and poly([VBIM][Cl]) are shown in **Figure 7.4**, which have a largely same feature as in **Figures 7.2** and **7.3**. That is, N2 and C8 possess higher peaks compared to other atoms. It can be concluded for the four PILs that anions interact preferentially with the backbone (C8 and N2) atoms of polycation and this phenomenon is independent of the anion type.
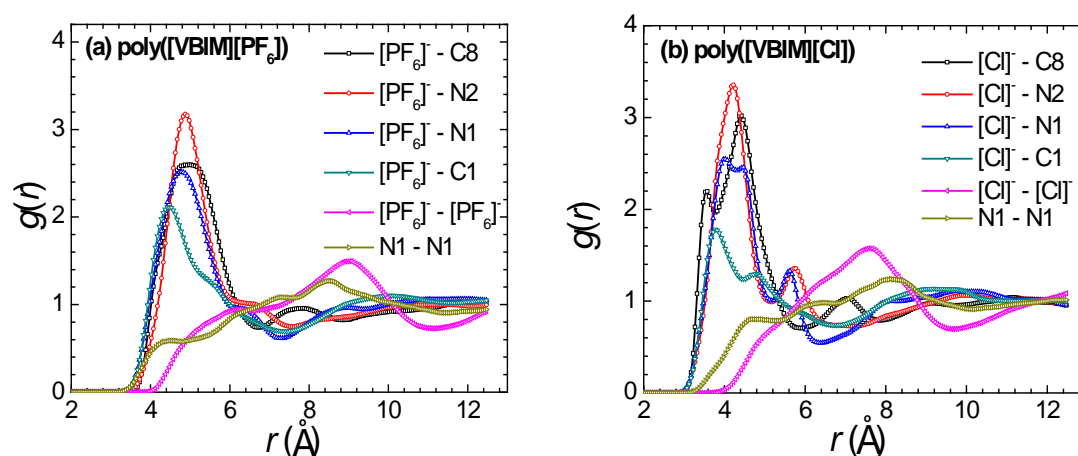
Figure 7.4 Radial distribution functions in (a) poly([VBIM][PF$_6$]) (b) poly([VBIM][Cl]).

7.3.3 Membrane Dynamic Properties

The dynamic properties of ions in the membranes are quantified by mean-squared displacements (MSDs). **Figure 7.5** shows the MSDs of ions in [BMIM][TF$_2$N] and [BMIM][SCN]. Despite bulky size, [BMIM]$^+$ exhibits higher mobility than both [TF$_2$N]$^-$ and [SCN]$^-$ anions. Such an interesting phenomenon was also observed in simulations [283,284] and experiments [285,286] for imidazolium-based bulk ILs, and interpreted as a result of the less hindered displacement of [BMIM]$^+$ ring along the direction of C5-H10 atoms (see **Figure 7.1**). Compared to [TF$_2$N]$^-$, [SCN]$^-$ has higher mobility because of the smaller size and lower molecular weight.
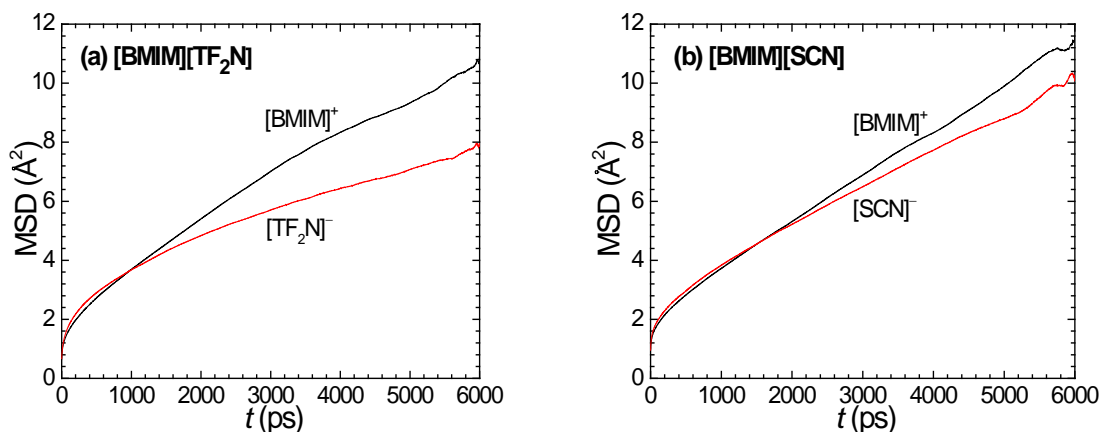
Figure 7.5 MSDs of (a) [BMIM]$^+$ and [TF$_2$N]$^-$ (b) [BMIM]$^+$ and [SCN]$^-$.
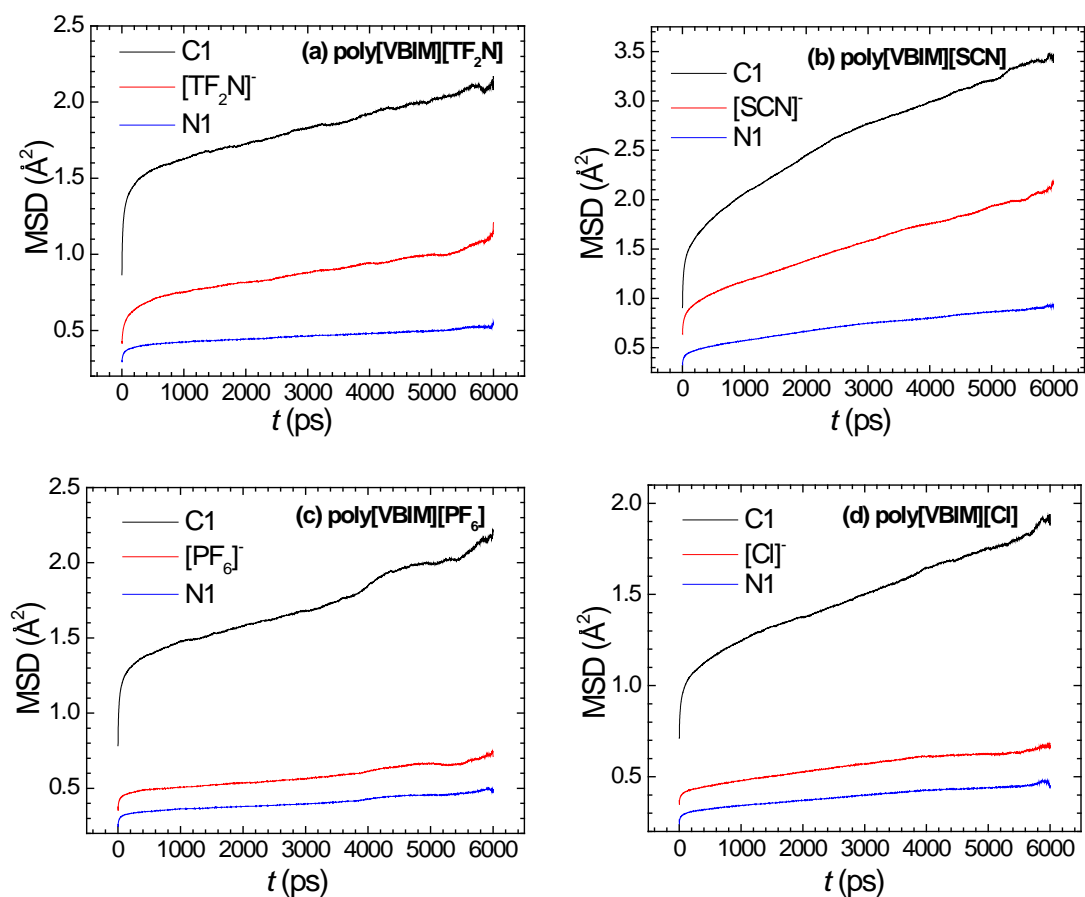
Figure 7.6 MSDs of C1, N1 atoms and anions in (a) poly([VBIM][TF$_2$N]) (b) poly([VBIM][SCN]) (c) poly([VBIM][PF$_6$]) (d) poly([VBIM][Cl]).

Figure 7.6 illustrates the MSDs of C1 and N1 atoms of poly[VBIM]$^{30+}$ chain, as well as anions, in poly([VBIM][TF$_2$N]), poly([VBIM][SCN]), poly([VBIM][PF$_6$]) and poly([VBIM][Cl]). Apparently, the ions in PILs possess lower mobility than in

ILs. This is because the transport pathway in PILs is largely blocked by chain connectivity, which reduces mobility. The MSDs of N1, C1 and anions increase in the order of N1 < anion < C1. N1 atom is next to poly[VBIM]$^{30+}$ backbone that barely moves, thus exhibits the lowest mobility among the three MSDs. C1 atom in the end group of side chain has the highest mobility and consequently creates a large transient void (or free volume) around C1 atom. This feature can significantly affect gas interaction with membrane, as well as gas sorption and diffusion. For example, Bara et al. found a long alkyl side chain of PILs largely enhances CO_2 diffusivity [187]. Li et al. also observed a substantial increase of CO_2 diffusivity in PILs by changing from ethyl to heptyl side chain [193]. The longer side chains are more flexible and thus create more transient void, which can facilitate gas diffusion.

7.3.4 Fractional Free Volumes and Void Size Distributions

Gas permeation in a membrane is largely governed by FFV and VSD. Based on a probe size equal to zero, the FFVs in [BMIM][TF$_2$N], [BMIM][SCN], poly([VBIM][TF$_2$N]), poly([VBIM][SCN]), poly([VBIM][PF$_6$]) and poly([VBIM][Cl]) are 36.2%, 37.8%, 33.0%, 34.9%, 31.9% and 34.0%, respectively. Because of chain connectivity, PIL has a smaller FFV than IL as also predicted by group contribution method [190]. Additionally, PIL with bulky anion, e.g. poly([VBIM][TF$_2$N]) and poly([VBIM][PF$_6$]) possesses a smaller FFV. The void morphologies of the two ILs and four PILs are illustrated in **Figure 7.7**.
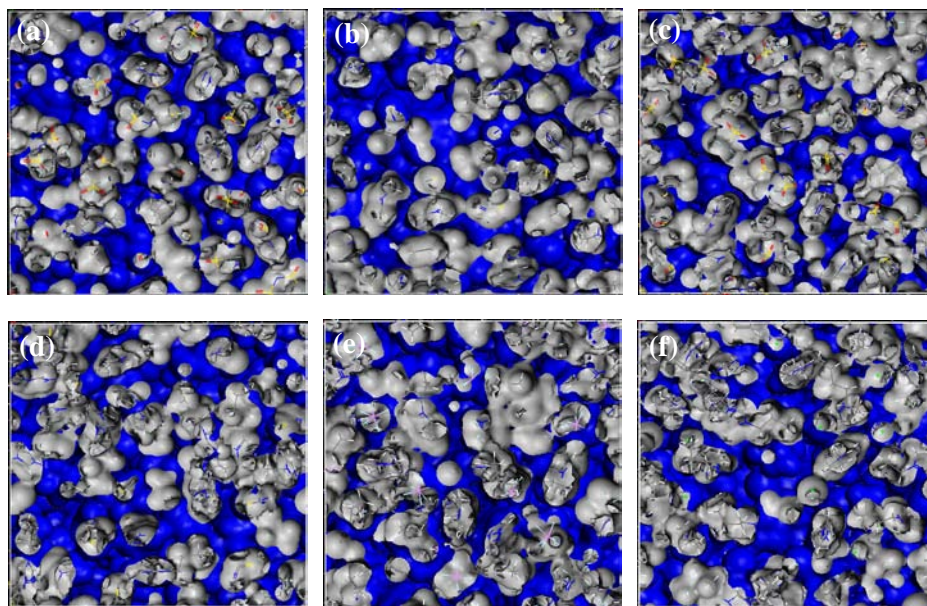
Figure 7.7 Void morphologies in (a) [BMIM][TF$_2$N] (b) [BMIM][SCN] (c) poly([VBIM][TF$_2$N]) (d) poly([VBIM][SCN]) (e) poly([VBIM][PF$_6$]) and (f) poly([VBIM][Cl]) membranes. The blue regions are voids and the grey regions are membrane networks.

Figure 7.8 shows the VSDs in [BMIM][SCN], [BMIM][TF$_2$N], poly([VBIM][SCN]), poly([VBIM][TF$_2$N]), poly([VBIM][PF$_6$]) and poly([VBIM][Cl]). Based on the void size, different patterns are observed in the VSDs. The percentage in the range of 0–1, 2–3, 3–4 and 4–5 Å has a similar pattern, in which the monomeric ILs have a smaller percentage compared to PILs. Nevertheless, the percentage in the range of 1–2 Å exhibits the opposite pattern. The largest void size is no more than 6 Å in the six membranes. This is in contrast to PIMs, in which the largest void is up to 9 Å as a consequence of rigid polymer chains and interconnected voids [287]. CO$_2$ and N$_2$ have kinetic diameters of about 3.30 and 3.64 Å, respectively. Thus only the large voids (> 3 Å in the inset) would predominately contribute to the diffusion of CO$_2$ and N$_2$.
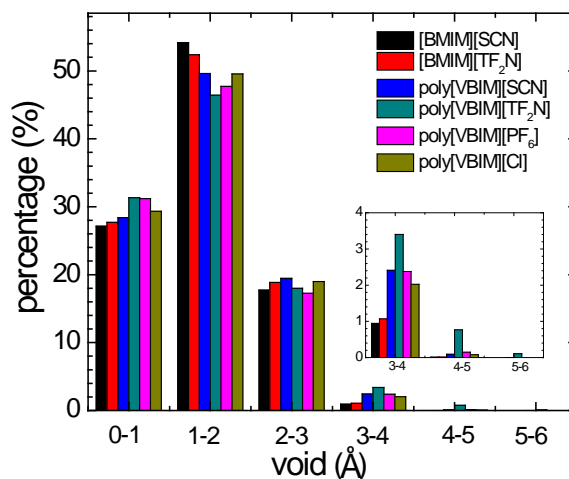
Figure 7.8 VSDs in [BMIM][SCN], [BMIM][TF$_2$N], poly([VBIM][SCN]), poly([VBIM][TF$_2$N]), poly([VBIM][PF$_6$]) and poly([VBIM][Cl]).

7.3.5 Gas-Membrane Interactions

The interactions between gases (CO$_2$ and N$_2$) and membranes are examined by analyzing radial distribution functions. **Figure 7.9a** shows the $g(r)$ of CO$_2$ around [BMIM]$^+$ in [BMIM][TF$_2$N] membrane. Sharp peaks are observed for C1 and C8 atoms at $r = 4$ Å. In contrast, N1 and N2 atoms have less pronounced peaks at $r = 5$ Å. This reveals CO$_2$ has the strongest interaction with the two ends of cation [BMIM]$^+$, but a relatively weaker interaction with the imidazolium ring. The $g(r)$ of CO$_2$ around [TF$_2$N]$^-$ shown in **Figure 7.9b** indicates the peak height decreases following C > N > F ≈ S > O. Thus, the C atom of [TF$_2$N]$^-$ has the strongest interaction with CO$_2$. Upon comparison with **Figure 7.9a**, C1 and C8 atoms of [BMIM]$^+$ and C atom of [TF$_2$N]$^-$ possess a close peak height at approximately the same distance, suggesting CO$_2$ has a similar interaction with the cation and anion in [BMIM][TF$_2$N]. These results are consistent with a simulation study in the literature [288]. **Figures 7.9c** and **7.9d** plot the $g(r)$ of N$_2$ in [BMIM][TF$_2$N]. Similar to the case of CO$_2$, the highest peak of N$_2$ around [BMIM]$^+$ is also seen in the two ends (C1 and C8 atoms), particularly the C1

atom. The peak height around $[TF_2N]^-$ decreases following $C > N > S \approx F > O$. Compared to N_2-C1, however, the peak height of N_2-C is lower.
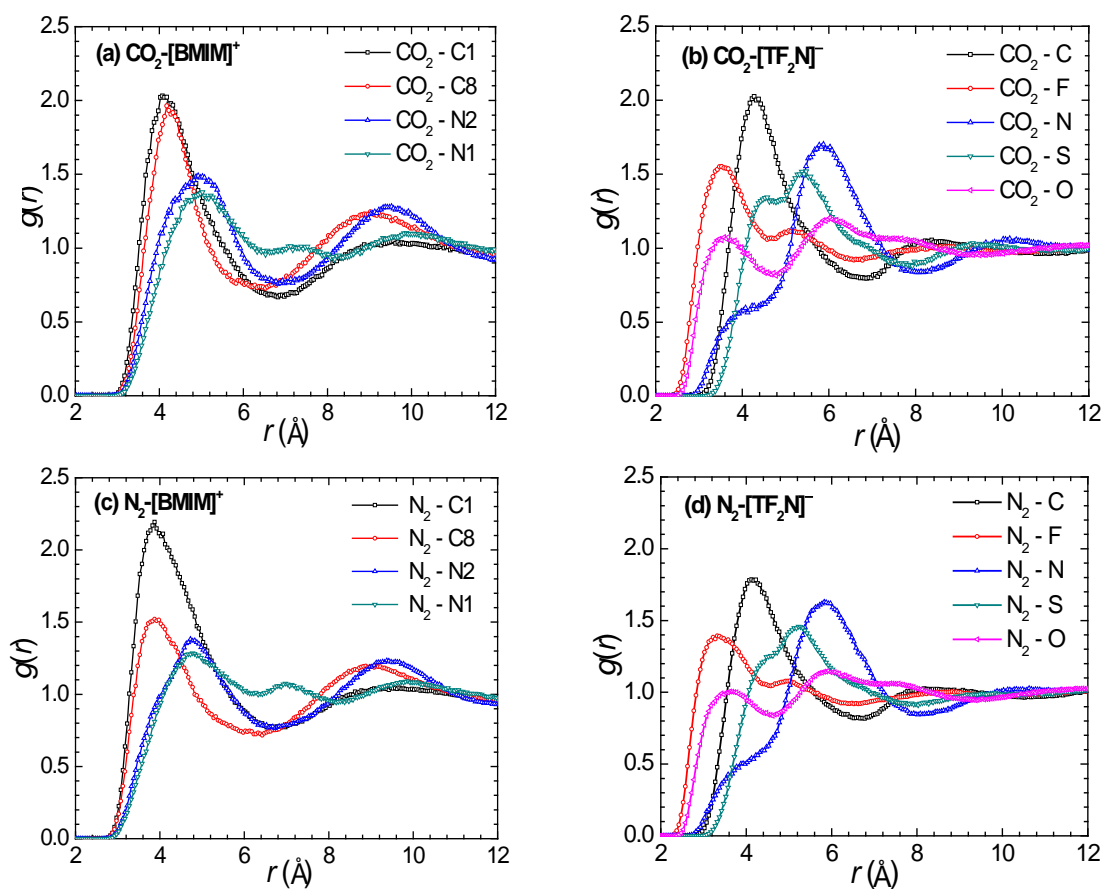
Figure 7.9 Radial distribution functions of CO_2 and N_2 in [BMIM][TF_2N] (a) CO_2-$[BMIM]^+$ (b) CO_2-$[TF_2N]^-$ (c) N_2-$[BMIM]^+$ (d) N_2-$[TF_2N]^-$.

Figure 7.10 illustrates the $g(r)$ of CO_2 and N_2 in [BMIM][SCN], which are generally similar to **Figure 7.9** in [BMIM][TF_2N]. Nevertheless, the $g(r)$ peaks of CO_2 around $[BMIM]^+$ are higher than those around $[SCN]^-$, implying that CO_2 interacts more strongly with $[BMIM]^+$ than with $[SCN]^-$, which is different from [BMIM][TF_2N].
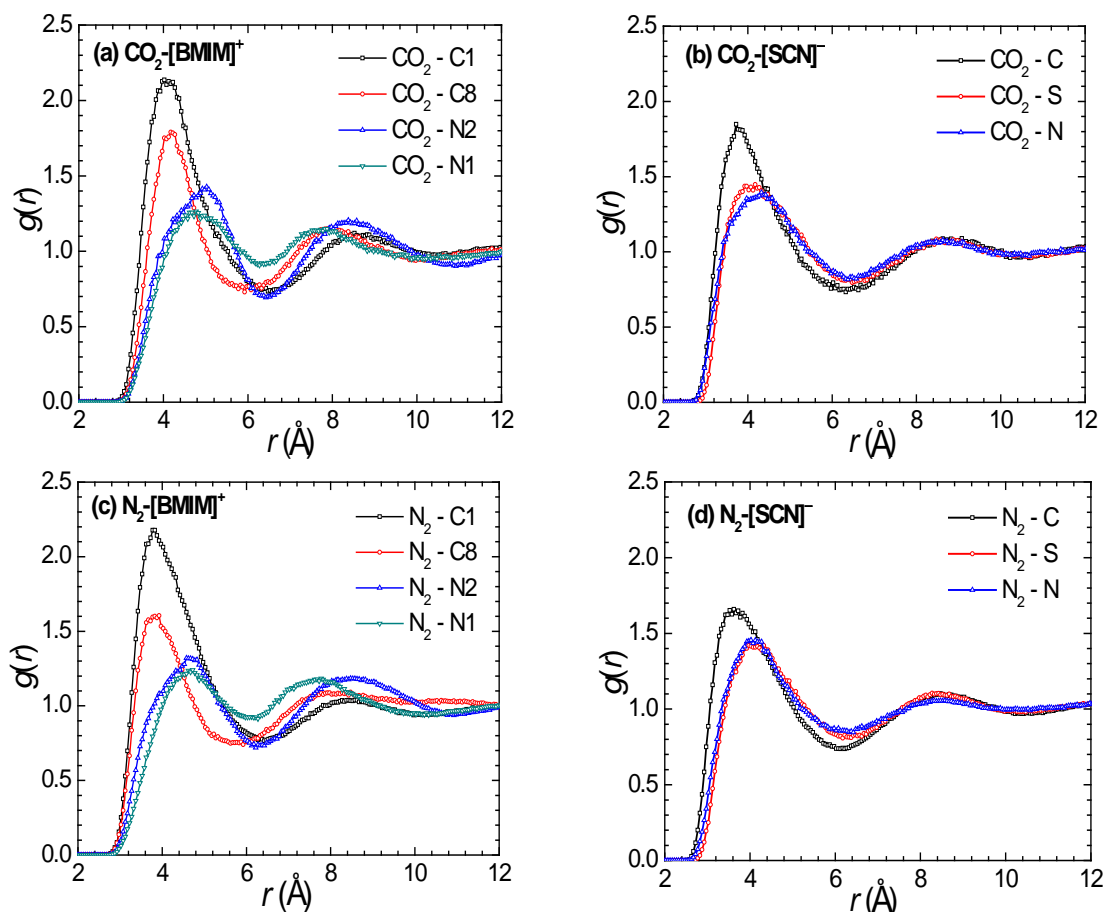
Figure 7.10 Radial distribution functions of CO_2 and N_2 in [BMIM][SCN] (a) CO_2-[BMIM]$^+$ (b) CO_2-[SCN]$^-$ (c) N_2-[BMIM]$^+$ (d) N_2-[SCN]$^-$.

Figure 7.11 represents the $g(r)$ of CO_2 and N_2 in poly([VBIM][TF$_2$N]). The $g(r)$ of CO_2 in poly([VBIM][TF$_2$N]) membrane is shown in **Figures 7.11a** and **7.11b**. Compared to **Figures 7.9a** and **7.9b** in [BMIM][TF$_2$N], the general trend around [TF$_2$N]$^-$ is nearly identical in both IL and PIL. However, there is a remarkable difference around cation. Specifically, a very sharp peak is seen in **Figure 7.11a** for the $g(r)$ of CO_2-C1, significantly higher than all other $g(r)$. This suggests CO_2 interacts most strongly with C1 atom than other cation atoms and anion. As discussed in **Figures 7.9a** and **7.9b** for [BMIM][TF$_2$N], the two ends of [BMIM]$^+$ (C1 and C8 atoms) possess a similar interaction with CO_2, and additionally cation and anion have a close interaction with CO_2. The situation is different for poly([VBIM][TF$_2$N]) membrane. C1 atom is the end of side chain in poly[VBIM]$^{30+}$, exhibits high mobility

(see **Figure 7.6**) thus creates a large free volume to accommodate CO$_2$; whereas C8 atom is in the backbone of poly[VBIM]$^+$, bonded with other atoms, and not readily accessible by CO$_2$. The $g(r)$ patterns of N$_2$ in **Figures 7.11c** and **7.11d** resemble those of CO$_2$. This reveals the strong interaction of CO$_2$ with C1 atom is not attributed to the quadrupolar moment of CO$_2$, rather due to the conformation of polycation (i.e. poly[VBIM]$^{30+}$).
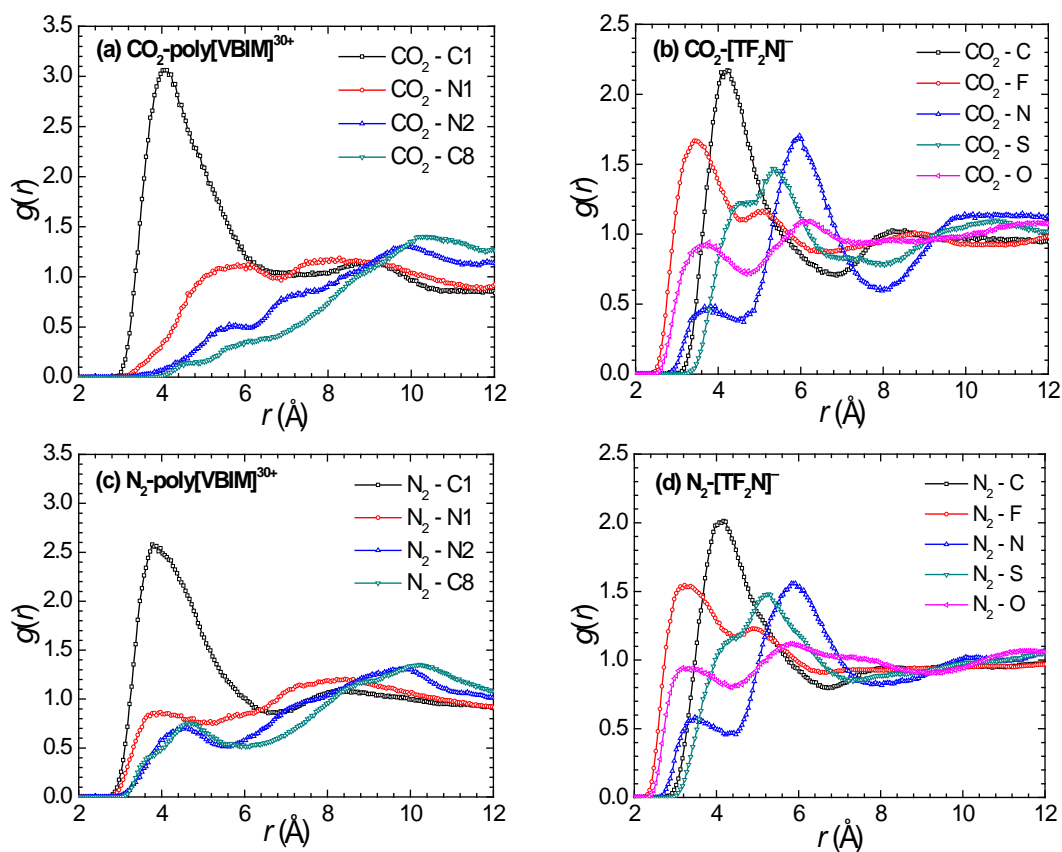
Figure 7.11 Radial distribution functions of CO$_2$ and N$_2$ in poly([VBIM][TF$_2$N]) (a) CO$_2$-poly[VBIM]$^{30+}$ (b) CO$_2$-[TF$_2$N]$^-$ (c) N$_2$-poly[VBIM]$^{30+}$ (d) N$_2$-[TF$_2$N]$^-$.
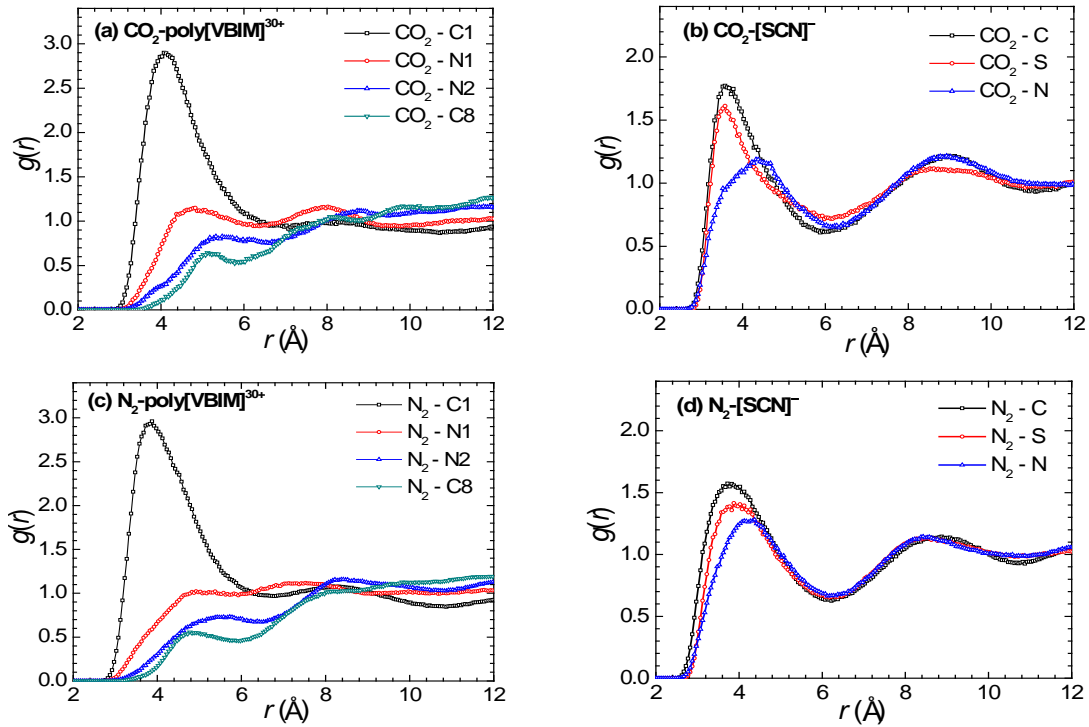
Figure 7.12 Radial distribution functions of CO$_2$ and N$_2$ in poly([VBIM][SCN]) (a) CO$_2$-poly[VBIM]$^{30+}$ (b) CO$_2$-[SCN]$^-$ (c) N$_2$-poly[VBIM]$^{30+}$ (d) N$_2$-[SCN]$^-$.
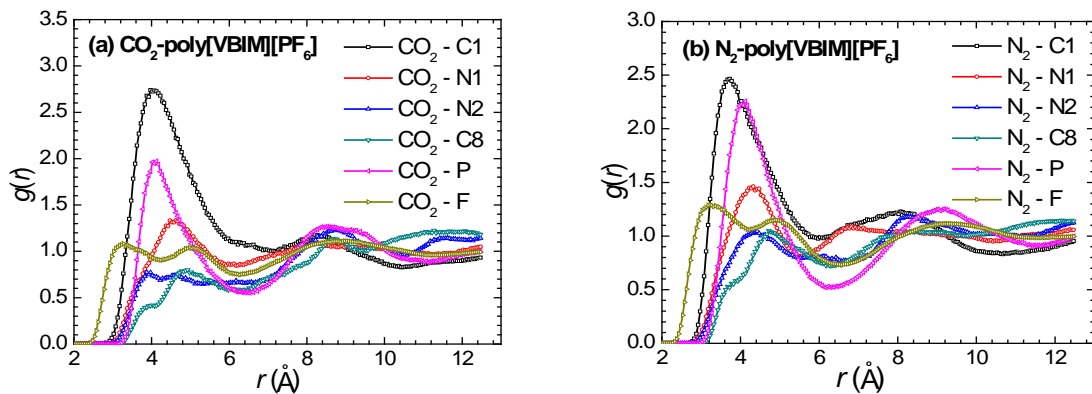
Figure 7.13 Radial distribution functions of CO$_2$ and N$_2$ in poly([VBIM][PF$_6$]) (a) CO$_2$-poly[VBIM][PF$_6$] (b) N$_2$-poly[VBIM][PF$_6$].
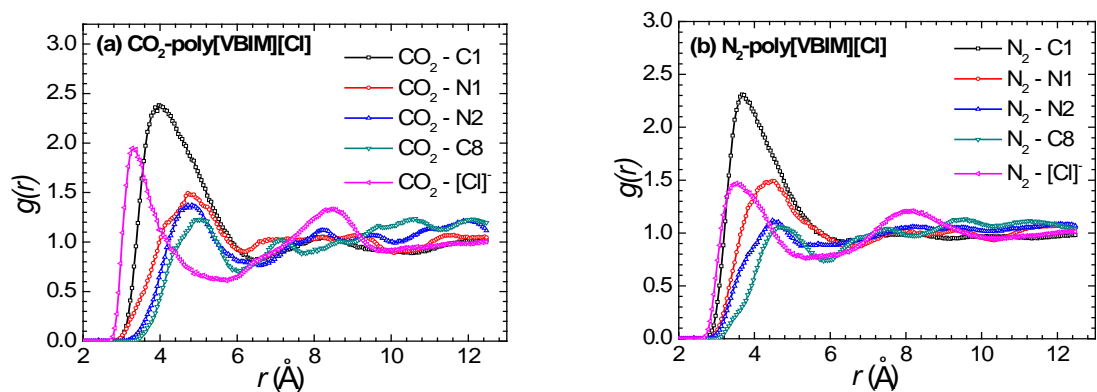
Figure 7.14 Radial distribution functions of CO$_2$ and N$_2$ in poly([VBIM][Cl]) (a) CO$_2$-poly[VBIM][Cl] (b) N$_2$-poly[VBIM][Cl].

Figures **7.12-7.14** illustrate the $g(r)$ of CO$_2$ and N$_2$ in poly([VBIM][SCN]), poly([VBIM][PF$_6$]) and poly([VBIM][Cl]). Similar trend is observed that the $g(r)$ peaks of both CO$_2$ and N$_2$ around the C1 atom of poly[VBIM]$^{30+}$ are substantially higher. This further confirms that gas has a substantially strong interaction with the end group of side chain in polycation. Consequently, anions in the four PILs under study do not play a dominant role in gas solubility. Such a phenomenon differs remarkably from monomeric ILs, in which anions have a significant effect [289].

7.3.6 Sorption, Diffusion and Permeation

Table 7.10 lists the solubility coefficients of CO$_2$ and N$_2$ in [BMIM][TF$_2$N], [BMIM][SCN], poly([VBIM][TF$_2$N]), poly([VBIM][SCN]), poly([VBIM][PF$_6$]) and poly([VBIM][Cl]) at 308 K. Experimentally measured data are available in poly([VBIM][TF$_2$N]) and [BMIM][TF$_2$N]. In general, the simulated results agree fairly well with measured data. The deviations might be attributed to the fact the solubility in simulation was considered at infinite dilution, not identical to experimental condition. It is noteworthy that large deviations are usually seen in the literature between experimental and simulation solubility data, e.g., 1–2 fold for N$_2$ and O$_2$ in polystyrenes [254], 1–5 fold for CO$_2$ and N$_2$ in PTMSP [255], 4–17 fold for CO$_2$ and N$_2$ in PEEK [256], and 1–55 fold for CO$_2$ and N$_2$ in polyimides [96]. In the two ILs, the predicted solubility decreases substantially from [BMIM][TF$_2$N] to [BMIM][SCN], consistent with experimental trend [290]. This indicates anion is crucial to gas solubility in ILs as experimentally revealed [290]. Recently, Babarao et al. suggested that cation-anion interaction of ILs dictates CO$_2$ solubility and a weaker cation-anion interaction would lead to a higher CO$_2$ solubility [291]. From **Figures 7.2a** and **7.3a**, it can been found that $g(r)$ of [BMIM][TF$_2$N] is lower than

[BMIM][SCN], thus the solubility in [BMIM][TF$_2$N] is higher. The solubility coefficients in the four PILs are close with a variation much smaller than in ILs. This is consistent with the discussion in **Figures 7.11-7.14** that polycation instead of anion plays a significant role in gas-membrane interaction. In other words, gas solubility is largely independent of the type of anion, which was indeed observed by experiment [196]. Nevertheless, the solubility coefficients in the four PILs increase, despite small magnitude, following the order of poly([VBIM][SCN]) < poly([VBIM][PF$_6$]) < poly([VBIM][TF$_2$N]) < poly([VBIM][Cl]). This is because solubility is affected by several factors. For instance, a large FFV usually leads to a higher solubility since more space is available for sorption.

Table 7.10 Solubility coefficients [cm^3 (STP) cm^{-3} (membrane) bar^{-1}], diffusivities [10^{-8} cm^2 s^{-1}] and permeabilities [barrer] of CO_2 and N_2 in [BMIM][TF$_2$N], [BMIM][SCN], poly([VBIM][TF$_2$N]), poly([VBIM][SCN]), poly([VBIM][PF$_6$]) and poly([VBIM][Cl]) at 308 K. The experimental measurements were at 308.15 K and 10 atm in ref. 190.

Membrane	Gas	S_{sim}	S_{exp}	$D_{sim}*10^2$	$D_{exp}*10^2$	P_{sim}	P_{exp}
[BMIM][TF$_2$N]	CO_2	1.4 ± 1.6	2.01	1.38 ± 0.46	5.02	257	1344.3
	N_2	0.14 ± 0.16	0.09	1.39 ± 0.20	5.89	26	68.3
[BMIM][SCN]	CO_2	0.61 ± 1.43	–	0.80 ± 0.35	–	65	–
	N_2	0.04 ± 0.06	–	0.96 ± 0.47	–	5	–
poly([VBIM][TF$_2$N])	CO_2	1.1 ± 1.2	1.13	0.49 ± 0.27	0.67	72	101.4
	N_2	0.1 ± 0.05	0.05	0.52 ± 0.36	0.75	7	4.55
poly([VBIM][SCN])	CO_2	0.78 ± 0.97	–	0.44 ± 0.24	–	46	–
	N_2	0.05 ± 0.06	–	0.47 ± 0.32	–	3	–
poly([VBIM][PF$_6$])	CO_2	0.94 ± 1.10	–	0.39 ± 0.33	–	49	–
	N_2	0.09 ± 0.08	–	0.37 ± 0.16	–	4.4	–
poly([VBIM][Cl])	CO_2	1.4 ± 1.6	–	0.24 ± 0.07	–	45	–
	N_2	0.18 ± 0.17	–	0.25 ± 0.11	–	6	–

Table 7.10 also lists the diffusivities of CO$_2$ and N$_2$ in the six membranes. While simulation agrees fairly well with experiment in poly([VBIM][TF$_2$N]), the simulated values in [BMIM][TF$_2$N] are approximately 4-fold lower than experimental data. It is recognized that gas diffusion in a membrane is affected by many factors and a 5-fold difference between prediction and experiment is usually acceptable [287]. Indeed, large deviations are commonly observed between experimental and simulation diffusion data, e.g., 1−67 fold for CO$_2$ and N$_2$ in PEEK [256], up to 100 fold for N$_2$ and CO$_2$ in polyimides [96], and 8 fold for N$_2$ in PVC [136]. The diffusivities in the four PILs increase following poly([VBIM][Cl]) < poly([VBIM][PF$_6$]) < poly([VBIM][SCN]) < poly([VBIM][TF$_2$N]). This is consistent with the increasing percentage of large voids (> 3 Å) shown in **Figure 7.8**. As discussed before, only large voids contribute to the diffusion of CO$_2$ and N$_2$. Comparing ILs and PILs, we see that gas diffusion in PILs is slower than in ILs. This is because the diffusion pathway in PILs is largely blocked. In addition, monomeric ions move much faster than polyions, thus facilitate gas diffusion in ILs.

The permeabilities of CO$_2$ and N$_2$ were calculated from $P = D \cdot S$. As presented in **Table 7.10**, the simulated P in [BMIM][TF$_2$N] are lower than experimental data because the simulated D are 4-fold lower. However, the simulated P in poly([VBIM][TF$_2$N]) agree fairly well with experimental results. In the four PILs, poly([VBIM][TF$_2$N]) exhibits the highest permeability, while other three PILs have similar permeability.

To quantify the separation factor of CO$_2$/N$_2$, **Table 7.11** lists the sorption, diffusion and permeation selectivities in the six membranes. The diffusion selectivity is nearly one in all the six membranes, thus the solution and permeation selectivities are approximately equal. This indicates the selectivity of CO$_2$/N$_2$ in the PILs and ILs

is sorption driven. In the PILs, polycation plays a major role in sorption rather than anion; therefore, CO$_2$/N$_2$ separation in the PILs is primarily governed by the polycation. Furthermore, the simulated diffusion selectivities in [BMIN][TF$_2$N] and poly([VBIM][TF$_2$N]) match well with experimental values. However, the simulated sorption and permeation selectivities are approximately half of experimental values. This is due to the deviations in the simulated and experimental solubilities as shown in **Table 7.10**. Based on simulation, poly([VBIM][SCN]) shows the highest permeation selectivity, which is twice of that in poly([VBIM][Cl]). As pointed out above, the reason is poly([VBIM][SCN]) has the highest sorption selectivity.

Table 7.11 Sorption, diffusion and permeation selectivities of CO$_2$/N$_2$ in [BMIM][TF$_2$N], [BMIM][SCN], poly([VBIM][TF$_2$N]), poly([VBIM][SCN]), poly([VBIM][PF$_6$]) and poly([VBIM][Cl]) at 308 K. The experimental data are from ref. 190.

Membrane	S_{CO_2}/S_{N_2}		D_{CO_2}/D_{N_2}		P_{CO_2}/P_{N_2}	
	Sim.	Exp.	Sim.	Exp.	Sim.	Exp.
[BMIM][TF$_2$N]	10.0	22.3	0.99	0.85	9.9	19.7
[BMIM][SCN]	15.3	–	0.83	–	12.7	–
poly([VBIM][TF$_2$N])	11.0	24.7	0.94	0.91	10.3	22.3
poly([VBIM][SCN])	15.6	–	0.94	–	14.7	–
poly([VBIM][PF$_6$])	10.4	–	1.05	–	10.9	–
poly([VBIM][Cl])	7.8	–	0.96	–	7.5	–

7.4 Conclusions

In this Chapter, CO$_2$/N$_2$ separation in four PILs including poly([VBIM][TF$_2$N]), poly([VBIM][SCN]), poly([VBIM][PF$_6$]) and poly([VBIM][Cl]) has been investigated. For comparison, two ILs [BMIM][TF$_2$N] and [BMIM][SCN] are also considered. To validate the model membranes, the densities of PILs and ILs are

predicted and found to match well with available experiment data. Due to polymerization, PILs are more densely packed and thus possess higher density compared to ILs. The predicted solubility parameters and vaporization enthalpies for ILs are in experimentally measured range. The anions of PILs interact more strongly with the backbone of polycation (poly[VBIM]$^{30+}$). The end group of side chain has the highest mobility, which creates a large free volume. As attributed to the blockage of chain connectivity, the mobility and fractional free volume of PILs are smaller compared to ILs. The void size in the four PILs is less than 6 Å. [TF$_2$N]$^-$-based IL and PIL possess a greater percentage of large voids (> 3 Å).

CO$_2$ and N$_2$ exhibit different interactions with the two [BMIM]$^+$-based ILs. In [BMIM][TF$_2$N], gas has a similar interaction with [BMIM]$^+$ and [TF$_2$N]$^-$. In [BMIM][Tf$_2$N], however, gas interacts with [BMIM]$^+$ more strongly than with [SCN]$^-$. Therefore, gas solubility in ILs is significantly affected by anion; [BMIM][TF$_2$N] has a higher solubility than [BMIM][SCN]. In the PILs, a large free volume is created around the end group of poly[VBIM]$^{30+}$. Thu gas has a substantially strong interaction with polycation rather than anion. Consequently, gas solubilities are close in the four PILs with a common polycation. Furthermore, the simulated solubilities are in good accordance with available experimental data. Consistent with the increasing percentage of large voids, diffusivities in the four PILs increase as poly([VBIM][Cl]) < poly([VBIM][PF$_6$]) < poly([VBIM][SCN]) < poly([VBIM][TF$_2$N]). For CO$_2$/N$_2$ separation, diffusion selectivities are approximately equal to one indicating the separation is driven by sorption. Among the four PILs, poly([VBIM][SCN]) exhibits the highest permeation selectivity.

In general, the simulated properties agree fairly well with available experimental data, whereas a certain degree of deviations exist as attributed to a few factors. Firstly,

the simulation condition is at infinite dilution, different from experimental condition. Secondly, cross-linkers were used experimentally to fabricate PIL membranes for improving mechanical properties. For simplification, however, cross-linkers are not included in the simulation. Thirdly, the force field used was not specifically developed for the ILs and PILs, thus may not be optimal. Nevertheless, this simulation study for the first time provides microscopic insights into the structural and dynamic properties of polycation and anion, as well as the behavior of gas molecules in PILs. Particularly, it is revealed why the polycation (poly[VBIM]$^{30+}$) plays a predominant role in gas-membrane interaction, sorption and separation. The molecular insights are valuable to assist in the development of new PILs for high-performance CO$_2$ capture. A wide variety of ions can be used to synthesize PILs, the bottom-up guidance is indispensable to screen and design promising candidates.

CHAPTER 8 CONCLUSIONS AND FUTURE WORK

8.1 Conclusions

In this thesis, two newly synthesized polymer membranes (PIMs and PILs) have been investigated by molecular simulation. The main contents include four parts. In the first part, two PIMs are examined for their performance in gas permeation and separation. The second and third parts are focused on the effects of functional groups and residual solvents on membrane structure and gas permeation, respectively. In the last part, simulation is conducted on the permeation and separation of CO_2 and N_2 in PILs towards CO_2 capture. The major conclusions are summarized below.

8.1.1 PIMs

PIM-1 and PIM-7 can be described by the polymer-consistent force field (PCFF) and the predicted densities match well with experimental data. The PIMs have larger fractional free volumes (47.7% in PIM-1 and 46.6% in PIM-7) than other glassy polymers such as PIs. Interconnected voids with a diameter up to 9 Å exist in the membranes. PIM-1 has a slightly lower density and a larger FFV than PIM-7 because of the presence of cyano groups.

The calculated solubilities of H_2, O_2, CH_4 and CO_2 agree well with measured results, decreasing in the order of $CO_2 > CH_4 > O_2 > H_2$. Due to the microporous structure and polar sites, the solubilities in PIM-1 and PIM-7 are substantially larger than those in other polymers. Good correlations exist between solubilities and the critical temperatures of gases. H_2 exhibits frequent jumping because of its small diameter, O_2 and CO_2 are trapped in a void for a while and then jump. With a relatively larger molecule, CH_4 is predominantly trapped. The diffusion coefficients increase in the order of $CH_4 < CO_2 < O_2 < H_2$, and are correlated well with the

effective diameters of gases. The calculated sorption, diffusion and permeation selectivities of CO_2/H_2, CO_2/O_2 and CO_2/CH_4 agree well with experimental data. Moreover, the permeation selectivity is dominated by the sorption selectivity.

8.1.2 Functionalized PIMs

Gas separation is examined in PIM-1 membranes with different functional groups (carboxyl, trifluoromethyl and phenylsulfone). A robust procedure is proposed to effectively equilibrate model membranes and the densities predicted match perfectly with experimental data. By adding functional groups, membrane density increases, while fractional free volume decreases. The percentage of small voids (0 – 3 Å) decreases in the order of CX-PIM > TFMPS-PIM > PIM-1. The calculated and experimental wide-angle X-ray diffraction patterns are in good accordance, and the predicted d-spacing distances agree well with experimental results.

The binding energies of CO_2 with cyano, trifluoromethyl, phenylfulfone and carboxyl groups are -8.96, -5.88, -12.52, -13.29 kJ/mol, respectively. The solubility and diffusion coefficients of CO_2 and N_2 agree well with experimental results, especially the solubility coefficients. Particularly, the diffusion coefficients increase in the order of CX-PIM < TFMPS-PIM < PIM-1. Due to the similar molecule size of CO_2 and N_2, the diffusion selectivity is almost a constant and independent on functional groups. However, the sorption selectivity largely increases upon adding functional groups, especially carboxyl group. The permeability selectivity follows the same order as the sorption selectivity PIM-1 < TFMPS-PIM < CX-PIM. The study reveals that CO_2/N_2 separation in functional PIMs is dominated by sorption selectivity.

8.1.3 Effects of Residual Solvents

The effects of residual solvents (CH_3OH, $CHCl_3$ and H_2O) on PIM-1 membrane structure and permeation properties are investigated. The membrane density and

fractional free volume are not significantly affected by solvent, in contrast to void size distribution. The percentage of large voids (> 6 Å) decreases in the order of PIM-1/CH$_3$OH > PIM-1/CHCl$_3$ > PIM-1/H$_2$O, consistent with PALS measurements. The lack of large voids in PIM-1/H$_2$O membranes is attributed to the formation of H$_2$O clusters. Between residual solvents and PIM-1, the interaction energies increase as H$_2$O < CH$_3$OH < CHCl$_3$, following the order of hydrophobicity. A good correlation exists between the interaction energies and critical volumes of solvents. The polar cyano and dioxane groups interact more preferentially with hydrophilic CH$_3$OH and H$_2$O, whereas less polar carbon atoms favor the interaction with hydrophobic CHCl$_3$. Among the three solvents, CHCl$_3$ shows the slowest mobility, while H$_2$O exhibits the highest. The mobility of PIM-1 chains increases in the presence of solvents.

H$_2$ solubility and diffusion coefficients from simulation and experiment are in good agreement. The solubility decreases in the order of PIM-1/CH$_3$OH > PIM-1/CHCl$_3$ > PIM-1/H$_2$O. Compared to dry PIM-1 membrane, the solubility in wet PIM-1 drops as also observed experimentally. The diffusion in PIM-1/H$_2$O is largely slowed down due to the occupation of large voids by H$_2$O clusters.

8.1.4 Polymeric ILs

For the first time, gas permeation/separation in PIL membranes are studied by simulation. For comparison, two ILs are also considered. The calculated properties including densities, solubility parameters and vaporization enthalpies are consistent with experimental results. This suggests the molecular models and PCFF are suitable for PILs and ILs. The fractional free volumes in [BMIM][TF$_2$N], [BMIM][SCN], poly([VBIM][TF$_2$N]), poly([VBIM][SCN]), poly([VBIM][PF$_6$]) and poly([VBIM][Cl]) are 36.2%, 37.8%, 33.0%, 34.9%, 31.9% and 34.0%, respectively.

The largest void has a size of 6 Å, and $[TF_2N]^-$-based ILs and PILs possess a greater percentage of large voids (> 3 Å).

CO_2 and N_2 interact preferentially with the end group of polycation, which plays a dominant role in gas-membrane interaction. As a consequence, gas solubility is largely independent of the type of anion. The simulated solubilities are in good agreement with available experimental data. Following the increasing percentage of large voids, gas diffusivities increase in the order of poly([VBIM][Cl]) < poly([VBIM][PF$_6$]) < poly([VBIM][SCN]) < poly([VBIM][TF$_2$N]). The permeation selectivity of CO_2/N_2 is determined by sorption selectivity because diffusion selectivity approaches unity. Among the four PILs, poly([VBIM][SCN]) exhibits the highest sorption and permeation selectivity.

8.2 Future work

Molecular simulation has been successfully applied in this thesis to investigate gas permeation and separation in polymer membranes. Microscopic insights are provided between chemical structures and membrane properties, the effects of functional groups and residual solvents. To facilitate the design of new polymer membranes for high-performance gas separation, several challenging and practically important topics are recommended for future simulation endeavor.

1. In remarkable contrast to crystalline materials such as zeolites and metal-organic frameworks, polymer membranes are amorphous without well-defined structures. A model for polymer membrane should be sufficiently equilibrated prior to evaluating gas permeation and separation. The performance of a model membrane could be affected by equilibration procedure; however, there is no specific and unique guidance

for equilibration. It is crucial to use or develop a reliable and efficient equilibrium method.

2. Diffusion in non-porous polymer membranes is activated jumping process from one void to another due to the relaxation of polymer chains. In glassy membranes, polymer chains are rather rigid with small mobility; thus gas diffusion hardly occurs in a short time scale. Toward this end, extremely long simulation is usually needed to reach normal diffusion behavior. One way to overcome this is to apply transition-state theory and the other is to use coarse-grained model for polymer chains.

3. More realistic models should be developed to mimic polymer membranes. For instance, cross-linkers are used in experiment to fabricate PILs for stronger mechanical strength. For simplification, however, cross-linkers are not incorporation into our model membranes for PILs. Consequently, the membrane properties and performance would be inevitably affected. Ideally, future simulation studies should take this factor into account.

4. A practical gas separation involves gas mixtures. Currently, most experimental and simulation studies for gas permeation and separation in polymer membranes are focused on pure gases. However, the separation of gas mixtures cannot be simply extrapolated from pure gases because mixing effect could be significant. Therefore, it is important to examine gas mixtures for better evaluating polymer membranes in practical conditions.

BIBLIOGRAPHY

[1] J. K. Mitchell, *J. Membr. Sci.*, **1830**, 100, 11.

[2] T. Graham, *J. Chem. Soc.*, **1864**, 17, 334.

[3] T. Graham, *J. Chem. Soc.*, **1866**, 20, 235.

[4] S. von Wroblewski, *Ann. der Phys.*, **1879**, 8, 29.

[5] H. Strathmann, *AIChE J.*, **2001**, 47, 1077.

[6] L. M. Robeson, *J. Membr. Sci.*, **1991**, 62, 165.

[7] L. M. Robeson, *J. Membr. Sci.*, **2008**, 320, 390.

[8] S. A. Stern, Y. Mi, H. Yamamoto, and A. K. St. Clair, *J. Polym. Sci. B*, **1989**, 27, 1887.

[9] S. L. Liu, R. Wang, T. S. Chung, M. L. Chng, Y. Liu, and R. H. Vora, *J. Membr. Sci.*, **2002**, 202, 165.

[10] K. Tanaka, H. Kita, M. Okano, and K. I. Okamoto, *Polymer*, **1992**, 33, 585.

[11] M. Yoshino, K. Ito, H. Kita, and K.-I. Okamoto, *J. Polym. Sci. Part B: Polym. Phys.*, **2000**, 38, 1707.

[12] C. E. Powell and G. G. Qiao, *J. Membr. Sci.*, **2006**, 279, 1.

[13] E. M. Maya, D. M. Muñoz, J. G. de la Campa, J. de Abajo, and Á. E. Lozano, *Desalination*, **2006**, 199, 188.

[14] J. Grobelny, D. M. Rice, F. E. Karasz, and W. J. MacKnight, *Polym. Commun. Guildford*, **1990**, 31, 86.

[15] G. C. Kapantaidakis, S. P. Kaldis, X. S. Dabou, and G. P. Sakellaropoulos, *J. Membr. Sci.*, **1996**, 110, 239.

[16] E. K. Chatzidaki, E. P. Favvas, S. K. Papageorgiou, N. K. Kanellopoulos, and N. V. Theophilou, *Eur. Polym. J.*, **2007**, 43, 5010.

[17] S. S. Hosseini, M. M. Teoh, and T. S. Chung, *Polymer*, **2008**, 49, 1594.

[18] A. Bos, I. Pünt, H. Strathmann, and M. Wessling, *AIChE J.*, **2001**, 47, 1088.

[19] E. V. Perez, K. J. Balkus Jr, J. P. Ferraris, and I. H. Musselman, *J. Membr. Sci.*, **2009**, 328, 165.

[20] J. Ahn, W. J. Chung, I. Pinnau, and M. D. Guiver, *J. Membr. Sci.*, **2008**, 314, 123.

[21] S. Kim, L. Chen, J. K. Johnson, and E. Marand, *J. Membr. Sci.*, **2007**, 294, 147.

[22] S. Husain and W. J. Koros, *J. Membr. Sci.*, **2007**, 288, 195.

[23] T. S. Chung, L. Y. Jiang, Y. Li, and S. Kulprathipanja, *Prog. Polym. Sci. (Oxford)*, **2007**, 32, 483.

[24] T. W. Pechar, S. Kim, B. Vaughan, E. Marand, M. Tsapatsis, H. K. Jeong, and C. J. Cornelius, *J. Membr. Sci.*, **2006**, 277, 195.

[25] S. Kim, T. W. Pechar, and E. Marand, *Desalination*, **2006**, 192, 330.

[26] C. M. Zimmerman, A. Singh, and W. J. Koros, *J. Membr. Sci.*, **1997**, 137, 145.

[27] H. Kita, T. Inada, K. Tanaka, and K.-I. Okamoto, *J. Membr. Sci.*, **1994**, 87, 139.

[28] T.-S. Chung, J. Ren, R. Wang, D. Li, Y. Liu, K. P. Pramoda, C. Cao, and W. W. Loh, *J. Membr. Sci.*, **2003**, 214, 57.

[29] A. Bos, I. G. M. Pünt, M. Wessling, and H. Strathmann, *Sep. Purif. Technol.*, **1998**, 14, 27.

[30] Y. Xiao, T.-S. Chung, H. M. Guan, and M. D. Guiver, *J. Membr. Sci.*, **2007**, 302, 254.

[31] Y. Liu, M. L. Chng, T.-S. Chung, and R. Wang, *J. Membr. Sci.*, **2003**, 214, 83.

[32] G.-S. Liou, J.-S. B. Wang, S.-T. Tseng, and R. C.-C. Tsiang, *J. Polym. Sci., Part A: Polym. Chem.*, **1999**, 37, 1673.

[33] M. D. Guiver, G. P. Robertson, Y. Dai, F. Bilodeau, Y. S. Kang, K. J. Lee, J. Y. Jho, and J. Won, *J. Polym. Sci., Part A: Polym. Chem.*, **2002**, 40, 4193.

[34] A. P. Kharitonov, Y. L. Moskvin, D. A. Syrtsova, V. M. Starov, and V. V. Teplyakov, *J. Appl. Polym. Sci*, **2004**, 92, 6.

[35] C. Fuhrman, M. Nutt, K. Vichtovonga, and M. R. Coleman, *J. Appl. Polym. Sci*, **2004**, 91, 1174.

[36] H. Kawakami, M. Mikawa, and S. Nagaoka, *J. Membr. Sci.*, **1996**, 118, 223.

[37] F. Zhou and W. J. Koros, *Polymer*, **2006**, 47, 280.

[38] X. Qiao, T.-S. Chung, and K. P. Pramoda, *J. Membr. Sci.*, **2005**, 264, 176.

[39] S. A. Stern, *J. Membr. Sci.*, **1994**, 94, 1.

[40] R. W. Spillman and M. B. Sherwin, *Chem. Tech.*, **1990**, 20, 378.

[41] R. I. Berry, *Chem. Eng. (New York)*, **1981**, 88.

[42] M. M. Qiu, S. T. Hwang, and Y. K. Kao, *Ind. Eng. Chem. Res.*, **1989**, 28, 1670.

[43] R. W. Spillman, *Chem. Eng. Prog.*, **1989**, 85, 41.

[44] S. Loeb and S. Sourirajan, in Sea Water Demineralization by Means of an Osmotic Membrane, 1963.

[45] R. W. Baker, *Ind. Eng. Chem. Res.*, **2002**, 41, 1393.

[46] D. R. Paul, *J. Polym. Sci.: Polym. Phys. Ed.*, **1974**, 12, 1221.

[47] S. Rosenbaum and O. Cotton, *J. Polym. Sci. A*, **1969**, 7, 101.

[48] X. Hong, Y. C. Jean, H. Yang, S. S. Jordan, and W. J. Koros, *Macromolecules*, **1996**, 29, 7859.

[49] V. P. Shantarovich, I. B. Kevdina, Y. P. Yampolskii, and A. Y. Alentiev, *Macromolecules*, **2000**, 33, 7453.

[50] B. S. Ghanem, K. J. Msayib, N. B. McKeown, K. D. M. Harris, Z. Pan, P. M. Budd, A. Butler, J. Selbie, D. Book, and A. Walton, *Chem. Commun.*, **2007**, 67.

[51] T. Emmler, K. Heinrich, D. Fritsch, P. M. Budd, N. Chaukura, D. Ehlers, K. Rätzke, and F. Faupel, *Macromolecules*, **2010**, 43, 6075.

[52] N. Du, G. P. Robertson, J. Song, I. Pinnau, S. Thomas, and M. D. Guiver, *Macromolecules*, **2008**, 41, 9656.

[53] M. L. Williams, R. F. Landel, and J. D. Ferry, *J. Am. Chem. Soc.*, **1955**, 77, 3701.

[54] A. Bondi, *J. Phys. Chem.*, **1964**, 68, 441.

[55] R. Voorintholt, M. T. Kosters, G. Vegter, G. Vriend, and W. G. J. Hol, *J. Mol. Graph.*, **1989**, 7, 243.

[56] X.-Y. Wang, A. J. Hill, B. D. Freeman, and I. C. Sanchez, *J. Membr. Sci.*, **2008**, 314, 15.

[57] A. Singh, B. D. Freeman, and I. Pinnau, *J. Polym. Sci. B*, **1998**, 36, 289.

[58] D. J. Cox, *Arch. Biochem. Biophys.*, **1971**, 142, 514.

[59] S. W. Fox, R. McCauley, D. Joseph, C. R. Windsor, and S. Yuyama, *Life Sci. Space Res.*, **1966**, 4, 111.

[60] D. I. C. Kells and J. E. Guillet, *J Polym Sci Part A-2 Polym Phys*, **1969**, 7, 1895.

[61] J. Mazur, *J. Chem. Phys.*, **1963**, 38, 193.

[62] R. L. McCullough and P. H. Lindenmeyer, *Summer Comput. Simul. Conf.*, **1972**, 1, 347.

[63] H. Takeuchi and K. Okazaki, *J. Chem. Phys.*, **1990**, 92, 5643.

[64] K. Choi and W. H. Jo, *Macromolecules*, **1995**, 28, 8598.

[65] H. Liu, X. Ding, J. Yi, L. Zhang, and S. Wu, *Fro. Chem. Eng. Ch.*, **2010**, 4, 257.

[66] S. Pricl and M. Fermeglia, *Chem. Eng. Commun.*, **2003**, 190, 1267.

[67] P. V. K. Pant and R. H. Boyd, *Macromolecules*, **1993**, 26, 679.

[68] R. H. Gee and R. H. Boyd, *Polymer*, **1995**, 36, 1435.

[69] N. F. A. Van Der Vegt, *Macromolecules*, **2000**, 33, 3153.

[70] F. Mozaffari, H. Eslami, and J. Moghadasi, *Polymer*, **2010**, 51, 300.

[71] J. Han and R. H. Boyd, *Polymer*, **1996**, 37, 1797.

[72] F. Müller-Plathe, *J. Chem. Phys.*, **1992**, 96, 3200.

[73] J. H. D. Boshoff, R. F. Lobo, and N. J. Wagner, *Macromolecules*, **2001**, 34, 6107.

[74] N. F. A. van der Vegt, *J. Membr. Sci.*, **2002**, 205, 125.

[75] P. Memari, V. Lachet, and B. Rousseau, *Polymer*, **2010**, 51, 4978.

[76] F. Faure, B. Rousseau, V. Lachet, and P. Ungerer, *Fluid Phase Equilib.*, **2007**, 261, 168.

[77] P. Memari, V. Lachet, M.-H. Klopffer, B. Flaconnèche, and B. Rousseau, *J. Membr. Sci.*, **2012**, 390–391, 194.

[78] L. Sanguigno, F. Cosentino, D. Larobina, and G. Mensitieri, *Soft Mater.*, **2011**, 9, 169.

[79] H. Eslami and F. Müller-Plathe, *Macromolecules*, **2007**, 40, 6413.

[80] S. G. Charati and S. A. Stern, *Macromolecules*, **1998**, 31, 5529.

[81] L. R. Segooa, P. E. Ngoepe, and G. Goldbeck-Wood, *Radiat. Eff. Defects Solids*, **2001**, 156, 341.

[82] R. M. Sok, H. J. C. Berendsen, and W. F. Van Gunsteren, *J. Chem. Phys.*, **1992**, 96, 4699.

[83] Y. Tamai, H. Tanaka, and K. Nakanishi, *Macromolecules*, **1994**, 27, 4498.

[84] Y. Tamai, H. Tanaka, and K. Nakanishi, *Macromolecules*, **1995**, 28, 2544.

[85] Y. Tamai, H. Tanaka, and K. Nakanishi, *Fluid Phase Equilib.*, **1995**, 104, 363.

[86] J. S. Yang, K. Choi, and W. H. Jo, *Macromol. Theor. Simulat.*, **2000**, 9, 287.

[87] J. R. Fried and D. K. Goyal, *J. Polym. Sci.B*, **1998**, 36, 519.

[88] T. Zheng and J. R. Fried, *Sep. Purif. Technol.*, **2001**, 36, 959.

[89] D. Hofmann, L. Fritz, J. Ulbrich, and D. Paul, *Polymer*, **1997**, 38, 6145.

[90] D. Hofmann, M. Heuchel, Y. Yampolskii, V. Khotimskii, and V. Shantarovich, *Macromolecules*, **2002**, 35, 2129.

[91] X.-Y. Wang, R. D. Raharjo, H. J. Lee, Y. Lu, B. D. Freeman, and I. C. Sanchez, *J. Phys. Chem. B*, **2006**, 110, 12666.

[92] E. Smit, M. H. V. Mulder, C. A. Smolders, H. Karrenbeld, J. Van Eerden, and D. Feil, *J. Membr. Sci.*, **1992**, 73, 247.

[93] A. A. Gusev and U. W. Suter, *J. Chem. Phys.*, **1993**, 99, 2228.

[94] A. A. Gusev, S. Arizzi, U. W. Suter, and D. J. Moll, *J. Chem. Phys.*, **1993**, 99, 2221.

[95] A. A. Gusev and U. W. Suter, *Phys. Rev. A*, **1991**, 43, 6488.

[96] M. Heuchel, D. Hofmann, and P. Pullumbi, *Macromolecules*, **2004**, 37, 201.

[97] R. Zhang and W. L. Mattice, *J. Membr. Sci.*, **1995**, 108, 15.

[98] A. Shimazu, T. Miyazaki, and K. Ikeda, *J. Membr. Sci.*, **2000**, 166, 113.

[99] D. Hofman, J. Ulbrich, D. Fritsch, and D. Paul, *Polymer*, **1996**, 37, 4773.

[100] L. Zhang, Y. Xiao, T.-S. Chung, and J. Jiang, *Polymer*, **2010**, 51, 4439.

[101] S. Pandiyan, D. Brown, S. Neyertz, and N. F. A. van der Vegt, *Macromolecules*, **2010**, 43, 2605.

[102] S. Neyertz, *Macromol. Theor. Simul.*, **2007**, 16, 513.

[103] I. A. Ronova, E. M. Rozhkov, A. Y. Alentiev, and Y. P. Yampolskii, *Macromol. Theor. Simulat.*, **2003**, 12, 425.

[104] K. S. Chang, C. C. Hsiung, C. C. Lin, and K. L. Tung, *J. Phys. Chem. B*, **2009**, 113, 10159.

[105] K. S. Chang, C. C. Tung, K. S. Wang, and K. L. Tung, *J. Phys. Chem. B*, **2009**, 113, 9821.

[106] S. Pandiyan, D. Brown, N. F. A. van der Vegt, and S. Neyertz, *J. Polym. Sci. Part B: Polym. Phys.*, **2009**, 47, 1166.

[107] H. Savoji, D. Rana, T. Matsuura, M. Soltanieh, and S. Tabe, *J. Appl. Polym. Sci*, **2012**, 124, 2287.

[108] M. Rahbari-Sisakht, A. F. Ismail, and T. Matsuura, *Sep. Purif. Technol.*, **2012**, 88, 99.

[109] S. Modarresi, M. Soltanieh, S. A. Mousavi, and I. Shabani, *J. Appl. Polym. Sci*, **2012**, 124, E199.

[110] C. Casado-Coterillo, J. Soto, T. M. Jimaré, S. Valencia, A. Corma, C. Téllez, and J. Coronas, *Chem. Eng. Sci.*, **2012**, 73, 116.

[111] K. Ghosal, R. T. Chern, B. D. Freeman, W. H. Daly, and I. I. Negulescu, *Macromolecules*, **1996**, 29, 4360.

[112] C. L. Aitken, W. J. Koros, and D. R. Paul, *Macromolecules*, **1992**, 25, 3651.

[113] I. Pinnau and W. J. Koros, *J. Appl. Polym. Sci.*, **1991**, 43, 1491.

[114] S. Niemelä, J. Leppänen, and F. Sundholm, *Polymer*, **1996**, 37, 4155.

[115] O. Hölck, M. Heuchel, M. Böhning, and D. Hofmann, *J. Polym. Sci., Part B: Polym. Phys.*, **2008**, 46, 59.

[116] O. Hölck, M. R. Siegert, M. Heuchel, and M. Böhning, *Macromolecules*, **2006**, 39, 9590.

[117] X.-Y. Wang, P. J. in 't Veld, Y. Lu, B. D. Freeman, and I. C. Sanchez, *Polymer*, **2005**, 46, 9155.

[118] A. A. Gusev, U. W. Suter, and D. J. Moll, *Macromolecules*, **1995**, 28, 2582.

[119] F. T. Gentile, S. Arizzi, U. W. Suter, and P. J. Ludovice, *Ind. Eng. Chem. Res.*, **1995**, 34, 4193.

[120] S. Arizzi, P. H. Mott, and U. W. Suter, *J. Polym. Sci., Part B: Polym. Phys.*, **1992**, 30, 415.

[121] M. López-González, E. Saiz, J. Guzmán, and E. Riande, *J. Chem. Phys.*, **2001**, 115, 6728.

[122] J.-H. Zhou, R.-X. Zhu, J.-M. Zhou, and M.-B. Chen, *Polymer*, **2006**, 47, 5206.

[123] Q. Yang and L. E. Achenie, *J. Phys. Chem. C*, **2012**, 116, 7409.

[124] B. Hanson, V. Pryamitsyn, and V. Ganesan, *J. Phys. Chem. B*, **2011**, 116, 95.

[125] P. S. Rallabandi and D. M. Ford, *J. Membr. Sci.*, **2000**, 171, 239.

[126] D. Pavel and R. Shanks, *Polymer*, **2003**, 44, 6713.

[127] R. Shanks and D. Pavel, *Mol. Simul.*, **2002**, 28, 939.

[128] E. Tocci, A. Gugliuzza, L. De Lorenzo, M. Macchione, G. De Luca, and E. Drioli, *J. Membr. Sci.*, **2008**, 323, 316.

[129] D. Pavel and R. Shanks, *Polymer*, **2005**, 46, 6135.

[130] K.-L. Tung, K.-T. Lu, R.-C. Ruaan, and J.-Y. Lai, *Desalination*, **2006**, 192, 391.

[131] M. Macchione, J. C. Jansen, G. De Luca, E. Tocci, M. Longeri, and E. Drioli, *Polymer*, **2007**, 48, 2619.

[132] S. Y. Lim, T. T. Tsotsis, and M. Sahimi, *J. Chem. Phys.*, **2003**, 119, 496.

[133] E. Tocci, E. Bellacchio, N. Russo, and E. Drioli, *J. Membr. Sci.*, **2002**, 206, 389.

[134] E. Tocci, D. Hofmann, D. Paul, N. Russo, and E. Drioli, *Polymer*, **2001**, 42, 521.

[135] C. García, P. Tiemblo, A. E. Lozano, J. de Abajo, and J. G. de la Campa, *J. Membr. Sci.*, **2002**, 205, 73.

[136] P. Tiemblo, E. Saiz, J. Guzmán, and E. Riande, *Macromolecules*, **2002**, 35, 4167.

[137] J. Sacristan and C. Mijangos, *Macromolecules*, **2010**, 43, 7357.

[138] J. R. Fried and P. Ren, *Comput. Theor. Polym. Sci.*, **2000**, 10, 447.

[139] J. R. Fried and N. Hu, *Polymer*, **2003**, 44, 4363.

[140] N. Hu and J. R. Fried, *Polymer*, **2005**, 46, 4330.

[141] J. Fried, *J. Inorg. Organomet. Polym. Mater.*, **2006**, 16, 407.

[142] N. C. Karayiannis, V. G. Mavrantzas, and D. N. Theodorou, *Macromolecules*, **2004**, 37, 2978.

[143] K.-L. Tung and K.-T. Lu, *J. Membr. Sci.*, **2006**, 272, 37.

[144] I. Cozmuta, M. Blanco, and W. A. Goddard Iii, *J. Phys. Chem. B*, **2007**, 111, 3151.

[145] F. Pan, J. Ma, L. Cui, and Z. Jiang, *Chem. Eng. Sci.*, **2009**, 64, 5192.

[146] Y. Tamai and H. Tanaka, *Fluid Phase Equilib.*, **1998**, 144, 441.

[147] P. M. Budd, B. Ghanem, K. Msayib, N. B. McKeown, and C. Tattershall, *J. Mater. Chem.*, **2003**, 13, 2721.

[148] N. B. McKeown, P. M. Budd, K. J. Msayib, B. S. Ghanem, H. J. Kingston, C. E. Tattershall, S. Makhseed, K. J. Reynolds, and D. Fritsch, *Chem. Eur. J.*, **2005**, 11, 2610.

[149] N. B. McKeown and P. M. Budd, *Chem. Sco. Rev.*, **2006**, 35, 675.

[150] N. B. McKeown and P. M. Budd, *Macromolecules*, **2010**, 43, 5163.

[151] P. M. Budd and N. B. McKeown, *Polym. Chem.*, **2010**, 1, 63.

[152] N. B. McKeown, P. M. Budd, K. J. Msayib, B. S. Ghanem, H. J. Kingston, C. E. Tattershall, S. Makhseed, K. J. Reynolds, and D. Fritsch, *Chem. Eur. J*, **2005**, 11, 2610.

[153] S. Thomas, I. Pinnau, N. Du, and M. D. Guiver, *J. Membr. Sci.*, **2009**, 333, 125.

[154] C. R. Mason, L. Maynard-Atem, N. M. Al-Harbi, P. M. Budd, P. Bernardo, F. Bazzarelli, G. Clarizia, and J. C. Jansen, *Macromolecules*, **2011**, 44, 6471.

[155] C. L. Staiger, S. J. Pas, A. J. Hill, and C. J. Cornelius, *Chem. Mater.*, **2008**, 20, 2606.

[156] P. M. Budd, A. Butler, J. Selbie, K. Mahmood, N. B. McKeown, B. Ghanem, K. Msayib, D. Book, and A. Walton, *Phys. Chem. Chem. Phys.*, **2007**, 9, 1802.

[157] S. Makhseed, J. Samuel, A. Bumajdad, and M. Hassan, *J. Appl. Polym. Sci*, **2008**, 109, 2591.

[158] J. Germain, J. M. J. Fréchet, and F. Svec, *Small*, **2009**, 5, 1098.

[159] H. J. MacKintosh, P. M. Budd, and N. B. McKeown, *J. Mater. Chem.*, **2008**, 18, 573.

[160] N. B. McKeown, S. Hanif, K. Msayib, C. E. Tattershall, and P. M. Budd, *Chem. Commun.*, **2002**, 2782.

[161] P. M. Budd, B. S. Ghanem, S. Makhseed, N. B. McKeown, K. J. Msayib, and C. E. Tattershall, *Chem. Commun.*, **2004**, 230.

[162] P. M. Budd, K. J. Msayib, C. E. Tattershall, B. S. Ghanem, K. J. Reynolds, N. B. McKeown, and D. Fritsch, *J. Membr. Sci.*, **2005**, 251, 263.

[163] R. L. de Miranda, J. Kruse, K. Rätzke, F. Faupel, D. Fritsch, V. Abetz, P. M. Budd, J. D. Selbie, N. B. McKeown, and B. S. Ghanem, *Phys. Status Solidi - Rapid Res. Lete.*, **2007**, 1, 190.

[164] B. S. Ghanem, N. B. McKeown, P. M. Budd, and D. Fritsch, *Macromolecules*, **2008**, 41, 1640.

[165] P. M. Budd, N. B. McKeown, B. S. Ghanem, K. J. Msayib, D. Fritsch, L. Starannikova, N. Belov, O. Sanfirova, Y. Yampolskii, and V. Shantarovich, *J. Membr. Sci.*, **2008**, 325, 851.

[166] N. Du, G. P. Robertson, I. Pinnau, and M. D. Guiver, *Macromolecules*, **2009**, 42, 6023.

[167] N. Du, G. P. Robertson, I. Pinnau, and M. D. Guiver, *Macromolecules*, **2010**, 43, 8580.

[168] N. Du, G. P. Robertson, I. Pinnau, S. Thomas, and M. D. Guiver, *Macromol. Rapid Commun.*, **2009**, 30, 584.

[169] N. Du, G. P. Robertson, J. Song, I. Pinnau, and M. D. Guiver, *Macromolecules*, **2009**, 42, 6038.

[170] N. Du, M. M. D. Cin, I. Pinnau, A. Nicalek, G. P. Robertson, and M. D. Guiver, *Macromol. Rapid Commun.*, **2011**, 32, 631.

[171] N. Du, H. B. Park, G. P. Robertson, M. M. Dal-Cin, T. Visser, L. Scoles, and M. D. Guiver, *Nat. Mater.*, **2011**, 10, 372.

[172] F. Y. Li, Y. Xiao, T.-S. Chung, and S. Kawi, *Macromolecules*, **2012**, 45, 1427.

[173] M. Heuchel, D. Fritsch, P. M. Budd, N. B. McKeown, and D. Hofmann, *J. Membr. Sci.*, **2008**, 318, 84.

[174] G. S. Larsen, P. Lin, F. R. Siperstein, and C. M. Colina, *Adsorption*, **2010**, 17, 21.

[175] G. S. Larsen, P. Lin, K. E. Hart, and C. M. Colina, *Macromolecules*, **2011**, 44, 6944.

[176] L. Zhao, D. Zhai, B. Liu, Z. Liu, C. Xu, W. Wei, Y. Chen, and J. Gao, *Chem. Eng. Sci.*, **2012**, 68, 101.

[177] J. E. Bara, D. E. Camper, D. L. Gin, and R. D. Noble, *Acc. Chem. Res*, **2010**, 43, 152.

[178] J. Tang, H. Tang, W. Sun, H. Plancher, M. Radosz, and Y. Shen, *Chem. Commun.*, **2005**, 3325.

[179] J. Tang, H. Tang, W. Sun, M. Radosz, and Y. Shen, *J. Polym. Sci. A*, **2005**, 43, 5477.

[180] J. Tang, H. Tang, W. Sun, M. Radosz, and Y. Shen, *Polymer*, **2005**, 46, 12460.

[181] J. Zhu, J. Zhou, H. Zhang, and R. Chu, *J. Polym. Res.*, **2011**, 18, 2011.

[182] Y. B. Xiong, H. Wang, Y. J. Wang, and R. M. Wang, *Polym. Adv. Technol.*, DOI: 10. 1002/pat.1973.

[183] S. Supasitmongkol and P. Styring, *Energy & Environ. Sci.*, **2010**, 3, 1961.

[184] A. Blasig, J. Tang, X. Hu, S. P. Tan, Y. Shen, and M. Radosz, *Ind. Eng. Chem. Res.*, **2007**, 46, 5542.

[185] J. Tang, W. Sun, H. Tang, M. Radosz, and Y. Shen, *Macromolecules*, **2005**, 38, 2037.

[186] H. Tang, J. Tang, S. Ding, M. Radosz, and Y. Shen, *J. Polym. Sci., Part A: Polym. Chem.*, **2005**, 43, 1432.

[187] J. E. Bara, S. Lessmann, C. J. Gabriel, E. S. Hatakeyama, R. D. Noble, and D. L. Gin, *Ind. Eng. Chem. Res.*, **2007**, 46, 5397.

[188] J. E. Bara, C. J. Gabriel, E. S. Hatakeyama, T. K. Carlisle, S. Lessmann, R. D. Noble, and D. L. Gin, *J. Membr. Sci.*, **2008**, 321, 3.

[189] X. Hu, J. Tang, A. Blasig, Y. Shen, and M. Radosz, *J. Membr. Sci.*, **2006**, 281, 130.

[190] P. Li, K. P. Pramoda, and T. S. Chung, *Ind. Eng. Chem. Res.*, **2011**, 50, 9344.

[191] J. E. Bara, E. S. Hatakeyama, D. L. Gin, and R. D. Noble, *Polym. Adv. Technol.*, **2008**, 19, 1415.

[192] T. K. Carlisle, E. F. Wiesenauer, G. D. Nicodemus, D. L. Gin, and R. D. Noble, *Ind. Eng. Chem. Res.*, **2012**, DOI: 10.1021/ie202305m.

[193] P. Li, D. R. Paul, and T. S. Chung, *Green Chem.*, **2012**, 14, 1052.

[194] Y. C. Hudiono, T. K. Carlisle, A. L. LaFrate, D. L. Gin, and R. D. Noble, *J. Membr. Sci.*, **2011**, 370, 141.

[195] C. Cadena, J. L. Anthony, J. K. Shah, T. I. Morrow, J. F. Brennecke, and E. J. Maginn, *J. Am. Chem. Soc.*, **2004**, 126, 5300.

[196] A. Samadi, R. K. Kemmerlin, and S. M. Husson, *Energy Fuels*, **2010**, 24, 5797.

[197] J. E. Bara, D. L. Gin, and R. D. Noble, *Ind. Eng. Chem. Res.*, **2008**, 47, 9919.

[198] R. S. Bhavsar, S. C. Kumbharkar, and U. K. Kharul, *J. Membr. Sci.*, **2011**, 389, 305.

[199] A. Warshel and S. Lifson, *J. Chem. Phys.*, **1970**, 53, 582.

[200] N. L. Allinger, Y. H. Yuh, and J. H. Lii, *J. Am. Chem. Soc.*, **1989**, 111, 8551.

[201] W. D. Cornell, P. Cieplak, C. I. Bayly, I. R. Gould, K. M. Merz, D. M. Ferguson, D. C. Spellmeyer, T. Fox, J. W. Caldwell, and P. A. Kollman, *J. Am. Chem. Soc.*, **1995**, 117, 5179.

[202] B. R. Brooks, R. E. Bruccoleri, B. D. Olafson, D. J. States, S. Swaminathan, and M. Karplus, *J. Comput. Chem.*, **1983**, 4, 187.

[203] P. Dauber-Osguthorpe, V. A. Roberts, D. J. Osguthorpe, J. Wolff, M. Genest, and A. T. Hagler, *Proteins: Struct., Funct., Bioinf.*, **1988**, 4, 31.

[204] H. Sun, S. J. Mumby, J. R. Maple, and A. T. Hagler, *J. Am. Chem. Soc.*, **1994**, 116, 2978.

[205] H. Sun, *J. Phys. Chem. B*, **1998**, 102, 7338.

[206] N. Metropolis, A. W. Rosenbluth, M. N. Rosenbluth, A. H. Teller, and E. Teller, *J. Chem. Phys.*, **1953**, 21, 1087.

[207] S. Ban and T. J. H. Vlugt, *Mol. Simul.*, **2008**, 35, 1105.

[208] S. Bhattacharya and K. E. Gubbins, *Langmuir*, **2006**, 22, 7726.

[209] J. Ahn, W.-J. Chung, I. Pinnau, J. Song, N. Du, G. P. Robertson, and M. D. Guiver, *J. Membr. Sci.*, **2010**, 346, 280.

[210] B. S. Ghanem, N. B. McKeown, P. M. Budd, J. D. Selbie, and D. Fritsch, *Adv. Mater. (Weinheim, Ger.)*, **2008**, 20, 2766.

[211] D. N. Theodorou and U. W. Suter, *Macromolecules*, **1985**, 18, 1467.

[212] W. Smith and T. R. Forester, *J. Mol. Graphics*, **1996**, 14, 136.

[213] W. Smith, C. W. Yong, and P. M. Rodger, *Mol. Simul.*, **2002**, 28, 385.

[214] H. Sun, *Macromolecules*, **1995**, 28, 701.

[215] H. Sun, S. J. Mumby, J. R. Maple, and A. T. Hagler, *J. Am. Chem. Soc.*, **1994**, 116, 2978.

[216] H. Sun, S. J. Mumby, J. R. Maple, and A. T. Hagler, *J. Phys. Chem.*, **1995**, 99, 5873.

[217] H. Sun and D. Rigby, *Spectrochim. Acta A*, **1997**, 53, 1301.

[218] H. J. C. Berendsen, J. P. M. Postma, W. F. Vangunsteren, A. Dinola, and J. R. Haak, *J. Chem. Phys.*, **1984**, 81, 3684.

[219] B. Nagasaka, T. Eguchi, H. Nakayama, N. Nakamura, and Y. Ito, *Radiat. Phys. Chem.*, **2000**, 58, 581.

[220] B. Widom, *J. Chem. Phys.*, **1963**, 39, 2808.

[221] P. M. Budd, *personal communication.*, **2009**.

[222] R. Babarao and J. W. Jiang, *Langmuir*, **2008**, 24, 6270.

[223] R. Babarao and J. W. Jiang, *Energy Environ. Sci.*, **2008**, 1, 139.

[224] O. M. Yaghi, M. O'Keeffe, N. W. Ockwig, H. K. Chae, M. Eddaoudi, and J. Kim, *Nature (London)*, **2003**, 423, 705.

[225] H. M. El-Kaderi, J. R. Hunt, J. L. Mendoza-Cortes, A. P. Cote, R. E. Taylor, M. O'Keeffe, and O. M. Yaghi, *Science*, **2007**, 316, 268.

[226] J. J. Shieh and T. S. Chung, *J. Polym. Sci., Part B: Polym. Phys.*, **1999**, 37, 2851.

[227] D. W. Breck, Zeolite Molecular Sieves: Structure, Chemistry and Use, John Wiley & Sons, Inc. New York, USA, 1974.

[228] B. E. Poling, J. M. Prausnitz, and J. P. O'Connell, The Properties of Gases and Liquids, McGraw-Hill, 2000.

[229] M. Meunier, *J. Chem. Phys.*, **2005**, 123, 13496.

[230] P. Gestoso and M. Meunier, *Mol. Simul.*, **2008**, 34, 1135.

[231] L. Sarkisov, T. Duren, and R. Snurr, *Mol. Phys.*, **2004**, 102, 211.

[232] A. I. Skoulidas and D. Sholl, *J. Phys. Chem. B*, **2005**, 109, 15760.

[233] R. Babarao and J. W. Jiang, *Langmuir*, **2008**, 24, 5474.

[234] H. Lin and B. D. Freeman, *J. Membr. Sci.*, **2004**, 239, 105.

[235] T. C. Merkel, V. I. Bondar, K. Nagai, B. D. Freeman, and I. Pinnau, *J. Polym. Sci., Part B: Polym. Phys.*, **2000**, 38, 415.

[236] V. Teplyakov and P. Meares, *Gas Sep. Purif.*, **1990**, 4, 66.

[237] C. Staudt-Bickel and W. J. Koros, *J. Membr. Sci.*, **1999**, 155, 145.

[238] Y. Xiao, B. T. Low, S. S. Hosseini, T. S. Chung, and D. R. Paul, *Prog. Polym. Sci. (Oxford)*, **2009**, 34, 561.

[239] D. T. Clausi and W. J. Koros, *J. Membr. Sci.*, **2000**, 167, 79.

[240] Y. Liu, R. Wang, and T. S. Chung, *J. Membr. Sci.*, **2001**, 189, 231.

[241] I. D. Sharpe, A. F. Ismail, and S. J. Shilton, *Sep. Purif. Technol.*, **1999**, 17, 101.

[242] L. M. Costello and W. J. Koros, *J. Polym. Sci., Part B: Polym. Phys.*, **1994**, 32, 701.

[243] P. Hacarlioglu, L. Toppare, and L. Yilmaz, *J. Membr. Sci.*, **2003**, 225, 51.

[244] M. Iqbal, Z. Man, H. Mukhtar, and B. K. Dutta, *J. Membr. Sci.*, **2008**, 318, 167.

[245] T. H. Kim, W. J. Koros, G. R. Husk, and K. C. O'Brien, *J. Membr. Sci.*, **1988**, 37, 45.

[246] S. A. Stern, Y. Mi, H. Yamamoto, and A. K. S. Clair, *J. Polym. Sci. B*, **1989**, 27, 1887.

[247] M. Calle, A. E. Lozano, J. de Abajo, J. G. de la Campa, and C. Álvarez, *J. Membr. Sci.*, **2010**, 365, 145.

[248] S. Sridhar, B. Smitha, M. Ramakrishna, and T. M. Aminabhavi, *J. Membr. Sci.*, **2006**, 280, 202.

[249] S. K. Sen and S. Banerjee, *J. Membr. Sci.*, **2010**, 350, 53.

[250] D. N. Theodorou and U. W. Suter, *Macromolecules*, **1986**, 19, 139.

[251] M. J. Frisch, G. W. Trucks, H. B. Schlegel, G. E. Scuseria, M. A. Robb, J. R. Cheeseman, V. G. Zakrzewski, J. A. Montgomery, R. E. Stratmann, J. C. Burant, S. Dapprich, J. M. Millam, A. D. Daniels, K. N. Kudin, M. C. Strain, O. Farkas, J. Tomasi, V. Barone, M. Cossi, R. Cammi, B. Mennucci, C. Pomelli, C. Adamo, S. Clifford, J. Ochterski, G. A. Petersson, P. Y. Ayala, Q. Cui, K. Morokuma, D. K. Malick, A. D. Rabuck, K. Raghavachari, J. B. Foresman, J. Cioslowski, J. V. Ortiz, B. B. Stefanov, G. Liu, A. Liashenko, P. Piskorz, I. Komaromi, R. Gomperts, R. L. Martin, D. J. Fox, T. Keith, M. A. Al-Laham, C. Y. Peng, A. Nanayakkara, C. Gonzalez, M. Challacombe, P. M. W. Gill, B. G. Johnson, W. Chen, M. W. Wong, J. L. Andres, M. Head-Gordon, E. S. Replogle, and J. A. Pople, Gaussian 09, Gaussian, Inc., 2009.

[252] W. M. Lee, *Polym. Eng. Sci.*, **1980**, 20, 65.

[253] J. Weber, Q. Su, M. Antonietti, and A. Thomas, *Macromol. Rapid Commun.*, **2007**, 28, 1871.

[254] Q. L. Liu and Y. Huang, *J. Phys. Chem. B*, **2006**, 110, 17375.

[255] X.-Y. Wang, F. T. Willmore, R. D. Raharjo, X. Wang, B. D. Freeman, A. J. Hill, and I. C. Sanchez, *J. Phys. Chem. B*, **2006**, 110, 16685.

[256] E. Tocci and P. Pullumbi, *Mol. Simul.*, **2006**, 32, 145.

[257] M. Meunier, *J. Chem. Phys.*, **2005**, 123, 134906.

[258] P. M. Budd, N. B. McKeown, B. S. Ghanem, K. J. Msayib, D. Fritsch, L. Starannikova, N. Belov, O. Sanfirova, Y. Yampolskii, and V. Shantarovich, *J. Membr. Sci.*, **2008**, 325, 851.

[259] A. Bondi, Physical Properties of Molecular Crystals, Liquids and Gases, John Wiley & Sons, Inc., 1968.

[260] M. Kotelyanskii and D. N. Theodorou, in 'Simulation Methods for Polymers', New York, 2004.

[261] C. Joly, D. Le Cerf, C. Chappey, D. Langevin, and G. Muller, *Sep. Purif. Tech.*, **1999**, 16, 47.

[262] Y. Kostina, G. Bondarenko, A. Alentiev, and Y. Yampolskii, *Vysokomol. Soed.*, **2006**, 48, 41.

[263] P. J. Linstrom and W. G. Mallard, in 'NIST Chemistry WebBook', Gaithersburg, Maryland, 2011.

[264] W. J. Fang, L. L. Zhang, and J. W. Jiang, *Mol. Simul.*, **2010**, 36, 992.

[265] Y. Yampolskii, A. Alentiev, G. Bondarenko, Y. Kostina, and M. Heuchel, *Ind. Eng. Chem. Res.*, **2010**, 49, 12031.

[266] K. A. Dill and S. Bromberg, Molecular Driving Forces Garland Science, 2010.

[267] L. L. Zhang, Y. C. Xiao, T. S. Chung, and J. W. Jiang, *Polymer*, **2010**, 51, 4439.

[268] S. Bachu, *Energy Convers. Manage.*, **2000**, 41, 953.

[269] R. E. Baltus, B. H. Culbertson, S. Dai, H. Luo, and D. W. DePaoli, *J. Phys. Chem. B*, **2004**, 108, 721.

[270] J. E. Bara, T. K. Carlisle, C. J. Gabriel, D. Camper, A. Finotello, D. L. Gin, and R. D. Noble, *Ind. Eng. Chem. Res.*, **2009**, 48, 2739.

[271] R. A. Gaussian 09, Frisch, M. J.; Trucks, G. W.; Schlegel, H. B.; Scuseria, G. E.; Robb, M. A.; Cheeseman, J. R.; Scalmani, G.; Barone, V.; Mennucci, B.; Petersson, G. A.; Nakatsuji, H.; Caricato, M.; Li, X.; Hratchian, H. P.; Izmaylov, A. F.; Bloino, J.; Zheng, G.; Sonnenberg, J. L.; Hada, M.; Ehara, M.; Toyota, K.; Fukuda, R.; Hasegawa, J.; Ishida, M.; Nakajima, T.; Honda, Y.; Kitao, O.; Nakai, H.; Vreven, T.; Montgomery, Jr., J. A.; Peralta, J. E.; Ogliaro, F.; Bearpark, M.; Heyd, J. J.; Brothers, E.; Kudin, K. N.; Staroverov, V. N.; Kobayashi, R.; Normand, J.; Raghavachari, K.; Rendell, A.; Burant, J. C.; Iyengar, S. S.; Tomasi, J.; Cossi, M.; Rega, N.; Millam, N. J.; Klene, M.; Knox, J. E.; Cross, J. B.; Bakken, V.; Adamo, C.; Jaramillo, J.; Gomperts, R.; Stratmann, R. E.; Yazyev, O.; Austin, A. J.; Cammi, R.; Pomelli, C.; Ochterski, J. W.; Martin, R. L.; Morokuma, K.; Zakrzewski, V. G.; Voth, G. A.; Salvador, P.; Dannenberg, J. J.; Dapprich, S.; Daniels, A. D.; Farkas, Ö.;

Foresman, J. B.; Ortiz, J. V.; Cioslowski, J.; Fox, D. J. Gaussian, Inc., Wallingford CT, 2009.

[272] U. C. Singh and P. A. Kollman, *J. Comput. Chem.*, **1984**, 5, 129.

[273] W. Smith, C. W. Yong, and P. M. Rodger, *Mol. Simul.*, **2002**, 28, 385.

[274] H. Sun, *J. Phys. Chem. B*, **1998**, 102, 7338.

[275] J. Troncoso, C. A. Cerdeiriña, Y. A. Sanmamed, L. Romaní, and L. P. N. Rebelo, *J. Chem. Eng. Data*, **2006**, 51, 1856.

[276] U. Domańska and M. Królikowska, *J. Chem. Eng. Data*, **2010**, 55, 2994.

[277] H. Luo, G. A. Baker, and S. Dai, *J. Phys. Chem. B*, **2008**, 112, 10077.

[278] S. S. Moganty and R. E. Baltus, *Ind. Eng. Chem. Res.*, **2010**, 49, 5846.

[279] J. P. Armstrong, C. Hurst, R. G. Jones, P. Licence, K. R. J. Lovelock, C. J. Satterley, and I. J. Villar-Garcia, *Phys. Chem. Chem. Phys.*, **2007**, 9, 982.

[280] K. Swiderski, A. McLean, C. M. Gordon, and D. H. Vaughan, *Chem. Commun.*, **2004**, 2178.

[281] S. H. Lee and S. B. Lee, *Chem. Commun.*, **2005**, 3469.

[282] A. Marciniak, *Int. J. Mol. Sci.*, **2010**, 11, 1973.

[283] T. Morrow and E. Maginn, *J. Phys. Chem. B*, **2002**, 106, 12807.

[284] S. U. Lee, J. Jung, and Y. K. Han, *Chem. Phys. Lett.*, **2005**, 406, 332.

[285] T. Umecky, M. Kanakubo, and Y. Ikushima, *Fluid Phase Equilib.*, **2005**, 228, 329.

[286] M. Kanakubo, s. K. R. Harri, N. Tsuchihashi, K. Ibuki, and M. Ueno, *J. Phys. Chem. B*, **2007**, 111, 2062.

[287] W. Fang, L. Zhang, and J. Jiang, *J. Phys. Chem. C*, **2011**, 115, 14123.

[288] D. Q. Vu, W. J. Koros, and S. J. Miller, *J. Membr. Sci.*, **2003**, 211, 311.

[289] S. N. V. K. Aki, B. R. Mellein, E. M. Saurer, and J. F. Brennecke, *J. Phys. Chem. B*, **2004**, 108, 20355.

[290] A.-L. Revelli, F. Mutelet, and J.-N. l. Jaubert, *J. Phys. Chem. B*, **2010**, 114, 12908.

[291] R. Babarao, S. Dai, and D. E. Jiang, *J. Phys. Chem. B*, **2011**, 115, 9789.

PUBLICATIONS

1. <u>Fang W. J.</u>, Luo Z. L., Jiang, J. W. "CO_2 capture in poly(ionic liquid) membranes: atomistic insight into the role of anions", *Physical Chemistry Chemical Physics*, 2013, 15, 651-658.

2. <u>Fang W. J.</u>, Zhang L. L., Jiang, J. W. "Gas permeation and separation in functionalized polymers of intrinsic microporosity: A combination of molecular simulations and ab initio calculations", *Journal of Physical Chemistry C*, 2011, 115, 14123-14130.

3. <u>Fang W. J.</u>, Zhang L. L., Jiang, J. W. "Polymers of intrinsic microporosity for gas permeation: A molecular simulation study", *Molecular Simulation*, 2010, 36, 992-1003.

4. Zhang L. L., <u>Fang W. J.</u>, Jiang J. W. "Effects of residual solvent on membrane structure and gas permeation in a polymer of intrinsic microporosity: Insight from atomistic simulation", *Journal of Physical Chemistry C*, 2011, 115, 11233-11239.

PRESENTATIONS

1. <u>Fang W. J.</u>, Luo Z. L., Jiang J. W. "Poly(ionic liquid) membranes for CO_2/N_2 separation: Insight from atomistic simulation", *AIChE Annual Meeting*, Pittsburgh, USA (Oct. 2012).

2. <u>Fang W. J.</u>, Jiang J. W. "Gas Permeation and Separation in Polymeric Ionic Liquids: Insights from Atomistic Simulation", 7th Conference of Aseanian Membrane Society, Busan, South Korea (Jul. 2012).

3. <u>Fang W. J.</u>, Zhang L. L., Jiang J. W. "Effects of functional group and residual solvent on membrane structure and gas permeation in a polymer of intrinsic microporosity: Insights from atomistic simulations", *14th Asia Pacific Confederation of Chemical Engineering Congress,* Suntec, Singapore, (Feb. 2012).

4. <u>Fang W. J.</u>, Zhang L. L., Jiang J. W. "Gas permeation and separation in functionalized polymers of intrinsic microposority: A combination of molecular simulations and ab initio calculations", *AIChE Annual Meeting*, Minneapolis, USA (Oct. 2011).

5. Zhang L. L., <u>Fang W. J.</u>, Jiang J. W. "Effects of residual solvent on membrane structure and gas permeation in a polymer of intrinsic microposority: Insight from atomistic simulation", *AIChE Annual Meeting*, Minneapolis, USA (Oct. 2011).

6. <u>Fang W. J.</u>, Jiang J. W. "Polymers of intrinsic microporosity for gas permeation: A molecular simulation study", *International Conference on Materials for Advanced Technologies 2011*, Suntec, Singapore, (Jun. 2011).

APPENDICES

Supplier	Elsevier Limited The Boulevard,Langford Lane Kidlington,Oxford,OX5 1GB,UK
Registered Company Number	1982084
Customer name	WEIJIE FANG
Customer address	09-00, STARPOINT 319, PASIR PANJANG ROAD
	SINGAPORE, SINGAPORE 118653
License number	3046310880034
License date	Dec 12, 2012
Licensed content publisher	Elsevier
Licensed content publication	Journal of Membrane Science
Licensed content title	The upper bound revisited
Licensed content author	Lloyd M. Robeson
Licensed content date	15 July 2008
Licensed content volume number	320
Licensed content issue number	1–2
Number of pages	11
Start Page	390
End Page	400
Type of Use	reuse in a thesis/dissertation
Portion	figures/tables/illustrations
Number of figures/tables/illustrations	2
Format	both print and electronic
Are you the author of this Elsevier article?	No
Will you be translating?	No
Order reference number	
Title of your thesis/dissertation	MOLECULAR SIMULATION OF GAS PERMEATION AND SEPARATION IN POLYMER MEMBRANES

Expected completion date	Dec 2012
Estimated size (number of pages)	130
Elsevier VAT number	GB 494 6272 12
Permissions price	0.00 USD
VAT/Local Sales Tax	0.0 USD / 0.0 GBP
Total	0.00 USD

Terms and Conditions

INTRODUCTION

1. The publisher for this copyrighted material is Elsevier. By clicking "accept" in connection with completing this licensing transaction, you agree that the following terms and conditions apply to this transaction (along with the Billing and Payment terms and conditions established by Copyright Clearance Center, Inc. ("CCC"), at the time that you opened your Rightslink account and that are available at any time at http://myaccount.copyright.com).

GENERAL TERMS

2. Elsevier hereby grants you permission to reproduce the aforementioned material subject to the terms and conditions indicated.

3. Acknowledgement: If any part of the material to be used (for example, figures) has appeared in our publication with credit or acknowledgement to another source, permission must also be sought from that source. If such permission is not obtained then that material may not be included in your publication/copies. Suitable acknowledgement to the source must be made, either as a footnote or in a reference list at the end of your publication, as follows:

"Reprinted from Publication title, Vol /edition number, Author(s), Title of article / title of chapter, Pages No., Copyright (Year), with permission from Elsevier [OR APPLICABLE SOCIETY COPYRIGHT OWNER]." Also Lancet special credit - "Reprinted from The Lancet, Vol. number, Author(s), Title of article, Pages No., Copyright (Year), with permission from Elsevier."

4. Reproduction of this material is confined to the purpose and/or media for which permission is hereby given.

5. Altering/Modifying Material: Not Permitted. However figures and illustrations may be altered/adapted minimally to serve your work. Any other abbreviations, additions, deletions and/or any other alterations shall be made only with prior written authorization of Elsevier Ltd. (Please contact Elsevier at permissions@elsevier.com)

6. If the permission fee for the requested use of our material is waived in this instance, please be advised that your future requests for Elsevier materials may attract a fee.

7. Reservation of Rights: Publisher reserves all rights not specifically granted in the combination of (i) the license details provided by you and accepted in the course of this licensing transaction, (ii) these terms and conditions and (iii) CCC's Billing and Payment

terms and conditions.

8. License Contingent Upon Payment: While you may exercise the rights licensed immediately upon issuance of the license at the end of the licensing process for the transaction, provided that you have disclosed complete and accurate details of your proposed use, no license is finally effective unless and until full payment is received from you (either by publisher or by CCC) as provided in CCC's Billing and Payment terms and conditions. If full payment is not received on a timely basis, then any license preliminarily granted shall be deemed automatically revoked and shall be void as if never granted. Further, in the event that you breach any of these terms and conditions or any of CCC's Billing and Payment terms and conditions, the license is automatically revoked and shall be void as if never granted. Use of materials as described in a revoked license, as well as any use of the materials beyond the scope of an unrevoked license, may constitute copyright infringement and publisher reserves the right to take any and all action to protect its copyright in the materials.

9. Warranties: Publisher makes no representations or warranties with respect to the licensed material.

10. Indemnity: You hereby indemnify and agree to hold harmless publisher and CCC, and their respective officers, directors, employees and agents, from and against any and all claims arising out of your use of the licensed material other than as specifically authorized pursuant to this license.

11. No Transfer of License: This license is personal to you and may not be sublicensed, assigned, or transferred by you to any other person without publisher's written permission.

12. No Amendment Except in Writing: This license may not be amended except in a writing signed by both parties (or, in the case of publisher, by CCC on publisher's behalf).

13. Objection to Contrary Terms: Publisher hereby objects to any terms contained in any purchase order, acknowledgment, check endorsement or other writing prepared by you, which terms are inconsistent with these terms and conditions or CCC's Billing and Payment terms and conditions. These terms and conditions, together with CCC's Billing and Payment terms and conditions (which are incorporated herein), comprise the entire agreement between you and publisher (and CCC) concerning this licensing transaction. In the event of any conflict between your obligations established by these terms and conditions and those established by CCC's Billing and Payment terms and conditions, these terms and conditions shall control.

14. Revocation: Elsevier or Copyright Clearance Center may deny the permissions described in this License at their sole discretion, for any reason or no reason, with a full refund payable to you. Notice of such denial will be made using the contact information provided by you. Failure to receive such notice will not alter or invalidate the denial. In no event will Elsevier or Copyright Clearance Center be responsible or liable for any costs, expenses or damage incurred by you as a result of a denial of your permission request, other than a refund of the amount(s) paid by you to Elsevier and/or Copyright Clearance Center for denied permissions.

LIMITED LICENSE

The following terms and conditions apply only to specific license types:

15. **Translation**: This permission is granted for non-exclusive world **English** rights only unless your license was granted for translation rights. If you licensed translation rights you may only translate this content into the languages you requested. A professional translator must perform all translations and reproduce the content word for word preserving the integrity of the article. If this license is to re-use 1 or 2 figures then permission is granted for non-exclusive world rights in all languages.

16. **Website**: The following terms and conditions apply to electronic reserve and author websites:
Electronic reserve: If licensed material is to be posted to website, the web site is to be password-protected and made available only to bona fide students registered on a relevant course if:
This license was made in connection with a course,
This permission is granted for 1 year only. You may obtain a license for future website posting,
All content posted to the web site must maintain the copyright information line on the bottom of each image,
A hyper-text must be included to the Homepage of the journal from which you are licensing at http://www.sciencedirect.com/science/journal/xxxxx or the Elsevier homepage for books at http://www.elsevier.com , and
Central Storage: This license does not include permission for a scanned version of the material to be stored in a central repository such as that provided by Heron/XanEdu.

17. **Author website** for journals with the following additional clauses:

All content posted to the web site must maintain the copyright information line on the bottom of each image, and the permission granted is limited to the personal version of your paper. You are not allowed to download and post the published electronic version of your article (whether PDF or HTML, proof or final version), nor may you scan the printed edition to create an electronic version. A hyper-text must be included to the Homepage of the journal from which you are licensing
at http://www.sciencedirect.com/science/journal/xxxxx . As part of our normal production process, you will receive an e-mail notice when your article appears on Elsevier's online service ScienceDirect (www.sciencedirect.com). That e-mail will include the article's Digital Object Identifier (DOI). This number provides the electronic link to the published article and should be included in the posting of your personal version. We ask that you wait until you receive this e-mail and have the DOI to do any posting.

Central Storage: This license does not include permission for a scanned version of the material to be stored in a central repository such as that provided by Heron/XanEdu.

18. **Author website** for books with the following additional clauses:
Authors are permitted to place a brief summary of their work online only.
A hyper-text must be included to the Elsevier homepage at http://www.elsevier.com . All content posted to the web site must maintain the copyright information line on the bottom of each image. You are not allowed to download and post the published electronic version

of your chapter, nor may you scan the printed edition to create an electronic version.

Central Storage: This license does not include permission for a scanned version of the material to be stored in a central repository such as that provided by Heron/XanEdu.

19. **Website** (regular and for author): A hyper-text must be included to the Homepage of the journal from which you are licensing at http://www.sciencedirect.com/science/journal/xxxxx. or for books to the Elsevier homepage at http://www.elsevier.com

20. **Thesis/Dissertation**: If your license is for use in a thesis/dissertation your thesis may be submitted to your institution in either print or electronic form. Should your thesis be published commercially, please reapply for permission. These requirements include permission for the Library and Archives of Canada to supply single copies, on demand, of the complete thesis and include permission for UMI to supply single copies, on demand, of the complete thesis. Should your thesis be published commercially, please reapply for permission.

21. **Other Conditions**: